

The Pennsylvania State University
The Graduate School
Department of Energy and Mineral Engineering

**ANALYSIS OF SPONTANEOUS IMBIBITION IN FRACTURED,
HETEROGENEOUS SANDSTONE**

A Dissertation in
Petroleum and Natural Gas Engineering

by
Basar Basbug

© 2009 Basar Basbug

Submitted in Partial Fulfillment
of the Requirements
for the Degree of

Doctor of Philosophy

May 2009

The dissertation of Basar Basbug was reviewed and approved* by the following:

Zuleima T. Karpyn
Assistant Professor of Petroleum and Natural Gas Engineering
Dissertation Advisor
Chair of Committee

Turgay Ertekin
Professor of Petroleum and Natural Gas Engineering
George E. Trimble Chair in Earth and Mineral Sciences
Graduate Program Chair of Petroleum and Natural Gas Engineering

Luis F. Ayala
Assistant Professor of Petroleum and Natural Gas Engineering

Demian Saffer
Associate Professor of Geosciences

*Signatures are on file in the Graduate School

ABSTRACT

Multiphase flow studies in naturally fractured reservoirs have numerous applications in hydrocarbon recovery, hydrogeology and environmental remediation of subsurface contamination. The presence of natural fractures has significant effects on recovery from oil and gas reservoirs. In these reservoirs, fracture networks serve as better flow paths for fluids, while the porous rock provides storage space. The efficiency of hydrocarbon recovery as well as pollution and contaminant removal from soil and groundwater are mainly controlled by our ability to understand and define fluid transport mechanisms in naturally fractured formations. Appropriate representation of transport properties, such as relative permeability and capillary pressure, is essential for the success of any predictive flow process in permeable media. In addition, the presence of heterogeneities such as fractures, faults, and other geological features adds to the difficulty of assigning flow properties that are representative of the system. The present study focuses on the development and implementation of a numerical model of two-phase flow in fractured rocks showing contrasting rock properties in the form of bedding planes. A unique experimental data set of spontaneous imbibition in a fractured sandstone core is used for the development and verification of the model. This data set consists of a series of high-resolution X-ray computed tomography scans of a rock sample showing local rock heterogeneities, fracture orientation, bedding planes, and fluid saturation as a function of time. An automated history matching approach is proposed to determine relative permeability and capillary pressure curves. A commercial reservoir simulator is used in coordination with an optimization protocol in the proposed history matching

method. Four different synthetic and a semi-synthetic data sets were used to test the automated history matching approach. Absolute permeability and oil relative permeability curves were predicted in those synthetic cases, using different relative permeability representations. In the semi-synthetic case, known relative permeability for the matrix and capillary pressure for both matrix and the fracture were determined simultaneously using experimental spontaneous imbibition data of a heterogeneous fractured core sample. Results of this study indicate that the automated history matching approach was successful in predicting the absolute permeability, relative permeability and capillary pressure. The effects of transport properties on the imbibition process were also investigated by sensitivity analysis. Results from this work improve understanding of multiphase flow in fractured and heterogeneous porous media and ability to predict fluid migration in fractured reservoirs.

TABLE OF CONTENTS

LIST OF FIGURES	vii
LIST OF TABLES	xii
NOMENCLATURE	xiii
ACKNOWLEDGEMENTS	xvi
Chapter 1 Introduction	1
1.1 Problem Statement	3
1.2 Literature Review	4
1.2.1 Modeling of Multi-Phase Flow in Naturally Fractured Reservoirs	4
1.2.2 Spontaneous Capillary Imbibition	8
1.2.3 A Review of Relative Permeability, Capillary Pressure and History Matching for Naturally Fractured Reservoirs	12
Chapter 2 Description of Experimental Data	15
2.1 Experimental Procedure	17
2.2 Experimental Results	19
Chapter 3 Methodology	23
3.1 Preparation of Representative Simulation Model	24
3.2 History Matching	27
3.3 Optimization Algorithm	33
Chapter 4 Implementation of Automated History Matching	36
4.1 Synthetic Cases	36
4.1.1 Estimation of Absolute Permeability	38
4.1.2 Estimation of Relative Permeability to Oil Using Power Law Parameterization	42
4.1.3 Estimation of Relative Permeability to Oil Using Quadratic B- Spline Parameterization	44
4.1.4 Estimation of Relative Permeability to Oil Using Cubic B-Spline	50
4.2 Semi-Synthetic Case	54
4.2.1 Determination of Oil-Water Relative Permeability and Capillary Pressure	57
4.3 Experimental Case	62
4.3.1 Extraction of Time-Dependent Saturation from CT Data	64
4.3.2 Sample Simulation Results	68

Chapter 5 Sensitivity Analysis	85
5.1 Fracture Structure	85
5.2 Matrix Capillary Pressure	98
5.3 Matrix Relative Permeability	106
5.4 Fracture Capillary Pressure.....	111
5.5 Fracture Relative Permeability and Capillary Pressure	115
5.6 Fracture Permeability.....	118
5.7 Capillary Hysteresis in the Matrix	122
Chapter 6 Conclusions	127
References.....	130
Appendix A Representation of Relative Permeability to Oil.....	140
A.1 Quadratic B-Spline Representation	140
A.2 Cubic B-Spline Representation.....	141
Appendix B Sample Matlab and C++ Source Codes for Preparation of the Simulation Model	143
B.1 Subtraction of Dry and Oil-Wet CT Scan Data	143
B.2 Up-Scaling the Subtracted Data.....	147
B.3 Construction of Petro-Physical Data (Porosity and Permeability).....	152
B.4 Extraction of Water-Wet CT Data for Calculating Experimental Saturation.....	154
B.5 Up-Scaling of the Extracted Data and Saturation Calculation.....	157
B.6 Optimization.....	163
B.7 C++ Source Code for Extraction of Required Properties from Simulation Output	164

LIST OF FIGURES

Figure 1-1: Representation of a Naturally Fractured Reservoir (after Warren and Root, 1963)	6
Figure 1-2: Schematic diagrams of connectivity for the standard dual-porosity model (a), the dual-permeability model (b), and the MINC model (c).	8
Figure 2-1: Schematic of fractured sample and CT slice (Karpyn <i>et al.</i> , 2008)	16
Figure 2-2: Schematic of experimental apparatus (Karpyn <i>et al.</i> , 2008)	16
Figure 2-3: Schematic of experimental sequence (Karpyn <i>et al.</i> , 2008)	17
Figure 2-4: Longitudinal view of water saturation distribution at 1072 min in xz direction, parallel to fracture plane	20
Figure 2-5: 3-D Representation of water saturation distribution at 1072 min	21
Figure 2-6: Longitudinal view of water saturation distribution at 1072 min in yz direction, perpendicular to fracture plane	21
Figure 2-7: Water saturation distributions at 1072 min	22
Figure 3-1: Determination of Threshold Value for CT Numbers	25
Figure 3-2: A Schematic Description of Up-scaling Schemes	26
Figure 3-3: Schematic diagram of history matching approach (S_{exp}^* : Experimental Saturation Distribution from X-ray CT imaging)	29
Figure 4-1: 3-D representation of the synthetic model showing depth of the centre of the block. Rectangular face corresponds to fracture plane	38
Figure 4-2: Minimization of objective function with respect to absolute permeability	40
Figure 4-3: Absolute Permeability (k_{abs}) Predictions	41
Figure 4-4: Relative permeability curves using power-law parameterization	43
Figure 4-6: Relative permeability vs water saturation plot using quadratic B-spline parameterization	50
Figure 4-7: Relative permeability curves using cubic B-spline parameterization	53

Figure 4-8: Relative permeability vs water saturation plot using cubic B-spline parameterization	54
Figure 4-9: Representative areal porosity distribution, fraction	56
Figure 4-10: Representative areal permeability distribution, mD	56
Figure 4-11: 3-D representation of the semi-synthetic model showing depth of the centre of the block	57
Figure 4-12: Relative permeability vs. water saturation plot for matrix and fracture	58
Figure 4-13: Capillary pressure vs. water saturation plot for matrix	59
Figure 4-14: Capillary pressure vs. water saturation plot for fracture	59
Figure 4-15: Optimization results as a function of iteration, current value (a), function value (b), step size (c), total function evaluation (d), norm of residuals (e), first-order optimality (f)	62
Figure 4-16: Representative areal permeability distribution, mD	64
Figure 4-17: Experimental water saturations of CT slice located 28.5 mm (a), 9.5 mm (b) and 3 mm (c) above the bottom of the core sample at the end of 1072 min.	66
Figure 4-18: Longitudinal representation of experimental water saturation at the end of 1072 min in yz direction perpendicular to the fracture plane	67
Figure 4-19: Longitudinal representation of experimental water saturation at the end of 1072 min in xz direction parallel to the fracture plane	67
Figure 4-20: 3-D representation of experimental water saturation at the end of 1072 min	68
Figure 4-21: Simulated water saturations of CT slice located 28.5 mm (a), 9.5 mm (b) and 3 mm (c) above the bottom of the core sample at the end of 1072 min.	70
Figure 4-22: Longitudinal representation of simulated water saturation at the end of 1072 min in yz direction perpendicular to the fracture plane	71
Figure 4-23: Longitudinal representation of simulated water saturation at the end of 1072 min in xz direction parallel to the fracture plane	71

Figure 4-24: 3-D representation of simulated water saturation at the end of 1072 min	72
Figure 4-25: Average water saturation in the fracture and in the slice, 3 mm above the bottom of the core	73
Figure 4-26: Water (a) and oil (b) flux for the slice 28.5 mm above the bottom of the core at the end of injection period (4 min).....	75
Figure 4-27: Water (a) and oil (b) flux for the slice 3 mm above the bottom of the core at the end of injection period (4 min)	76
Figure 4-28: Water (a) and oil (b) flux for the slice 28.5 mm above the bottom of the core at early-time period (5 min)	78
Figure 4-29: Water (a) and oil (b) flux for the slice 3 mm above the bottom of the core at early-time period (5 min)	79
Figure 4-30: Water (a) and oil (b) flux for the slice 28.5 mm above the bottom of the core at intermediate-time period (10 min)	80
Figure 4-31: Water (a) and oil (b) flux for the slice 3 mm above the bottom of the core at intermediate-time period (10 min)	81
Figure 4-32: Water (a) and oil (b) flux for the slice 28.5 mm above the bottom of the core at late-time period (120 min)	82
Figure 4-33: Water (a) and oil (b) flux for the slice 3 mm above the bottom of the core at late-time period (120 min)	83
Figure 5-1: Comparison of up-scaling schemes, factor of 5 in all directions (a), factor of 7 in x, y and factor of 10 in z direction (b), and factor of 10 in all directions (c)	87
Figure 5-2: Longitudinal (xz) representation of the reservoir model with discontinuous fracture structure (blue: fracture, red: matrix).....	88
Figure 5-3: Cross-sectional (xy) representation of the reservoir model with discontinuous fracture structure (blue: fracture, red: matrix).....	88
Figure 5-4: Longitudinal (xz) representation of the reservoir model with continuous fracture structure (blue: fracture, red: matrix).....	89
Figure 5-5: Cross-sectional (xy) representation of the reservoir model with continuous fracture structure (blue: fracture, red: matrix).....	89
Figure 5-6: Capillary pressure vs water saturation for matrix and fracture	91

Figure 5-7: Relative permeability vs water saturation for matrix and fracture.....	91
Figure 5-8: Cross-sectional (xy) water saturation distribution of the slice 3 mm above the bottom of the core model with discontinuous fracture structure.....	94
Figure 5-9: Longitudinal (xz) water saturation distribution of the core model with discontinuous fracture structure.....	95
Figure 5-10: Cross-sectional (xy) water saturation distribution of the slice 3 mm above the bottom of the core model with continuous fracture structure	96
Figure 5-11: Longitudinal (xz) water saturation distribution of the core model with continuous fracture structure	97
Figure 5-12: Average water saturation in the fracture as a function of time	98
Figure 5-13: Capillary pressure vs water saturation for matrix and fracture	99
Figure 5-14: 3-D Representations of water saturation distribution for the model developed by using Pc_matrix_1 curve (base)	101
Figure 5-15: 3-D Representations of water saturation distribution for the model developed by using Pc_matrix_2 curve	102
Figure 5-16: 3-D Representations of water saturation distribution for the model developed by using Pc_matrix_3 curve	103
Figure 5-17: Average water saturation in the fracture as a function of time	105
Figure 5-18: Average water saturation in the slice 3 mm above the bottom of the model as a function of time	105
Figure 5-19: Matrix relative permeability vs water saturation	106
Figure 5-20: Cross-sectional (xy) water saturation distribution of the slice 3 mm above the bottom of the core model with the second sets of relative permeability	107
Figure 5-21: Cross-sectional (xy) water saturation distribution of the slice 3 mm above the bottom of the core model with the third sets of relative permeability	109
Figure 5-22: Average water saturation in the fracture as a function of time	110
Figure 5-23: Average water saturation in the slice 3 mm above the bottom of the model as a function of time	110

Figure 5-24: Capillary pressure vs water saturation for matrix and fracture	111
Figure 5-25: Longitudinal (xz) water saturation distribution of the core model developed by using Pc_fracture_2 curve	112
Figure 5-26: Longitudinal (xz) water saturation distribution of the core model developed by using Pc_fracture_3 curve	114
Figure 5-27: Average water saturation in the fracture as a function time	115
Figure 5-28: Average water saturation in the fracture as a function of time	116
Figure 5-29: 3-D Representations of water saturation distribution for the model with zero Pc & straight-line relative permeability in the fracture	117
Figure 5-30: Average water saturation in the fracture as a function of time	119
Figure 5-31: Longitudinal (xz) water saturation distribution of the core model with 500 mD of fracture permeability	120
Figure 5-32: Longitudinal (xz) water saturation distribution of the core model with 6000 mD of fracture permeability	121
Figure 5-33: Imbibition and drainage capillary pressure curves for matrix	123
Figure 5-34: Cross-sectional (xy) water saturation distribution of the slice 3 mm above the bottom of the core model with capillary hysteresis effect in the matrix	125
Figure 5-35: Average water saturation in the slice 3 mm above the bottom of the model as a function of time	126
Figure 5-36: Average water saturation in the fracture as a function of time	126

LIST OF TABLES

Table 4-1: Reservoir Rock and Fluid properties.....	37
Table 4-2: Initial Guesses and Estimated Absolute Permeability Values.....	40
(Target $k_{abs}=500$ mD).....	40
Table 4-3: Absolute Permeability Predictions	41
Table 4-4: Initial and Target values for power-law parameterization	42
Table 4-5: Control Points for Quadratic B-spline Representation.....	44
Table 4-6: End Control Points for Quadratic B-spline Representation	44
Table 4-7: Objective Function Distribution for Quadratic B-spline Parameterization	48
Table 4-8: Estimated transformed variables and control points	49
Table 4-9: Control Points for Cubic B-spline Representation	50
Table 4-10: End Control Points for Cubic B-spline Representation.....	51
Table 4-11: Imaginary Control Points for Cubic B-spline Representation.....	51
Table 4-12: Estimated transformed variables and control points	53
Table 4-13: Reservoir Rock and Fluid Properties (Semi-Synthetic Case)	55

NOMENCLATURE

Symbols:

N_B : Bond number

H : Length of core, cm

k : Permeability, cm²

k_{abs} : Absolute permeability, mD

g : Acceleration due to gravity, cm / s²

J : Objective function

S^{cal} : Predicted fluid saturation distribution, fraction

S^{exp} : Experimental fluid saturation distribution, fraction

kr : Relative permeability

P_c : Capillary pressure, kPa

P_c^* : End-point capillary pressure, kPa

a : Controlling parameter for relative permeability

b : Controlling parameter for relative permeability

a_{pc} : Controlling parameter for capillary pressure

b_{pc} : Controlling parameter for capillary pressure

S_e : Effective saturation, fraction

S_{or} : Residual oil saturation, fraction

S_w : Water saturation, fraction

- S_{wavg} : Average water saturation, fraction
- S_{wpixel} : Water saturation in pixel, fraction
- S_{wirr} : Irreducible water saturation, fraction
- CS_w : x coordinate of the control point
- Ckr : y coordinate of the control point
- CP_c : Capillary pressure constant for matrix
- CP_{cf} : Capillary pressure constant for fracture
- t : Variable along the B-spline curve
- s : Trial step size
- q : Representative function of the objective function
- N : Neighborhood
- f : Objective function in trust region algorithm
- H : Hessian matrix
- s^T : Transpose of trial step size matrix
- g : Gradient of f
- D : Diagonal scaling matrix
- $\|\cdot\|$: 2-norm of the matrix
- C_i : i^{th} control point
- y_i : Transformed variable of the i^{th} control point
- $CT_{subtracted}$: CT number of phase subtracted core

CT_{wet} : CT number of fluid saturated core

CT_{vacuum} : CT number of core under vacuum

S_s : Specific surface area

Greek:

ϕ : Porosity, fraction

σ : Interfacial tension, mN / m

$\Delta\rho$: Density difference, g/cm³

Δ : Positive scalar

ϕ_{pixel} : Porosity in pixel

ϕ_{avg} : Average porosity

τ : Tortuosity

Abbreviations:

CT : Computerized Tomography

DR : Digital Radiography

MINC : Multiple interacting continua

EMA : Effective medium approach

CMG : Computer modeling group

IMEX : The black oil module of CMG

min : Minimum

NaN : Not a number

IFT : Interfacial tension

ACKNOWLEDGEMENTS

I would like to take this opportunity to express my sincere appreciation and gratitude to people who had contributed to my graduate study and my life experience at Penn State. This study would not have been accomplished without their support and friendship.

First and foremost, I would like to thank my thesis advisor and mentor, Dr. Zuleima T. Karpyn, for her constant support and guidance throughout the course of my entire study. She has been very helpful, encouraging and patient during challenging periods both in my research and my personal life. I am very indebted to her for supporting me throughout the research and life-learning experience at Penn State.

I am grateful to Dr. Luis F. Ayala for his encouraging attitude during the initial stage of my admission process to Penn State as well as sharing his valuable suggestions and experiences with me during my graduate study. I would also like to thank him for providing me the financial support for the last semester, which contributed significantly to maintain my life at Penn State.

I would like to extend my appreciation to my other thesis committee members, Dr. Turgay Ertekin and Dr. Demian Saffer, for their interest in serving as committee members. Their indispensable suggestions and contributions to this work are truly appreciated.

My final gratitude goes to my colleagues and all my friends who supported and helped me during my academic and personal life at Penn State. I am very thankful to Dr. Emre Artun, Doruk Alp, Dr. Claudia Parada, Sultan Al-Enezi and Dr. Murat Yasar for

their help and their suggestions, which contribute to solve problems encountered during my research. I am indebted to my friends Dr. Emin Caglan Kumbur and Yasemin Mohammad for their emotional support and encouragement throughout my entire study. I would also like to thank Baris Ozcan, Mehmet Tarman, Ani -Umut Gokcesu, Seyit-Nuran Ural, Ahmet Turan, Pamir Cirdi, Oyku Asikoglu, Ceyda Coruh, Safakcan Tuncdemir, Ozhan-Sinem Turgut, Ali-Esra Akturk, Emre Kultursay, Zeki Ozgur Gokce and all others for being great friends and sharing wonderful moments during the past few years.

This work is dedicated to my parents, A. Yasar and Nezaket Basbug for their understanding, endless patience and valuable support. Today, I would not have been in this position without their courage and help.

Chapter 1

Introduction

Naturally fractured reservoirs, corresponding to a large amount of world oil and gas reserves, are caused by the deformation in the earth crust due to local variations in stress distribution. An interconnected fracture network provides substantial flow paths for fluids, while the adjacent matrix blocks provide pore spaces to store the fluid. Gravity and capillary forces are important driving forces that allow fluid transport in naturally fractured reservoirs. Spontaneous capillary imbibition is also an important recovery mechanism for oil and gas reservoirs. Recent studies on modeling of spontaneous imbibition indicate the importance of transport properties such as relative permeability and capillary pressure curves in describing the fluid flow in fractured rocks. However, the complexity in the determination of these curves for both matrix and fractures, and their relative importance has not been resolved yet.

The main objective of this study is to investigate the relative importance of transport properties on spontaneous imbibition in addition to construct a 3-D numerical model of two-phase flow (oil-water) in fractured Berea sandstone. The numerical model mainly focuses on modeling of spontaneous, countercurrent capillary imbibition in naturally fractured porous media. An automated history matching approach is proposed to construct the relative permeability and capillary pressure curves for a system of known saturation history. The nature of the present work is mostly numerical, although an experimental data set of spontaneous imbibition is presented and used for the validation

of the model. In the previous experimental study (Karpyn *et al.*, 2008), a high-resolution Computerized Tomography system (CT scanner) was used to map the fracture, characterize bedding planes, heterogeneities in the rock, and saturation history during spontaneous imbibition. In the present study, different synthetic and semi-synthetic data sets of spontaneous imbibition were utilized to test the proposed automated history matching method. A commercial reservoir simulator (CMG) coupled with the Optimization Toolbox of MATLAB[®] R2006b were used to determine the absolute permeability and the parameters that control the shape of the relative permeability and capillary pressure curves.

Results of this study would provide a mechanistic explanation for spontaneous, countercurrent imbibition in naturally fractured reservoirs through experimental and numerical analysis. It would also improve understanding of multiphase flow in fractured and heterogeneous porous media and our ability to predict fluid migration in fractured reservoirs.

1.1 Problem Statement

In naturally fractured water drive reservoirs, spontaneous capillary imbibition can be an effective recovery mechanism to produce the oil in the matrix adjacent to a fracture. This process occurs in countercurrent manner between the matrix and fracture when the wetting and non-wetting phases flow in opposite directions. Both drainage and imbibition processes exist, simultaneously, during countercurrent flow, although at different locations. Modeling spontaneous, countercurrent flow and the associated hysteretic processes has been a challenging problem due to the complexity of the matrix-fracture interaction. Determination of the appropriate relative permeability and capillary pressure curves for both matrix and fracture, including drainage and imbibition path, presents an interesting challenge. Thus, the main objectives of this study are:

1. To improve understanding of spontaneous imbibition and ability to predict fluid migration in fractured and heterogeneous porous media.
2. To investigate the relative importance of transport properties on spontaneous capillary imbibition and the displacement of oil residing in the rock matrix.
3. To construct a 3-D numerical model of spontaneous, countercurrent imbibition in a fractured core sample.
4. To propose a method to determine relative permeability and capillary pressure characteristics from experimental observations of spontaneous imbibition in fractured sandstone.

1.2 Literature Review

1.2.1 Modeling of Multi-Phase Flow in Naturally Fractured Reservoirs

A considerable amount of the world hydrocarbon reservoirs are naturally fractured (Bourblaux and Kalaydjian, 1990; Cil *et al.*, 1998; Kang *et al.*, 2006). Studies of fluid flow and transport in fractured rock have received increasing interest in the last decades. Those studies have numerous applications in hydrocarbon recovery, hydrogeology, and environmental remediation of subsurface contamination. Therefore, understanding the fundamental flow characteristics in fractured rocks is of great importance for designing effective recovery processes from oil, gas, and geothermal reservoirs, controlling migration and distribution of contaminants in the subsurface, and improving underground fluid storage. Since the 1960s, significant progress has been encountered in numerical simulation of fluid flow and transport processes in fractured reservoirs (Kang *et al.*, 2006). Many numerical modeling approaches and techniques have been proposed by researchers to develop petroleum and geothermal reservoirs as well as to resolve subsurface contamination problems (Barenblatt *et al.*, 1960; Kazemi and Merrill, 1979; Kazemi, 1969; Pruess and Narasimhan, 1985; Warren and Root, 1963).

One of the most common techniques to model multi-phase flow in a fractured porous medium is the conventional continuum model, in which governing equations and essential relationships are approximated to build a numerical model. In continuum models, the reservoir is discretized into two distinct spatial domains namely, matrix and fracture. One major assumption is that the matrix continuum consists of matrix blocks surrounded by fractures. Matrix block dimensions can vary throughout the reservoir and

are related to fracture spacing, orientation, and width (Akin, 2001). Matrix blocks usually have a very low-permeability and higher effective-porosity compared to adjacent fractures having a high-permeability and low effective-porosity. Bossie-Codreanu *et al.* (1985) suggested that fracture permeabilities may be 100 and even over 10000 times higher than permeability within the matrices. Therefore, the fracture network can provide a preferential flow path for fluids while matrix blocks store the fluids.

Four different continuum models for naturally fracture reservoirs are proposed in the literature (Pruess and Narasimhan, 1985; Warren and Root, 1963; Gilman and Kazemi, 1988; Fung, 1988). Each has unique description of the flow in a fractured reservoir. The first one is the standard dual porosity model where fluids propagate in the fracture network through the reservoir and matrices are treated as source and sink terms (Warren and Root, 1963). The geometrical idealization in this model is comprised of rectangular parallelepiped blocks separated by vertical and horizontal vertical intersecting fractures (Ayala, 2004), which is also known as the “sugar-cube model” (Warren and Root, 1963). A schematic drawing of the sugar-cube model is given in Fig. 1-1. Warren and Root (1963) proposed in their study that two porosities are necessary to describe every point in a naturally fractured reservoir effectively. Primary porosity associated with the matrix blocks and secondary porosity related to fractures are the two porosities in a naturally fractured reservoir that they introduced. There is no permeability associated with the matrix since Darcian flow occurs in the fracture network throughout the reservoir in naturally fractured reservoirs. This approach is also known as the dual porosity (fracture and matrix) and single permeability (fracture) model. This analytical

model for single-phase flow is extended by 3-D and multiphase numerical approaches developed by Kazemi *et al.* (1976) and Thomas *et al.* (1983).

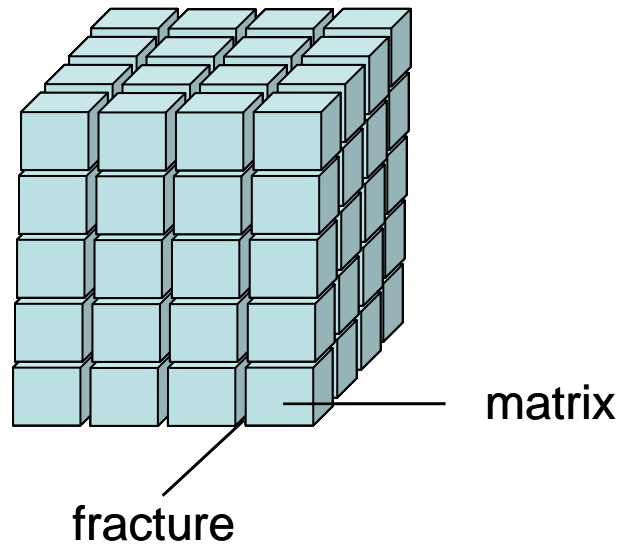


Figure 1-1: Representation of a Naturally Fractured Reservoir (after Warren and Root, 1963)

In 1985, the “dual permeability” concept was introduced by Hill and Thomas (1985), which assumes that Darcian flow occurs in both the fracture blocks and the neighboring matrix blocks. Quandalle and Sabathier (1989) and Gilman and Kazemi (1988) proposed two numerical simulation models based on dual porosity, dual-permeability approaches. According to Gilman and Kazemi (1988), the dual porosity model provided less number of grid blocks compared to single porosity approach, which made it most practical and widely used method for the simulation of naturally fractured reservoirs. The third one is the multiple-interacting continua (MINC) model (Pruess and Narasimhan, 1985) that utilizes a nested discretization of the matrix blocks. The nested

structure of the matrix-fracture transfer enables very effective description of the transient flow regime that is usually neglected by the standard dual porosity model. The disadvantage of this model is that it neglects the effects of the gravity forces even though it can represent the pressure, viscous, and capillary forces. The sub-domain model (Fung, 1988) is a modification of the standard dual porosity model in which matrix blocks are refined in the vertical direction to account for the gravity drainage process from the matrix block to fracture more adequately. The connectivity structure of those continuum models are presented in Fig. **1-2**. A comprehensive literature review on the progress of the numerical simulation of naturally fractured reservoirs can be obtained in the works of Bossie-Codreanu *et al.* (1985) and Kazemi and Gilman (1993).

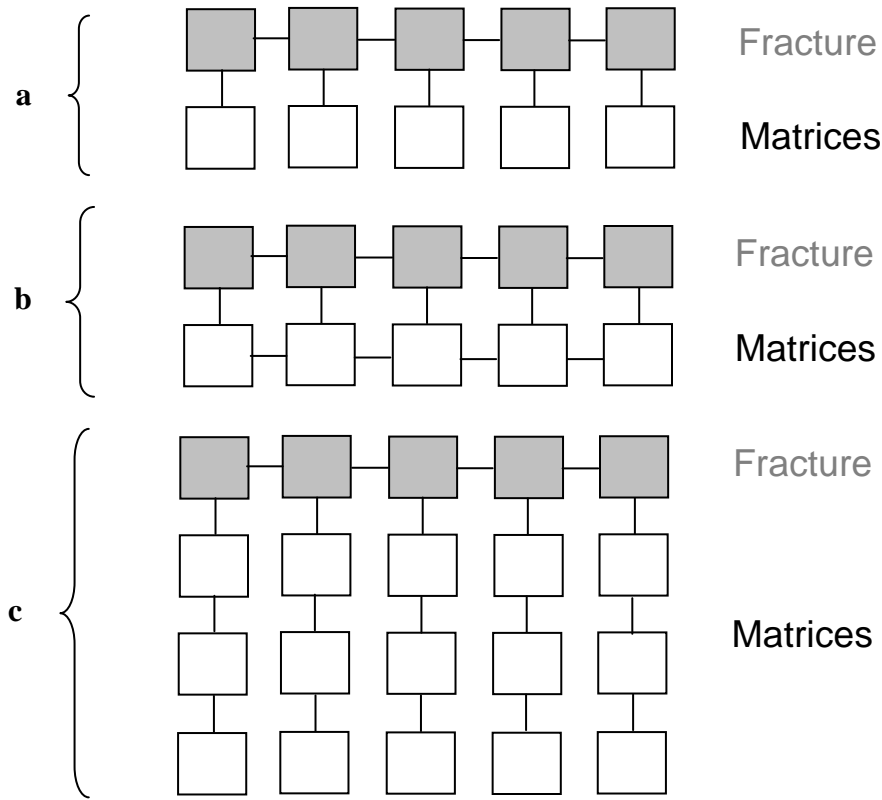


Figure 1-2: Schematic diagrams of connectivity for the standard dual-porosity model (a), the dual-permeability model (b), and the MINC model (c).

1.2.2 Spontaneous Capillary Imbibition

In order to develop a realistic numerical model of fluid flow in naturally fractured reservoirs, the fundamental matrix-fracture interactions as well as the effects of transport properties on the fluid flow has to be well analyzed. In water drive reservoirs, capillary imbibition is generally the driving force to produce oil in the matrix surrounded by a fracture (Lee and Kang, 1999). If a fluid having wetting affinity to the rock exists in the fractures, spontaneous imbibition will be the dominant transport mechanism that affects the displacement of non-wetting fluids stored in the matrix (Karpyn *et al.*, 2008).

Spontaneous imbibition in which non-wetting phase is displaced by the wetting phase occurs in both co-current and countercurrent manner in naturally fractures reservoirs (Bourblaux and Kalaydjian, 1990; Parson and Chaney, 1966; Iffly *et al.* 1972; Hamon and Vidal, 1986; Al-Lawati and Saleh, 1996; Pooladi-Darvish and Firoozabadi, 2000). In co-current flow, the wetting and non-wetting phases flow in the same direction while the wetting phase pushes the non-wetting phase out of the matrix. In countercurrent flow, the wetting and non-wetting phases flow in opposite directions. The relative importance of each flow mechanism depends on boundary conditions and the ratio of gravity to capillary forces (Bourblaux and Kalaydjian, 1990; Pankaj and Kishore, 2004) which is represented by Bond number (Schechter *et al.*, 1994). The Bond number is defined by the following Eq. **1.1**:

$$N_B = \frac{\Delta\rho g H}{C \sigma \sqrt{\phi/k}} \quad \mathbf{1.1}$$

$C = 0.4$ for capillary tube model (Zhou and Stenby, 1989)

H : Length of core (cm)

ϕ : Porosity

k : Permeability (cm²)

$\Delta\rho$: Density difference between two immiscible phases (g / cm³)

σ : Interfacial tension (IFT) (mN / m)

g : Acceleration due to the gravity (cm / s²)

In water-wet rocks, for low Bond numbers ($N_B < 1$), the spontaneous imbibition is dominated by capillary forces and takes place from the entire exposed surface of the porous matrix (countercurrent imbibition). However, for high bond numbers ($N_B > 1$), gravity forces are dominant where the non-wetting phase exit the porous matrix from the top and wetting-phase is imbibed from the bottom (co-current imbibition). Both gravity and capillary forces are effective in spontaneous imbibition at intermediate Bond numbers.

In last two decades, most of the spontaneous imbibition studies have focused on the countercurrent imbibition. The mathematical formulation of countercurrent imbibition is given as a form of a nonlinear diffusion equation in the study of Marle (1981). McWhorter and Sunada (1990), Chen (1988) and Chen *et al.* (1990) presented analytical and semi-analytical solutions of countercurrent flow equation by assuming a semi-infinite domain. In 2005, a semi-analytical approach expressing gravity-dominated and capillary dominated countercurrent imbibition in both weakly and strongly-wet rocks was proposed by Tavassoli *et al.* (2005) to support dual-porosity modeling of flow in fractured reservoirs. Another approximate analytical solution for one dimensional, linear, countercurrent spontaneous imbibition has been presented recently by Ruth *et al.* (2007).

There are numerous experimental works on countercurrent imbibition in the literature. In these experiments, the oil saturated cores are either exposed to water in all directions or sealed such that water displaces the oil through the same face (Mattax and Kyte, 1962; Iffly *et al.*, 1972; Du Prey, 1978; Hamon and Vidal, 1986; Cuiec *et al.*, 1994; Zhang *et al.*, 1996). In some co-current imbibition studies, oil production was observed

from a face that is not covered by water (Iffly *et al.*, 1972; Hamon and Vidal, 1986; Parsons and Chaney, 1966; Kleppe and Morse, 1974). The majority of these studies could not clarify the differences between co-current and countercurrent imbibition (Pooladi-Darvish and Firoozabadi, 2000). However, detailed experimental studies (Bourblaux and Kalaydjian, 1990; Pooladi-Darvish and Firoozabadi, 2000; Morrow and Mason, 2001) have demonstrated significant recovery differences between co-current and countercurrent imbibition. The importance of co-current and countercurrent flow in fractured petroleum reservoirs was also illustrated by several experimental studies (Firoozabadi and Markeset, 1992; Baldwin and Spinler, 1999; Hatiboglu and Babadagli, 2004; Karpyn *et al.*, 2008).

In recent years, more numerical model studies supporting experimental findings of countercurrent spontaneous imbibition were presented in the literature. Li *et al.* (2005) attempted to simulate countercurrent flow experiments to identify the importance of relative permeability and capillary pressure curves with hysteretic components. In 2006, Behbahani *et al.* (2006) performed one and two dimensional simulation of countercurrent imbibition and compared his findings with experimental measurements. Similar experimental and numerical comparisons of countercurrent imbibition were illustrated in the literature (Standnes, 2006; Hognesen *et al.*, 2006). Fischer *et al.* (2008) stated the necessity of an appropriate numerical model of spontaneous imbibition which can be validated by laboratory experiments and presented a detailed modeling study emphasizing the importance of viscosity ratio and boundary conditions in the simulation of spontaneous imbibition. A detailed literature review of countercurrent imbibition can be found in the work of Pankaj and Kishore (2004).

1.2.3 A Review of Relative Permeability, Capillary Pressure and History Matching for Naturally Fractured Reservoirs

After describing the matrix-fracture transport mechanisms in naturally fractured reservoirs, the determination of the correct set of relative permeability and capillary pressure curves become important to develop powerful numerical models which are used for estimating the productivity, injectivity and ultimate recovery from hydrocarbon reservoirs. Especially, defining the correct relative permeability and capillary pressure curves for the fractures is difficult due to the complexity of the matrix-fracture systems. Most engineers have mostly used straight-line relative permeabilities and zero capillary pressure to simulate the fluid flow in fractured reservoirs (De la Porte *et al.*, 2005). Conventional straight-line relative permeability curves were introduced by Romm (1966) after conducting an experimental study in fractures. According to his results, phase relative permeability and phase saturations were linearly dependent, and zero capillary pressure was observed for fractures. His experiments were based on the fluid flow between two parallel plates where the effects of fracture aperture and roughness were not investigated (De la Porte *et al.*, 2005). In 1990, Firoozabadi and Thomas (1990) introduced non-zero capillary pressures where the recoveries were changed drastically using wettability concept combined with the enhanced oil recovery techniques. Another model was proposed by Firoozabadi and Hauge (1990) to calculate the capillary pressures of fractures within a system where fracture characteristics such as waviness, roughness, width, and interfacial tension were considered. Rossen and Kumar (1992) suggested a method for calculating non-straight line relative permeabilities in fractures using Effective Medium Approach (EMA). In this approach, effects of gravity and aperture

distribution on relative permeabilities were analyzed where two phase flow in fracture networks was not allowed. In 1994, Pieters and Graves (1994) utilized video-imaging technique to monitor saturation distribution in fractures, which validates the non-linear behavior of relative permeability. Similar tendency for relative permeability in fractures were observed in the study of Range-German *et al.* (1998) using a computerized tomography scanner. Furthermore, Bertels *et al.* (2001) proposed an experimental technique to measure and compute fracture aperture distribution, capillary pressure, and relative permeability in fractured rocks using CT scanning. A more comprehensive review of relative permeability and capillary pressure for fractures is illustrated in (Rangel-German and Kavscek, 2005).

After the 1960s, history matching technique, where relative permeabilities and capillary pressure as well as absolute permeability, and porosity are adapted using a reservoir simulator was introduced to achieve a reservoir representation in an agreement with the observed reservoir performance. The first study on history matching was done by Kruger (1961). He calculated the areal permeability distribution of the reservoir using history matching approach. Archer *et al.* (1973) applied similar approach in reservoir characterization and description to obtain relative permeabilities from coreflood experiments. Capillary pressures as well as relative permeabilities were determined by Chavent *et al.* (1980) with automated history matching. With the improvement of computerized technology, the automated history matching technique has been extensively applied in coreflood analysis by several researches (Kerig and Watson, 1987; Akin and Demiral, 1997; Akin and Kavscek, 1999). Al-Wadahi *et al.* (2000) and Li *et al.* (2003) studied the applications of this technique in counter-current flow using X-ray

computerized tomography. Similar history matching study was done by Alajmi (2003) to investigate the influence of a fracture tip on two-phase flow displacement processes. In 2005, a novel methodology in which fracture intensity was conditioned to the production data was introduced by Cui and Kelkar (2005). A case study of automated history matching in naturally fractured reservoirs was also presented as an implementation of the proposed novel approach to investigate the effect of fracture intensity controlling the fracture permeability and the dimensions of matrix blocks on the production data. In addition, Gang and Kelkar (2006) proposed an efficient history matching approach to examine the impact of fracture permeability on the production data.

In the present work, a similar automated history matching approach was developed to obtain the capillary pressure and relative permeability curve for both matrix and fracture during spontaneous, countercurrent imbibition. The experimental saturation distribution obtained from Computerized Tomography (CT) was used to validate the accuracy of the history matching approach. Although some researches showed that straight-line representation may not be correct to describe the relative permeability of the fractures, this representation of relative permeability curve for fractures is still widely used in numerical simulation studies. Because of this conflict, some additional work should be done to determine the appropriate relative permeability and capillary pressure curves representing spontaneous imbibition in matrix-fracture systems.

Chapter 2

Description of Experimental Data

A unique experimental data set of capillary imbibition in a fractured sandstone core is available in this study to develop and validate our numerical model. A two-phase (oil-water) experiment was previously conducted to study spontaneous capillary imbibition in fractured porous media (Karpyn *et al.*, 2008). Calcite-cemented Berea sandstone with 5% clay content was used in this experiment. Porosity ranges between 15-22 % and unconfined compressive strength ranges from 6 to 15 ksi (Clark, 1966). The sample was cored parallel to bedding planes and artificially fractured perpendicular to bedding planes with a modified Brazilian test. The rock sample was 47.5 mm long and 25.4 mm in diameter with a single longitudinal fracture with open ends. The fracture has a mean aperture of 0.16 mm, 0.19 cm³ pore volume, and 4 % contact area. Fig. 2-1 illustrates a schematic representation of the fractured sample and a CT scan cross-section. The viscosities of oil and water phases were 5.0 cp and 1.2 cp, respectively.

The experimental apparatus contained a multi-phase fluid flow system, an X-ray transparent core holder assembly, and a high-resolution X-ray Computed Tomography system (CT scanner). A schematic drawing of the experimental apparatus is introduced in Fig. 2-2.

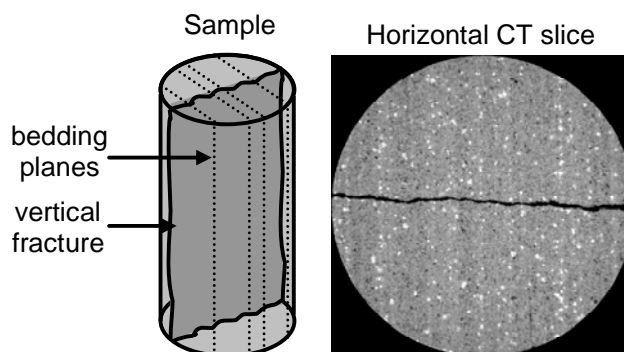


Figure 2-1: Schematic of fractured sample and CT slice (Karpyn *et al.*, 2008)

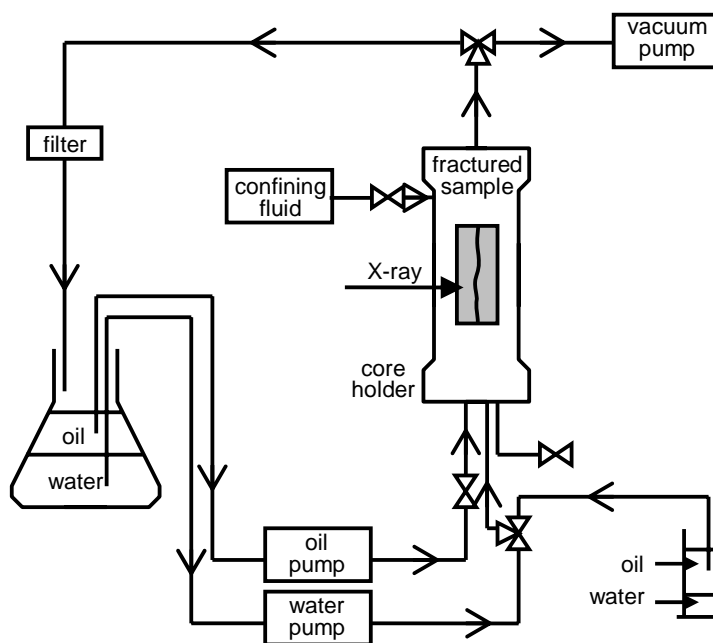


Figure 2-2: Schematic of experimental apparatus (Karpyn *et al.*, 2008)

2.1 Experimental Procedure

A schematic representation of the experimental procedure is illustrated in Fig. 2-3. The bedding planes are perpendicular to the plane of the fracture and parallel to the direction of gravity (Fig.2-3.a). The core sample was originally vacuum saturated with oil (Fig.2-3.b). Nearly one fracture pore volume, 0.2 cm^3 , of water was injected upwards into the fracture for a period of 4 min (Fig.2-3.c). The system was shut in and monitored regularly using Digital Radiography (DR) and high-resolution CT scanner. Computed Tomography scans are single slices through a three-dimensional object where as a single view of the sample is acquired by Digital Radiography. DR was used to monitor early-time saturation changes in the entire core which could not be achieved using slower 3-D tomography images.

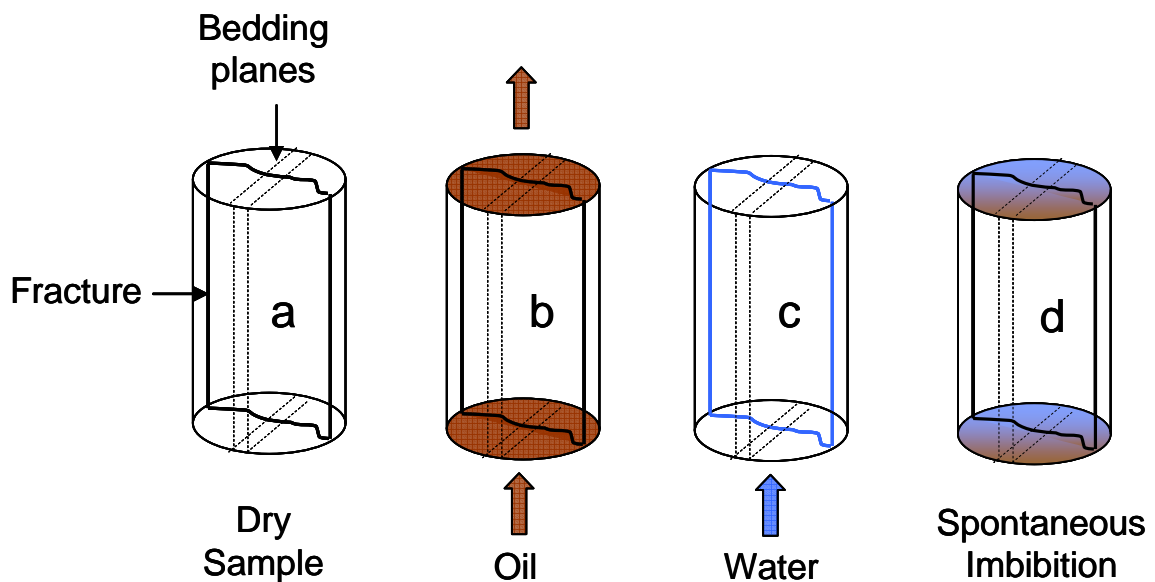


Figure 2-3: Schematic of experimental sequence (Karpyn *et al.*, 2008)

A successful representation of porosity, permeability and fluid saturation distributions is significant to better understand the fundamental characteristics of multi phase flow in porous media. X-ray computerized tomography (CT) technique has evolved as a powerful tool for non-destructive imaging since it is relatively easy to utilize, adjustable to many types of experimental procedures and conditions, and can provide fine spatial resolution. In comparison to conventional X-ray radiography, CT scanners create cross-sectional images of the object by computing the attenuation of a beam of X-rays as it is rotated around the object at angular increments within a single plane.

In the previously presented work (Karpyn *et al.*, 2008), artificially fractured Berea sandstone was studied through visualization and quantification using CT scanner. This technology allows spatial pixel resolution varying between 20 and 50 microns. Several two-dimensional slices generate three-dimensional digital core at this resolution. The CT system is comprised from an ionized X-ray source, a detector, a translation system, and a computer in order to monitor fluid migration and data acquisition. The sample was rotated 360 degrees in the X-ray beam while the detector offers attenuation views to the data acquisition computer. After a complete rotation of the sample, a cross-sectional image of the attenuation values which represents a combination of the density and the apparent atomic number of the sample and the imaged position was regenerated. After each rotation, the sample is repositioned for a new scan leading to a continuous 3-D coverage of the sample.

2.2 Experimental Results

Experimental results obtained by Karpyn *et al.* (2008) indicated that co-current and countercurrent flow coexist during the spontaneous capillary imbibition process. Early, intermediate and late-time were the three distinctive flow intervals that could be distinguished during the spontaneous imbibition process. The duration of these intervals is dependent on rock and fluid properties, sample dimensions and boundary conditions. The shape of the advancing front is controlled by the presence of bedding planes in the rock's structure at early time. The imbibing front propagates through low porosity/permeability layers due to higher capillary forces. During the intermediate interval, cross-layer fluid exchange has a tendency to level the imbibing front. Countercurrent flow, perpendicular to plane of fracture, is more dominant during the early and intermediate intervals compared to co-current flow. There are some localized zones in which drainage and imbibition are taking place with a transition cross-point that moves away from the fracture as imbibition advances. Saturation gradients in the vertical direction are stabilized by an upward co-current flow during the late time imbibition where co-current and countercurrent flow mechanisms coexist (Karpyn *et al.*, 2008).

This experimental study where resulting water saturation distributions are illustrated through Fig. 2-4 - Fig. 2-6 was used to validate the proposed automated history matching in which relative permeability and capillary pressure curves were generated. Fig. 2-4 shows the 3-D representation of water saturation distribution at the end of experiment. Fig. 2-5 and Fig. 2-6 represent orthogonal water saturation distributions in the xz and yz direction obtained at the end of experiment ($t = 1072$ min), respectively.

Individual slice representations of saturation distribution for slices 576, 864 and 1152 (top to bottom) are given in Fig. 2-7. The resulting relative permeability and capillary pressure curves provide a basis for the determination of flow properties of similar spontaneous imbibition processes. The impacts of rock heterogeneity on spontaneous imbibition were also analyzed during the remaining study. The validation of the proposed methodology allows us to understand the basic characteristics of the spontaneous, countercurrent imbibition in naturally fractured reservoirs.

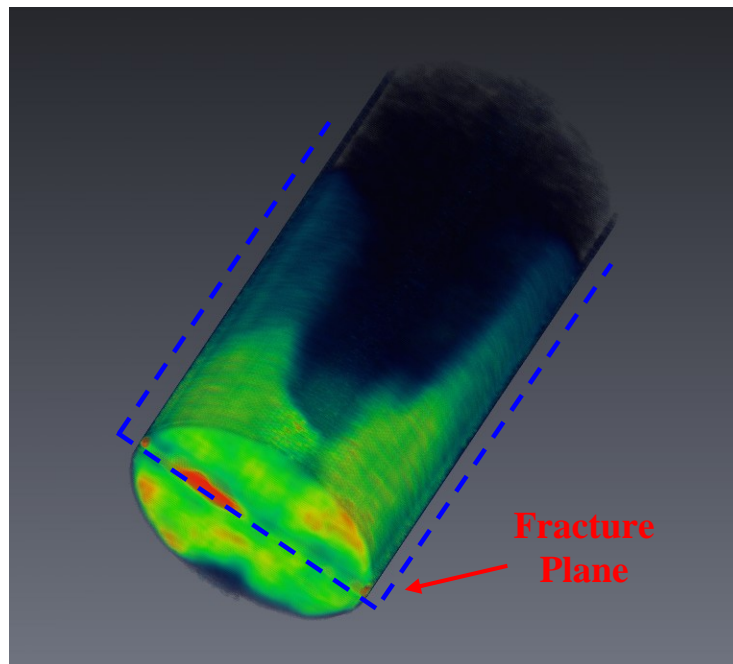


Figure 2-4: Longitudinal view of water saturation distribution at 1072 min in xz direction, parallel to fracture plane

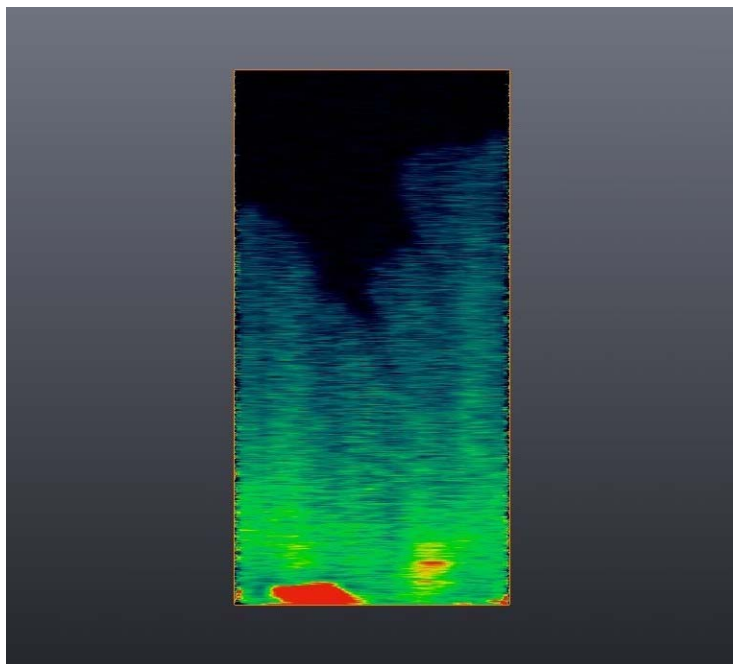


Figure 2-5: 3-D Representation of water saturation distribution at 1072 min

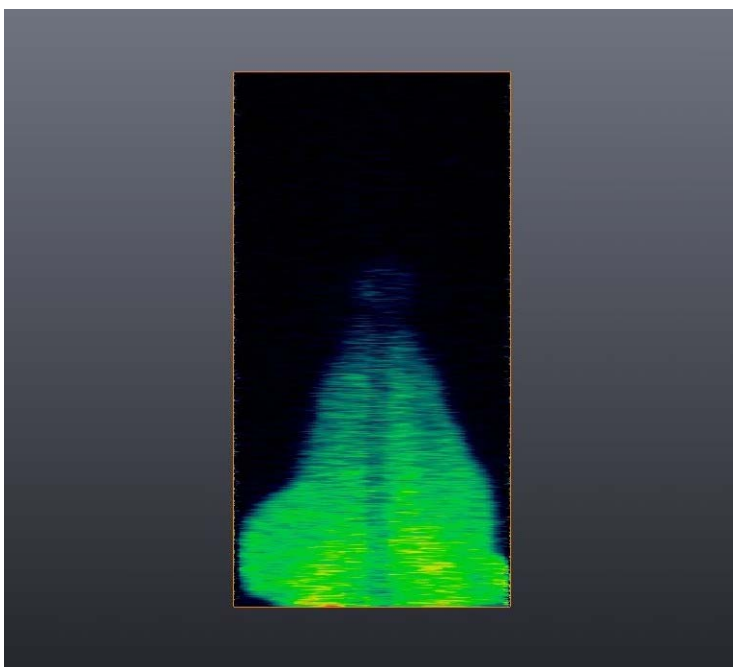


Figure 2-6: Longitudinal view of water saturation distribution at 1072 min in yz direction, perpendicular to fracture plane.

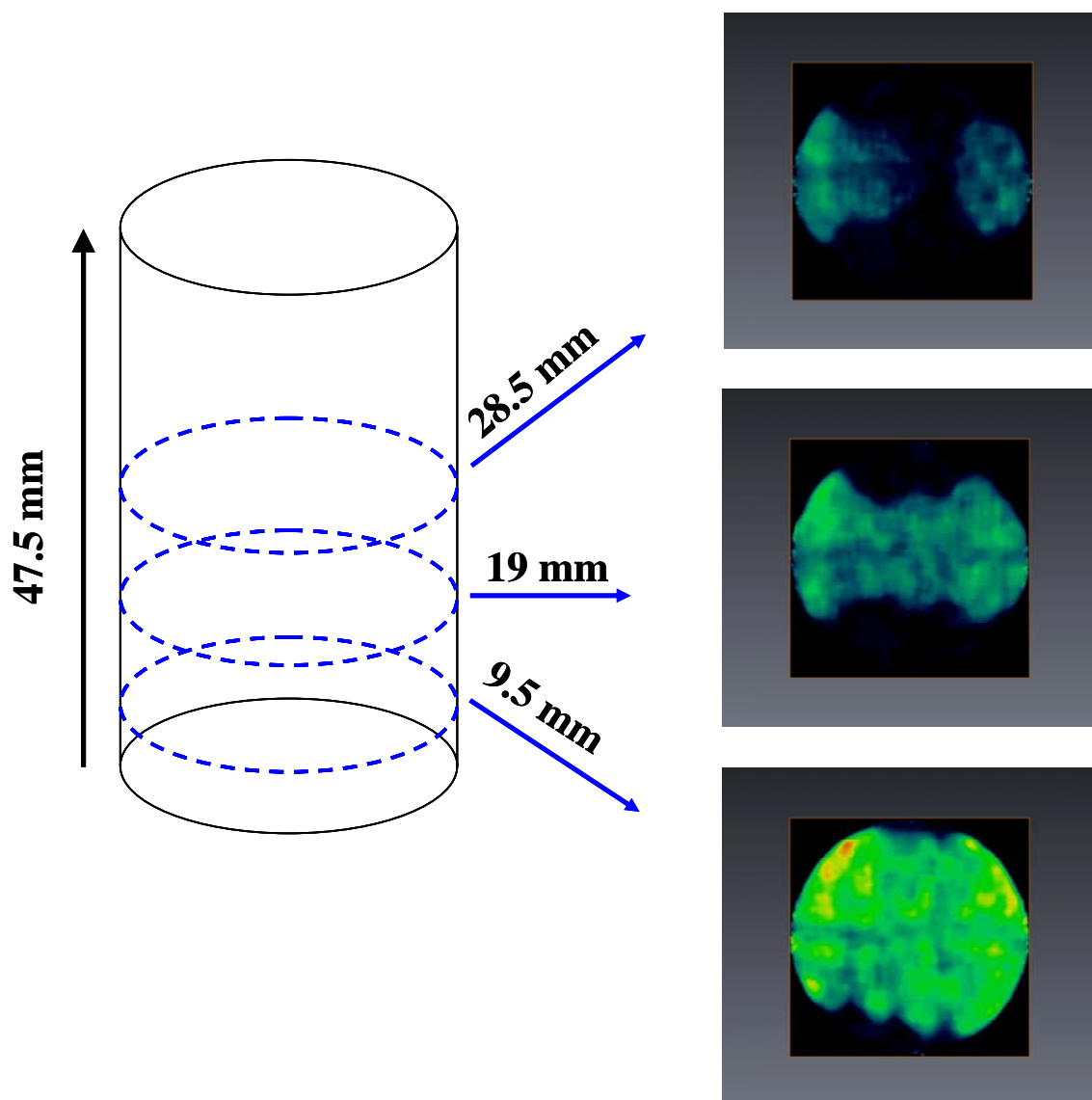


Figure 2-7: Water saturation distributions at 1072 min

Chapter 3

Methodology

The present study focuses on the development and implementation of a numerical model of spontaneous imbibition in fractured rocks showing contrasting rock properties in the form of bedding planes. A commercial reservoir simulator coupled with an automated history matching technique is utilized to construct relative permeability and capillary pressure curves. Parameters describing the relative permeability and capillary pressure curves were determined through an optimization method in order to identify the basic traits of multiphase flow in naturally fractured reservoirs. Saturation distributions from a 2-phase flow experiment in a fractured Berea sample using X-ray Computed Tomography (CT) were used for the validation of the numerical model. The proposed methodology was tested with four different synthetic and a semi-synthetic data sets. The first synthetic data set was prepared for the estimation of absolute permeability. The remaining three synthetic data sets were designed for the determination of relative permeability to oil using three different parameterizations. Detail explanations for the preparation of those synthetic and semi-synthetic data sets will be presented in Chapter 4. After testing the developed methodology with synthetic cases, a more complex semi-synthetic case was prepared using experimental spontaneous imbibition data of a fractured core sample in order to determine relative permeability for the matrix and capillary pressure for both matrix and the fracture simultaneously. Unlike the earlier synthetic cases, heterogeneous porosity and permeability distributions were implemented

in preparation of the numerical model. Absolute permeability and parameters controlling the relative permeability and capillary pressure curves were optimized successfully in those five cases using the proposed optimization algorithm.

3.1 Preparation of Representative Simulation Model

In this section, a sample preparation of simulation data for the semi-synthetic case, in which a fractured, heterogeneous Berea sandstone core sample was used, is presented to better describe the developed methodology. A preparation of the model for history matching consists of four parts such as fracture identification, subtraction, up-scaling and petrophysics. First of all, CT scan data of spontaneous imbibition experiment were uploaded into MATLAB[®] R2006b and rearranged in order to be used for the determination of porosity and permeability distribution. X-ray CT numbers are strong indicators of the density of the material scanned, which can be linked to porosity and consequently to permeability through correlations. High CT numbers indicate high density, low porosity, and low CT numbers represent higher porosity values. Fracture blocks were identified using a dry core sample by assigning a constant value for those blocks whose CT numbers were less than or equal to the threshold value of CT numbers, representative of the crack. The threshold value for CT numbers was determined as 2800 illustrated in Fig. 3-1. This figure represents the CT numbers along the potential fracture dimension. The same fracture definition was also used for the wet core sample.

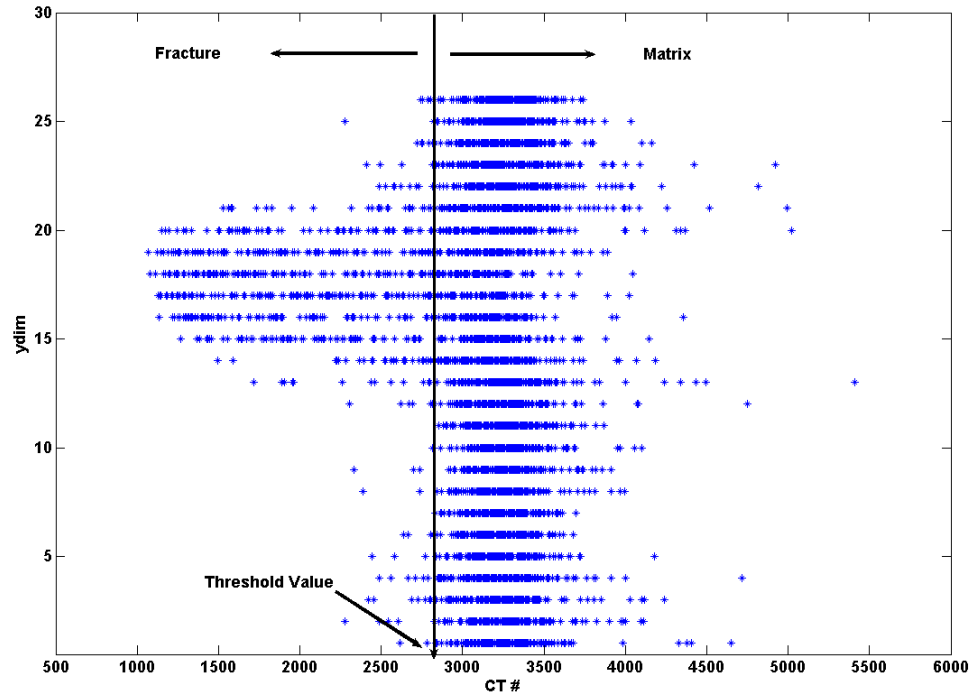


Figure 3-1: Determination of Threshold Value for CT Numbers

After the determination of fracture, the dry core sample was subtracted from the wet core sample in order to identify potential porous grid blocks. For up-scaling purposes, the subtracted data was up-scaled by a factor of 5 in each direction (x, y, z) using an arithmetic average of subtracted CT numbers. A successful up-scaling scheme was necessary for the purpose of simulation and optimization since the subtracted data has large number of grid blocks ($210 * 210 * 1440$) to simulate. An up-scaling factor of 5 was determined after implementing three different up-scaling schemes in the model construction. A schematic description of those up-scaling schemes is presented in Fig. 3-2. Detail comparison of those up-scaling schemes will be presented in chapter 5.1.

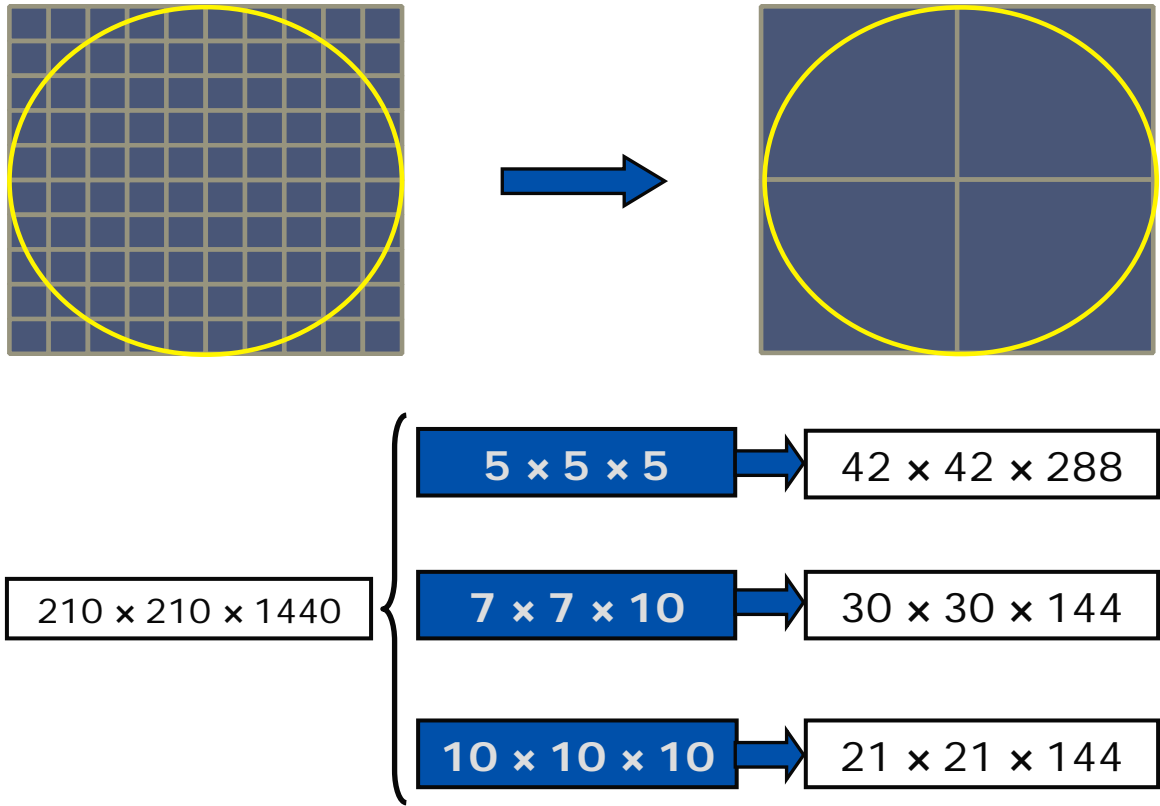


Figure 3-2: A Schematic Description of Up-scaling Schemes

The resulting up-scaled CT data were substituted into the following Eq. 3.1 to calculate the porosity for each volume of element.

$$\phi_{\text{voxel}} = \phi_{\text{avg}} * \frac{CT_{\text{wet}} - CT_{\text{dry}}}{(CT_{\text{wet}} - CT_{\text{dry}})_{\text{avg}}} \quad 3.1$$

where ϕ_{avg} , 18 %, is the average porosity of the core (Karpyn *et al.*, 2008); CT_{dry} and CT_{wet} are the CT numbers when the core is placed under vacuum and is saturated with a fluid respectively.

After obtaining the porosity distribution, Timur's correlation (1968), given by Eq. 3.2 was used to determine the permeability distribution with an average absolute permeability of 100 mD, as referenced in the experimental work (Karpyn *et al.*, 2008). Timur's correlation was also used by Alajmi (2003) for similar purposes, after testing several porosity-permeability correlations.

$$k = 0.136 \frac{\phi^{4.4}}{S_{wirr}^2} \quad 3.2$$

where ϕ is the porosity of the core (percentage) and S_{wirr} is the irreducible water saturation (fraction). In semi-synthetic case, irreducible water saturation of 0.227 satisfying the average permeability of 100 mD was used in the implementation of Eq. 3.2.

Finally, the resulting porosity and permeability distribution was incorporated in the simulation input file to be used for the developed history matching approach.

3.2 History Matching

History matching is a technique used for adjusting reservoir parameters such as absolute permeability, porosity, relative permeability and capillary pressure in coordination with the numerical simulator in order to achieve better match of reservoir performance with the observed data, prior to establishing predictive scenarios. A powerful optimization protocol should be utilized to minimize the least-square objective function. In this study, a sequential saturation distributions determined by a CT scanner is

compared with the predicted saturation values by adapting the relative permeability and capillary pressure. The black oil module (IMEX) of a commercial reservoir simulator, CMG (Computer Modeling Group, 2005) was used as the forward model coupled with the Optimization Toolbox of MATLAB[®] R2006b (The Math Works, 2006) to predict the absolute permeability, the relative permeability and the capillary pressure. A schematic diagram of automated history matching approach is illustrated in Fig. **3-3**. Initialization, simulation, convergence, and optimization are the four components of the automated history matching process. Rock and fluid properties such as relative permeability, capillary pressure, porosity and absolute permeability are the input parameters prepared in the initialization part in order to run the simulation. Saturation profiles were extracted from the simulator output and compared with the experimental data. Absolute permeability and oil relative permeability values were modified with a large-scale optimization algorithm (Trust-Region Method) until a match is achieved between the predicted and experimental saturation distributions within a pre-specified tolerance range.

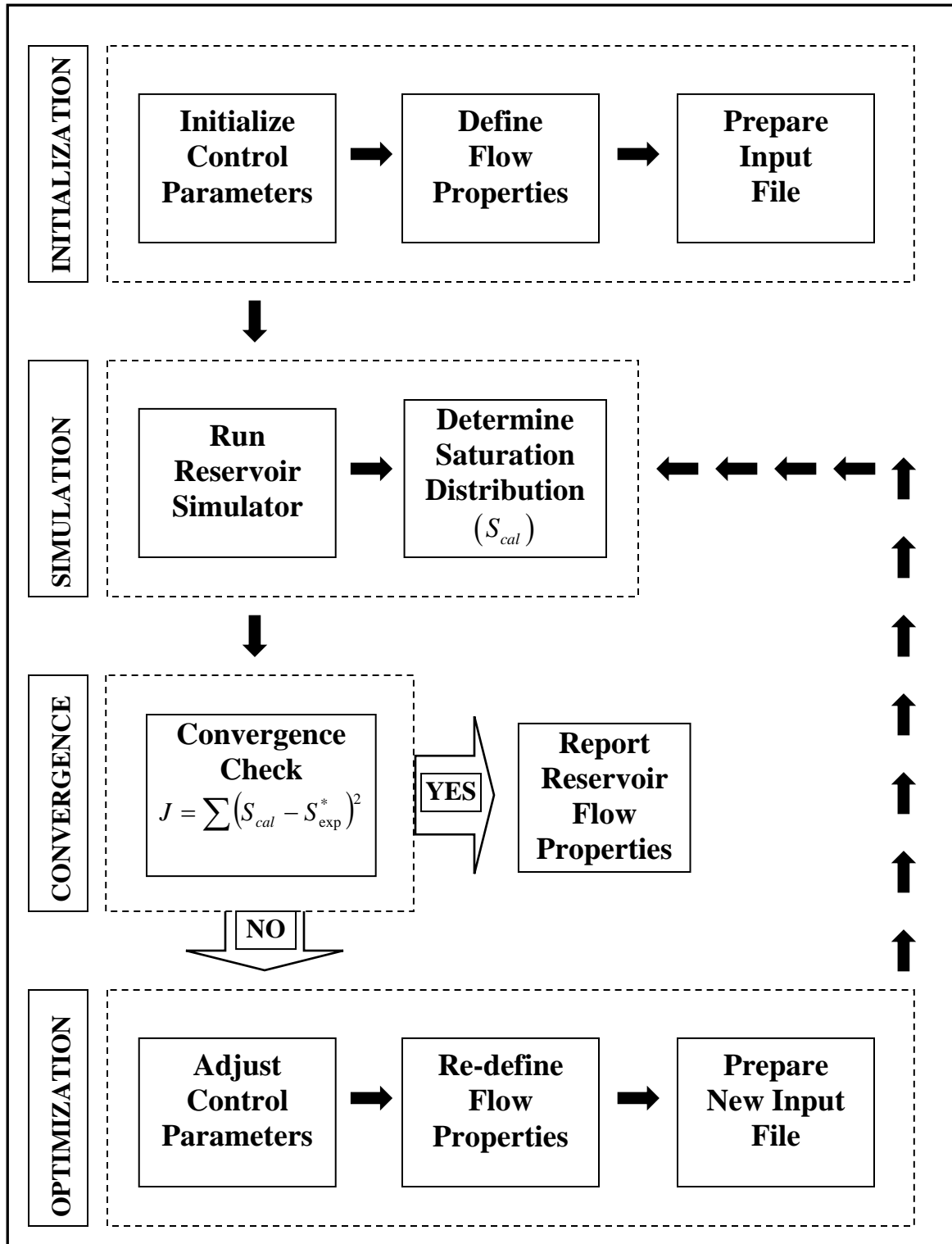


Figure 3-3: Schematic diagram of history matching approach (S_{exp}^* : Experimental Saturation Distribution from X-ray CT imaging)

MATLAB[®] codes **(B.1-6)** were developed with the optimization algorithm and coupled with the commercial reservoir simulator. An additional C++ programming **(B.7)** was used for the extraction of saturation data from the simulator output files. In the implementation of the optimization algorithm, the following objective function expressed by Eq. **3.3** is proposed to be minimized for the verification of match between experimental and predicted data.

$$J = \sum_{\Omega(x,y,z,t)} (S_{x,y,z,t}^{cal}(k_r, P_c) - S_{x,y,z,t}^{exp})^2 \quad \mathbf{3.3}$$

where $S_{x,y,z,t}^{cal}$ and $S_{x,y,z,t}^{exp}$ is the calculated and experimental saturation distribution in the core sample respectively. These saturations are a function of relative permeability, k_r and capillary pressure, P_c which are automatically adjusted to minimize the objective function; J until the convergence criteria is reached.

Different relative permeability definitions are available in the literature. The most widely used representation of the relative permeability is the power law model (Li, 2003) which is expressed by Eq. **3.4**:

$$k_{ri} = a_i (S_i - S_{ir})^{bi} \quad \mathbf{3.4}$$

where S_i is the saturation of phase i and S_{ir} is the residual saturation of phase i, a_i and b_i are the adjustable parameters in order to obtain a better match between predicted and observed relative permeability.

Capillary pressure is defined by the following Eq. 3.5 (Al-Wadahi *et al.*, 2000):

$$P_c = a_{pc}(P_c^* + b_{pc}) \quad 3.5$$

where P_c^* is a function of final fluid saturation distribution obtained from experiments, a_{pc} and b_{pc} are the parameters to be modified.

B-spline functions can also be used for the representation of relative permeability and capillary pressure curves. The B-spline curve is an approximating curve which is based on control points (Salomon, 1999). Knots have to be specified in addition to the control points to offer additional control on the B-spline curve. There are several types of B-splines. The knot values are uniformly distributed and all the weight functions have the same shape and are shifted with respect to each other in the uniform B-Spline. The non-uniform B-spline has user specified knots and the weight functions are changing in this type of splines. Other B-splines can be classified as open-uniform, rational, and non-rational. Detail description of these B-splines can be obtained from the study of Salomon (1999).

In this study, quadratic non-uniform and cubic uniform B-spline representations with no additional knot definitions were used to construct the relative permeability. The cubic uniform B-spline was additionally used since efficient computational algorithms

are achieved using uniform control points within the interval of interest (Salomon, 1999).

The quadratic and the cubic B-spline approximations for relative permeability curve are given by Eq. 3.6, Eq. 3.7 and Eq. 3.8, Eq. 3.9 respectively:

- **Quadratic B-spline Parameterization**

$$S_{wi}(t) = \frac{1}{2}(t^2 - 2t + 1)CS_w(i-1) + \frac{1}{2}(-2t^2 + 2t + 1)CS_w(i) + \frac{1}{2}(t^2)CS_w(i+1) \quad 3.6$$

$$kr_i(t) = \frac{1}{2}(t^2 - 2t + 1)Ckr(i-1) + \frac{1}{2}(-2t^2 + 2t + 1)Ckr(i) + \frac{1}{2}(t^2)Ckr(i+1) \quad 3.7$$

- **Cubic B-spline Parameterization**

$$S_{wi}(t) = \frac{1}{6}(-t^3 + 3t^2 - 3t + 1)CS_w(i-1) + \frac{1}{6}(3t^3 - 6t^2 + 4)CS_w(i) + \frac{1}{6}(-3t^3 + 3t^2 + 3t + 1)CS_w(i+1) + \frac{1}{6}(t^3)CS_w(i+2) \quad 3.8$$

$$kr_i(t) = \frac{1}{6}(-t^3 + 3t^2 - 3t + 1)Ckr(i-1) + \frac{1}{6}(3t^3 - 6t^2 + 4)Ckr(i) + \frac{1}{6}(-3t^3 + 3t^2 + 3t + 1)Ckr(i+1) + \frac{1}{6}(t^3)Ckr(i+2) \quad 3.9$$

where t is the variable that varies along the curve, CS_w and Ckr are the x and y coordinates of i^{th} control point respectively.

3.3 Optimization Algorithm

An efficient optimization algorithm that minimizes the objective function is necessary in order to obtain a successful history match. In this study, a large-scale trust region method was used for the adjustment of parameters that control the relative permeability curve. This method is embedded within the Optimization Toolbox of MATLAB[®] R2006b software.

In this approach, the objective is to minimize $f(x)$ where the function takes vector arguments and return scalars (The Math Works, 2006). The algorithm starts with a point x in n -space and tries to improve x in the direction of a point with lower function value. The basic idea is to find a simpler function q that approximate f in a neighborhood N around the point x . This neighborhood is called the trust-region. A trial step s is computed by minimizing over N . The trust-region sub-problem is defined by Eq. 3.10:

$$\min_s \{q(s) \mid s \in N\} \quad 3.10$$

The current point is updated to be $x + s$ if $f(x + s) < f(x)$; otherwise the current point remains unchanged and trust-region, N is reduced in size and the trial step computation is repeated.

The way the approximation q is chosen and computed is very critical in defining the trust-region problem. Choosing an appropriate trust-region and modifying it properly are also important for the accuracy of solving the trust-region sub-problem. The first two terms of the Taylor approximation of f at x is used for the definition of quadratic

approximation q in the standard trust-region method (The Math Works, 2006). The neighborhood N is usually considered as spherical or ellipsoidal in shape. A typical mathematical description of trust-region sub-problem is then given by:

$$\min \left\{ \frac{1}{2} s^T H s + s^T g \quad \text{such that} \quad \|Ds\| \leq \Delta \right\} \quad \mathbf{3.11}$$

where g is the gradient of f at the current point x , H is the Hessian matrix (the symmetric matrix of second derivatives of f), D is a diagonal scaling matrix, Δ is a positive scalar, and $\|\cdot\|$ is the 2-norm of matrix. There are several algorithms for solving Eq. **3.11**. In such algorithms, a full eigensystem is computed and a Newton process applied to the secular Eq. **3.12**:

$$\frac{1}{\Delta} - \frac{1}{\|s\|} = 0 \quad \mathbf{3.12}$$

Such algorithms provide an accurate solution to Eq. **3.11**, but several factorizations of H are required. Therefore, for large-scale problems, a different approach is utilized. Based on Eq. **3.11**, numerous approximation and heuristic strategies have been suggested in the literature (The Math Works, 2006). The methodology that Optimization Toolbox follows is to limit the trust-region sub-problem to a 2-D subspace S (The Math Works, 2006). Preconditioned conjugate gradient process is used in determination of the two-dimensional subspace S . The toolbox assigns $S = \langle s_1, s_2 \rangle$,

where s_1 is in the direction of the gradient g ,

$$s_2 \begin{cases} \text{either approximate Newton direction, solution to } H.s_2 = -g \\ \text{or a direction of negative curvature, } s_2^T . H . s_2 < 0 \end{cases}$$

The idea behind the choice of S is to force global convergence and achieve fast local convergence. Therefore this algorithm can be summarized in four steps:

- 1.** Formulation of the two-dimensional trust-region sub-problem.
- 2.** Solving Eq. **3.11** to determine the trial step s .
- 3.** If $f(x + s) \leq f(x)$ then $x + s$.
- 4.** Adjust Δ .

Chapter 4

Implementation of Automated History Matching

The main purpose of this study is to construct a 3-D numerical model that mimics the flow mechanism observed in a previous spontaneous imbibition experiment in fractured Berea sandstone conducted by Karpyn *et al.* (2008). An automated history matching approach, coupled with a commercial reservoir simulator, is proposed in this study to determine the relative permeability and capillary pressure curves of a fractured core sample. An efficient optimization algorithm is implemented to adjust the parameters controlling these two sets of curves.

4.1 Synthetic Cases

Testing of the proposed history matching methodology was done through the determination of known values of absolute permeability and relative permeability to oil corresponding to synthetic cases of 2-phase flow in core samples. The reservoir characteristics and reservoir rock-fluid properties used for the preparation of synthetic cases are presented in Table 4-1. A 3-D view of the lab-scale reservoir model of synthetic cases is given in Fig. 4-1. Model geometry and reservoir characteristics used in synthetic cases are similar to the properties used in experimental spontaneous imbibition. The 3-D model of synthetic cases has dimensions of 19 cm, 12 cm, and 5 cm in x, y, and z directions respectively with a homogeneous permeability value of 500 mD. A half

cylinder representation of the core sample is used for the lab-scale model. The vertical plane of symmetry corresponds to the location of the fracture in the experimental reference. The total volume of injected water is 2.7 cc with a 30 min injection period.

Table 4-1: Reservoir Rock and Fluid properties

Core dimensions, cm in x, y, z direction	x = 1.9	y = 1.2	z = 5
Matrix permeability (mD) in x, y, z direction	500	500	500
Porosity (%)	25		
Pore compressibility (1/kPa)	5.9E-08		
Pore pressure (kPa)	240.5		
Oil density (g/cm³)	0.89		
Water density (g/cm³)	1.11		
Oil compressibility (1/kPa)	8.96311E-04		
Water compressibility (1/kPa)	0		
Bubble point pressure (kPa)	222.915		
Total volume of injected water (cc)	2.7		
Water injection time (min)	30		

Four different synthetic data sets were prepared to test the automated history match methodology. The first data set was designed for predicting the absolute permeability of the sample. The second data set was prepared for estimating the relative permeability to oil approximated by a power law representation. The quadratic and cubic B-spline representations of oil relative permeability were used for the last two cases, respectively.

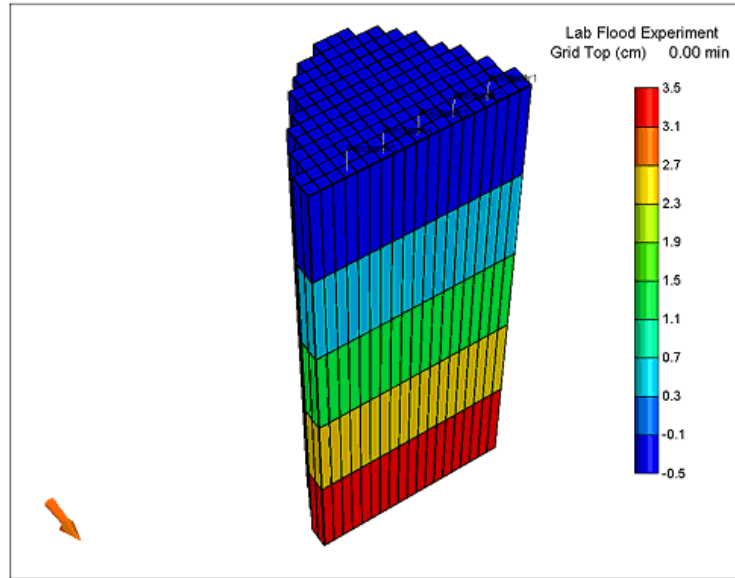


Figure 4-1: 3-D representation of the synthetic model showing depth of the centre of the block. Rectangular face corresponds to fracture plane.

4.1.1 Estimation of Absolute Permeability

The objective of this case is to determine the absolute permeability of the core sample using the proposed automated history matching method. This synthetic data set was prepared using an absolute permeability value of 500 mD and known reservoir rock-fluid properties given in Table 4-1. Starting with initial guess varying between 10 and 1000 mD, absolute permeability was optimized.

Preliminary modeling and optimization results demonstrate that optimization was successful for estimating the absolute permeability of reservoir. The objective function, J , which is defined as the square of the differences between calculated and the experimental saturation values, is plotted against absolute permeability values in Fig. 4-2. This figure indicates that J is decreasing by increase in absolute permeability up to a value of 500

mD where it vanishes and increasing when the absolute permeability is moving further from a value of 500 mD. It is observed from Fig. 4-2 that there is a minimum objective function value at 500 mD since the synthetic data set was prepared using an absolute permeability of 500 mD verifying that objective function was calculated correctly.

After the objective function calculation was proved, absolute permeability of the reservoir was optimized using the optimization algorithm mentioned in chapter 3.3. Table 4-2 illustrates the optimized absolute permeability values together with the proposed initial guesses recalling that 500 mD was the target value. Two stopping criteria conditions were defined for the optimization algorithm. The objective function and the target parameter tolerances are determined as 10^{-7} and 10^{-5} respectively. For all successive runs in synthetic cases, same stopping criteria conditions were prevailed.

It can be noticed from Table 4-2 that the estimated absolute permeability values converged to the target value even though the optimization algorithm was initiated with different guesses. This observation validates that a successful optimization protocol is attained for optimizing one parameter. Therefore, several different absolute permeability values were predicted starting from arbitrary initial guesses (Fig. 4-3 and Table 4-3).

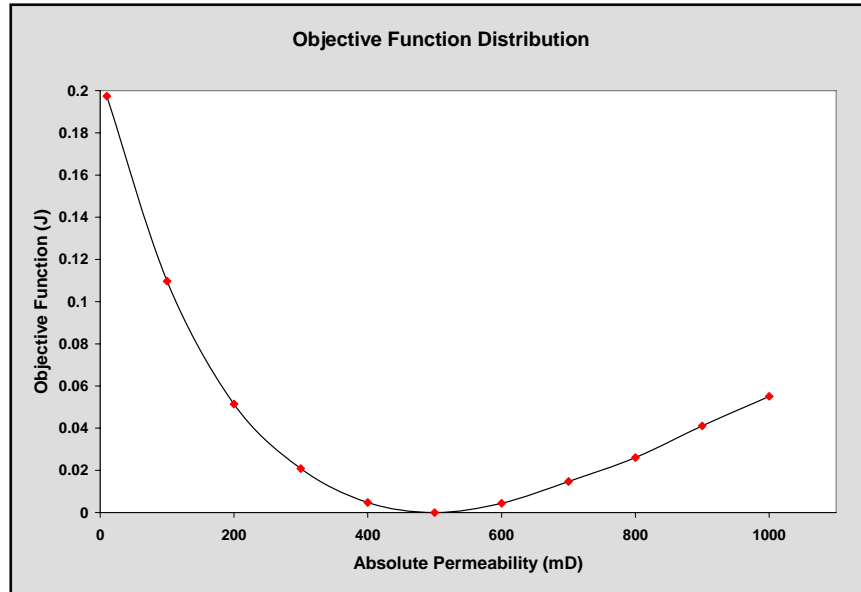


Figure 4-2: Minimization of objective function with respect to absolute permeability

Table 4-2: Initial Guesses and Estimated Absolute Permeability Values
(Target $k_{abs}=500$ mD)

Initial Guess for k_{abs}	Estimated k_{abs}
10	500.02057
100	500.02075
200	500.02055
300	500.01994
400	500.02005
600	500.02072
700	500.02201
800	500.02042
900	500.02016
1000	500.02231

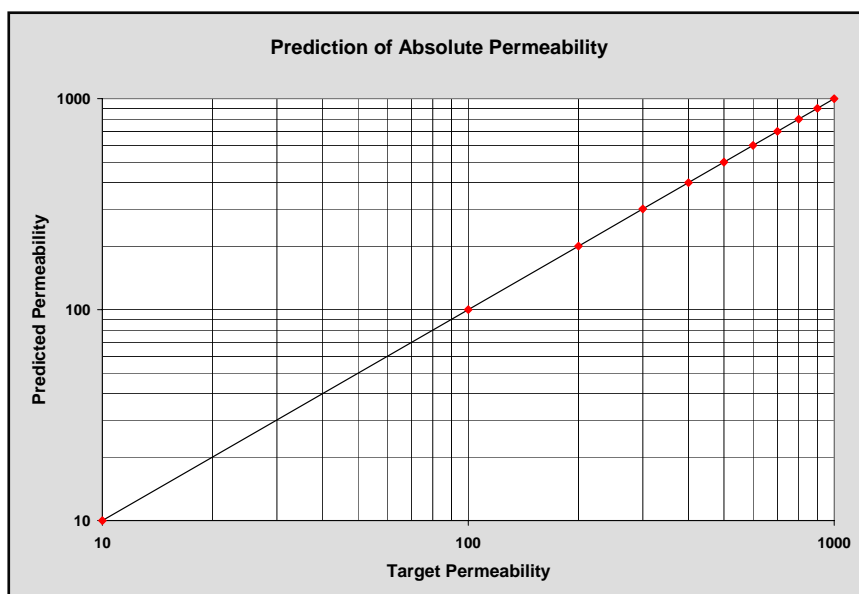


Figure 4-3: Absolute Permeability (k_{abs}) Predictions

Table 4-3: Absolute Permeability Predictions

Initial Guess	Estimated k_{abs}	Target k_{abs}
20	10.00360	10
300	99.99935	100
500	200.02647	200
100	300.03365	300
200	399.96204	400
300	500.01994	500
300	599.97696	600
900	700.00537	700
400	799.97230	800
400	900.09562	900
600	999.56139	1000

4.1.2 Estimation of Relative Permeability to Oil Using Power Law Parameterization

The goal of this second case is to obtain the oil relative permeability curve using a power law representation. Based on the standard power law parameterization, oil relative permeability is defined by Eq. 4.1:

$$kr_{ol} = a_1(1 - S_w - S_{or})^{b_1} \quad 4.1$$

After the adjustment of controlling parameters a_1 and b_1 with the aid of the values given by Li (2003), initial guesses and target values for those parameters were tabulated in Table 4-4 and plotted in Fig. 4-4. Those parameters were arbitrarily adjusted in a way that initial guesses of parameters for the oil relative permeability curve were quite different from the target.

Table 4-4: Initial and Target values for power-law parameterization

a_1		b_1	
Initial	Target	Initial	Target
0.8245	0.2546	1.7567	1.425

In the case where the oil relative permeability was optimized using a power law parameterization, the history matching process was terminated due to unreasonable oil relative permeability generations. It was found that the power law parameterization does not provide an appropriate relative permeability representation for automated history

matching. The resulting oil relative permeability values were not monotonically decreasing, since the coefficients were perturbed arbitrarily by the optimization algorithm. The reservoir simulator needs a monotonically decreasing relative permeability curve for oil. Therefore, B-spline parameterization with a transformation of variables was introduced to guarantee a monotonically decreasing relative permeability curve.

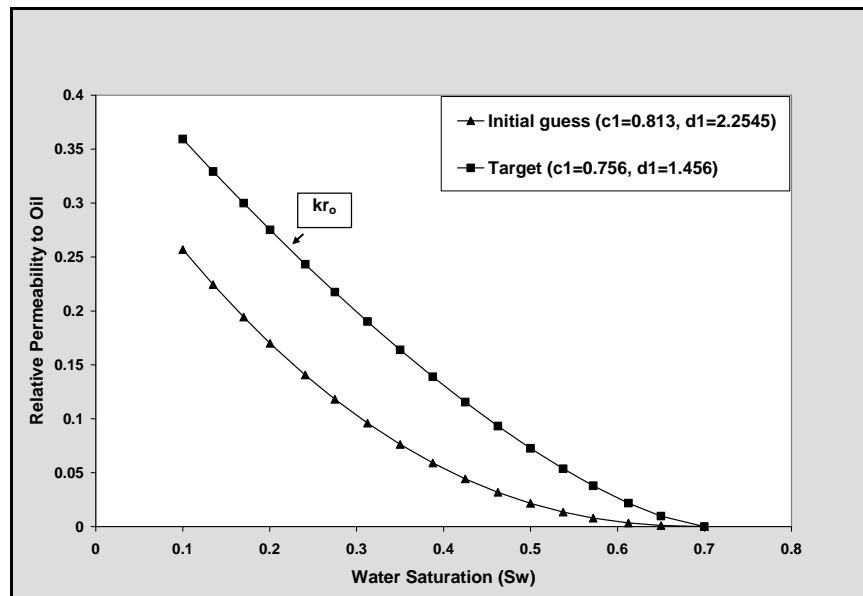


Figure 4-4: Relative permeability curves using power-law parameterization

4.1.3 Estimation of Relative Permeability to Oil Using Quadratic B-Spline Parameterization

The aim of this case is to determine oil relative permeability using quadratic B-splines. It was mainly concentrated on the representation of oil relative permeability in order to validate the optimization algorithm. Therefore, two control points (CS_{w1}, Ckr_{o1}) and (CS_{w2}, Ckr_{o2}) were chosen to generate the synthetic case using non-uniform quadratic B-spline parameterization for oil relative permeability. Those control points were selected according to the oil relative permeability curve presented in Chen *et al.* (2005) and tabulated in Table 4-5:

Table 4-5: Control Points for Quadratic B-spline Representation

CS_{w1}	Ckr_{o1}	CS_{w2}	Ckr_{o2}
0.3	0.3	0.6	0.06

The end-points, (CS_{w0}, Ckr_{o0}) and (CS_{w3}, Ckr_{o3}) , were also known from the definition of oil relative permeability and given in Table 4-6:

Table 4-6: End Control Points for Quadratic B-spline Representation

CS_{w0}	Ckr_{o0}	CS_{w3}	Ckr_{o3}
0	1	1	0

Two additional control points, (CS_{w-1}, Ckr_{o-1}) and (CS_{w4}, Ckr_{o4}) , have to be defined in order to use the quadratic representation given by Eq. **3-6**, Eq. **3-7**. Those control points should be chosen in such a way that B-spline curve passes through the two end points (CS_{w0}, Ckr_{o0}) and (CS_{w3}, Ckr_{o3}) . Therefore control points can be given in a matrix form as:

$$\begin{bmatrix} CS_{w-1} \\ CS_{w0} \\ CS_{w1} \\ CS_{w2} \\ CS_{w3} \\ CS_{w4} \end{bmatrix} = \begin{bmatrix} 0 \\ 0 \\ 0.3 \\ 0.6 \\ 1 \\ 1 \end{bmatrix} \quad \begin{bmatrix} Ckr_{o-1} \\ Ckr_{o0} \\ Ckr_{o1} \\ Ckr_{o2} \\ Ckr_{o3} \\ Ckr_{o4} \end{bmatrix} = \begin{bmatrix} 1 \\ 1 \\ 0.3 \\ 0.06 \\ 0 \\ 0 \end{bmatrix}$$

Using the definition given by Eq. **3-7**, the oil relative permeability curve is represented by equations in four different saturation intervals (**A.1**) and illustrated in Fig. **4-5**:

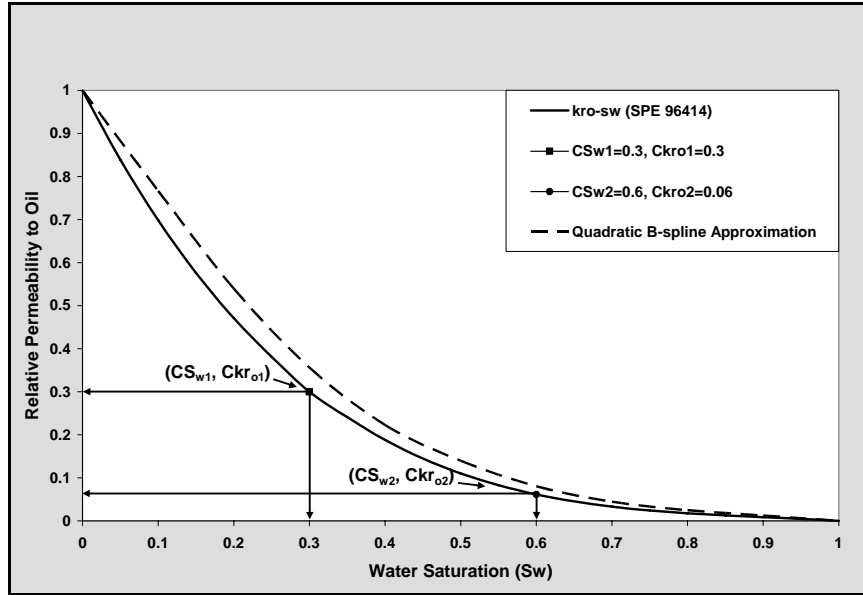


Figure 4-5: Relative permeability curves using quadratic B-spline parameterization

In the generation of relative permeability curves, it is very important that resulting relative permeability curves become monotonically decreasing for oil and increasing for water since the reservoir simulator (forward model) requires monotonicity for relative permeability definitions. Therefore, transformation of variables was introduced in order to guarantee the monotonicity of the relative permeability curves. The transformation procedure is similar to the one used by Chen *et al.* (2005). Since optimization was focused on oil relative permeability, the control points C_i^o were transformed to a new set of parameters, y_i which are defined by Eq. 4.2:

$$y_i = \ln \left(\frac{C_i^o - C_{i+1}^o}{C_{i-1}^o - C_i^o} \right) \quad \text{for } 1 \leq i \leq n \quad 4.2$$

where n is the number of intervals, $C_0^o = 1$ and $C_n^o = 0$,

$$\text{for cubic B-spline } \begin{cases} C_{-1}^o = 2C_0^o - C_1^o \\ C_{n+1}^o = 2C_n^o - C_{n-1}^o \end{cases}, \text{ for quadratic B-spline } \begin{cases} C_{-1}^o = C_0^o \\ C_{n+1}^o = C_n^o \end{cases}$$

Control points C_i^o were mapped to the variable y_i . The inverse transformation can be represented by the following Eq. 4.3 and Eq. 4.4:

$$e^{y_i} = \frac{C_i^o - C_{i+1}^o}{C_{i-1}^o - C_i^o} \quad \text{for } 1 \leq i \leq n-1 \quad 4.3$$

$$C_i^o = \frac{e^{y_i}}{1 + e^{y_i}} C_{i-1}^o + \frac{1}{1 + e^{y_i}} C_{i+1}^o \quad \text{for } 1 \leq i \leq n-1 \quad 4.4$$

where $C_0^o = 1$ and $C_n^o = 0$

After the parameterization using quadratic B-spline, the objective function distribution was obtained as a function of two control points Ckr_{o1} and Ckr_{o2} at given water saturations, $CS_{w1} = 0.3$ and $CS_{w2} = 0.6$, respectively:

Table 4-7 is prepared for the range of 0.1 and 0.7 for Ckr_{o1} whereas Ckr_{o2} varies between 0.05 and 0.4. The maximum attainable values for Ckr_{o1} and Ckr_{o2} are determined as 0.7 and 0.4 respectively since the straight line oil relative permeability gives the oil relative permeability of 0.7 at $CS_{w1} = 0.3$ and 0.4 at $CS_{w2} = 0.6$. The

minimum value for both control points is obviously zero. But, the first control point, Ckr_{o1} , has to be greater than the second control point, Ckr_{o2} , since the monotonicity requirement is satisfied if only this condition prevails. The objective function values designated by “NaN” result from the aforementioned requirement. The zero objective function value highlighted with a red color is obtained at $Ckr_{o1} = 0.3$ and $Ckr_{o2} = 0.06$ and corresponds with the optimized solution leading to the correct combination of CS_{w1} and CS_{w2} for this synthetic case. The objective function calculations were accurate for the case where non-uniform quadratic B-spline was introduced for the representation of oil relative permeability curve. It can be observed from Table 4-7 that the objective function value decreases until the control points of synthetic data are reached and increases when both control points Ckr_{o1} and Ckr_{o2} rise after that point.

Table 4-7: Objective Function Distribution for Quadratic B-spline Parameterization

The Objective Function Distribution								
C1\C2	0.06	0.1	0.15	0.2	0.25	0.3	0.35	0.4
0.1	1.6488	NaN	NaN	NaN	NaN	NaN	NaN	NaN
0.15	0.6884	0.3527	NaN	NaN	NaN	NaN	NaN	NaN
0.2	0.2405	0.6991	4.342	NaN	NaN	NaN	NaN	NaN
0.25	0.0487	1.0712	5.0292	10.2493	NaN	NaN	NaN	NaN
0.3	0	1.4414	5.6367	10.9483	16.4693	NaN	NaN	NaN
0.35	0.0343	1.7982	6.1811	11.5638	17.088	21.656	NaN	NaN
0.4	0.118	2.1376	6.6736	12.1145	17.638	22.0387	25.1645	NaN
0.45	0.2317	2.4571	7.121	12.6082	18.1011	22.3686	25.4021	26.1089
0.5	0.3631	2.7573	7.5288	13.0559	18.5143	22.6591	25.441	26.1651
0.55	0.5042	3.0379	7.9046	13.4648	18.8754	22.916	25.4994	26.2166
0.6	0.6496	3.3011	8.252	13.8395	19.2001	23.1454	25.5509	26.2617
0.65	0.7953	3.5485	8.5739	14.1886	19.4934	23.353	25.6007	26.303
0.7	0.939	3.7819	8.8745	14.509	19.7584	23.541	25.6493	26.3412

After the verification of the objective function calculation, optimization was performed in terms of the transformed variable y_i . The unknown control points were calculated using the inverse transformation given in Eq. 4.3 and Eq. 4.4. Transformed variables and the corresponding control points are tabulated in Table 4-8. It can be perceived from this table that the two transformed variables y_1 and y_2 were optimized successfully. Therefore the resulting oil relative permeability curve is presented in Fig. 4-6, where straight line oil relative permeability curve was used as an initial guess. The estimated oil relative permeability values were matched with the target values by using the quadratic B-spline representation.

Table 4-8: Estimated transformed variables and control points

	Initial	Target	Estimated
y_1	0	-1.0704	-1.0706
y_2	0	-1.3863	-1.3863
Ckr_{o1}	0.4	0.3	0.3
Ckr_{o2}	0.7	0.06	0.06

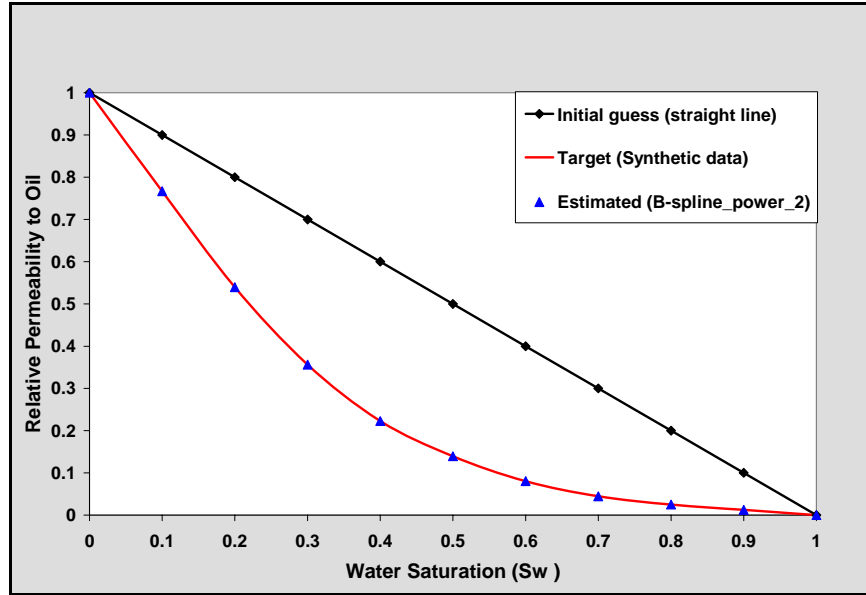


Figure 4-6: Relative permeability vs water saturation plot using quadratic B-spline parameterization

4.1.4 Estimation of Relative Permeability to Oil Using Cubic B-Spline

Determination of relative permeability to oil using cubic B-spline is the goal of this case. Cubic B-spline representation was additionally used since efficient computational algorithms are achieved using uniform control points. Therefore, three uniformly spaced control points, (CS_{w1}, Ckr_{o1}) , (CS_{w2}, Ckr_{o2}) , (CS_{w3}, Ckr_{o3}) , were determined to construct oil relative permeability given in Table 4-9:

Table 4-9: Control Points for Cubic B-spline Representation

CS_{w1}	Ckr_{o1}	CS_{w2}	Ckr_{o2}	CS_{w3}	Ckr_{o3}
0.25	0.3811	0.5	0.1102	0.75	0.0241

The end-points (CS_{w0}, Ckr_{o0}) and (CS_{w4}, Ckr_{o4}) were determined from the definition of oil relative permeability and given in Table **4-10**:

Table **4-10**: End Control Points for Cubic B-spline Representation

CS_{w0}	Ckr_{o0}	CS_{w4}	Ckr_{o4}
0	1	1	0

Two additional control points (CS_{w-1}, Ckr_{o-1}) and (CS_{w5}, Ckr_{o5}) given in Table **4-11** that guarantees B-spline passes through the end-points were obtained by Eq. **4.5**:

$$\begin{aligned} C_{-1} &= 2C_0 - C_1 \\ C_5 &= 2C_4 - C_3 \end{aligned} \quad \mathbf{4.5}$$

Table **4-11**: Imaginary Control Points for Cubic B-spline Representation

CS_{w-1}	Ckr_{o-1}	CS_{w5}	Ckr_{o5}
-0.25	1.6189	1.25	-0.0241

Therefore, those control points for cubic B-spline parameterization are given in the matrix form as:

$$\begin{bmatrix} CS_{w-1} \\ CS_{w0} \\ CS_{w1} \\ CS_{w2} \\ CS_{w3} \\ CS_{w4} \\ CS_{w5} \end{bmatrix} = \begin{bmatrix} -0.25 \\ 0 \\ 0.25 \\ 0.5 \\ 0.75 \\ 1 \\ 1.25 \end{bmatrix} \quad \begin{bmatrix} Ckr_{o-1} \\ Ckr_{o0} \\ Ckr_{o1} \\ Ckr_{o2} \\ Ckr_{o3} \\ Ckr_{o4} \\ Ckr_{o5} \end{bmatrix} = \begin{bmatrix} 1.6189 \\ 1 \\ 0.3811 \\ 0.1102 \\ 0.0241 \\ 0 \\ -0.0241 \end{bmatrix}$$

Using the definition given by Eq. 3-8, Eq. 3-9, oil relative permeability curve is represented by equations in four different saturation intervals (A.2) and given in Fig. 4-7.

Uniform cubic spline parameterization with the transformation of variables was used in order to construct the oil relative permeability curve. Uniform cubic B-spline was preferred since efficient computational algorithms are achieved using equally spaced control points (Chen *et al.*, 2005). The generated oil relative permeability is still monotonically decreasing since transformation of variables is utilized. Estimated transformed variables and control points were given in Table 4-12. It can be observed from this table that estimated transformed variables and corresponding control points are very close to the target values by initially guessed with straight line oil relative permeability curve. Resulting oil relative permeability curve is presented in Fig. 4-8.

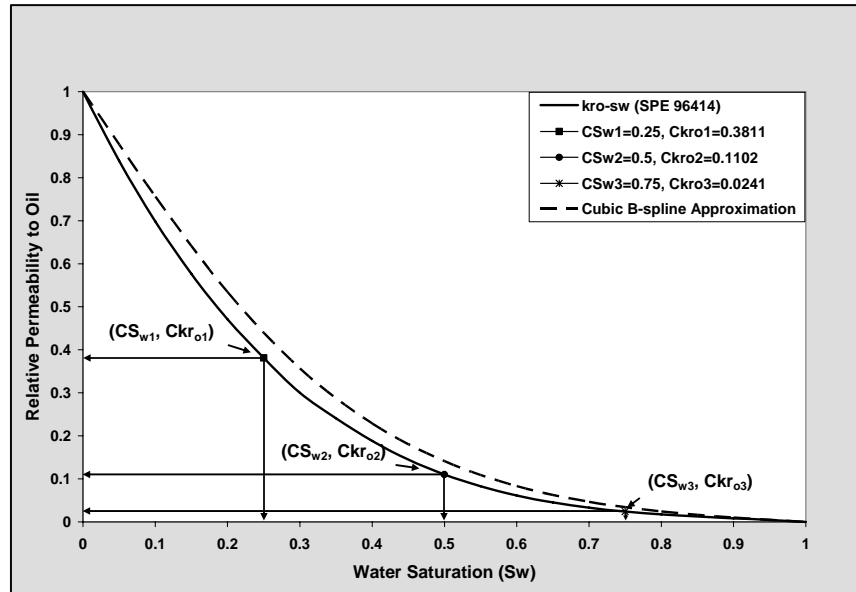


Figure 4-7: Relative permeability curves using cubic B-spline parameterization

Table 4-12: Estimated transformed variables and control points

	Initial	Target	Estimated
y_1	0	-0.82619	-0.7821
y_2	0	-1.14624	-1.1848
y_3	0	-1.27329	-1.2663
Ckr_{o1}	0.25	0.3811	0.389
Ckr_{o2}	0.5	0.1102	0.1096
Ckr_{o3}	0.75	0.0241	0.0241

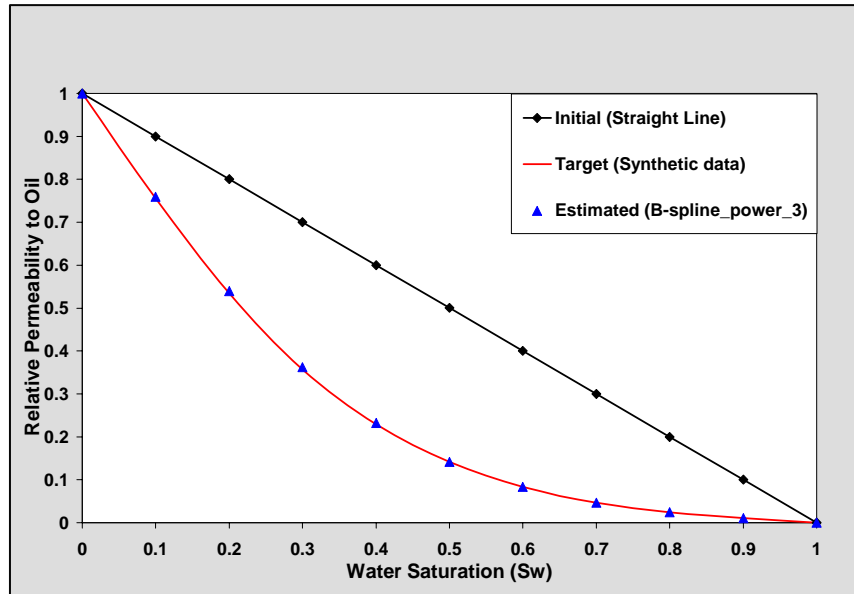


Figure 4-8: Relative permeability vs water saturation plot using cubic B-spline parameterization

4.2 Semi-Synthetic Case

The developed history matching methodology was validated by determining known values of oil-water relative permeability for matrix and capillary pressure for both matrix and fracture, corresponding to a semi-synthetic case of 2-phase flow in a fractured, heterogeneous core sample. It is called semi-synthetic because actual experimental CT scan data were used to define the distribution of porosity and consequently permeability, while other known dynamic properties such as relative permeability and capillary pressure were recalculated using the methodology described in chapter 3.1. The reservoir characteristics and reservoir rock-fluid properties used in the preparation of semi-synthetic case are presented in Table 4-13. A representative areal

porosity and permeability distributions are given in Fig. 4-9 and Fig. 4-10. A 3-D view of the lab-scale reservoir model of semi-synthetic case is given in Fig. 4-11. The 3-D model of semi-synthetic case has dimensions of 2.54 cm, 2.54 cm and 4.75 cm in x, y, and z direction respectively with an average porosity value of 18 % and an average permeability of 100 mD. The volume of injected water was 0.25 cc with a 4 min injection period, which was similar to the properties used in experimental spontaneous imbibition.

Table 4-13: Reservoir Rock and Fluid Properties (Semi-Synthetic Case)

Core dimensions, cm in x, y, z direction	x = 2.54	y = 2.54	z = 4.75
Average matrix permeability (mD)	100		
Average matrix porosity (%)	18		
Pore compressibility (1/kPa)	5.9E-08		
Pore pressure (kPa)	240.5		
Oil density (g/cm³)	0.89		
Water density (g/cm³)	1.11		
Oil compressibility (1/kPa)	8.96311E-04		
Water compressibility (1/kPa)	0		
Bubble point pressure (kPa)	222.915		
Total volume of injected water (cc)	0.25		
Water injection time (min)	4		

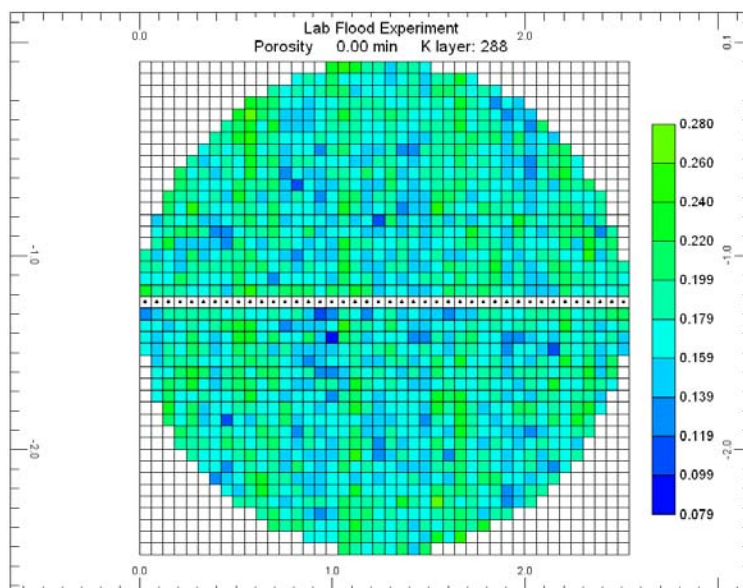


Figure 4-9: Representative areal porosity distribution, fraction

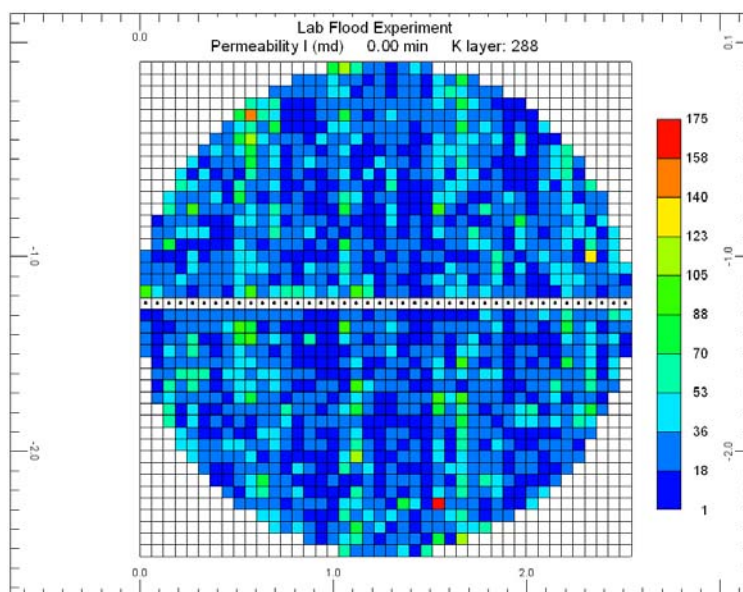


Figure 4-10: Representative areal permeability distribution, mD

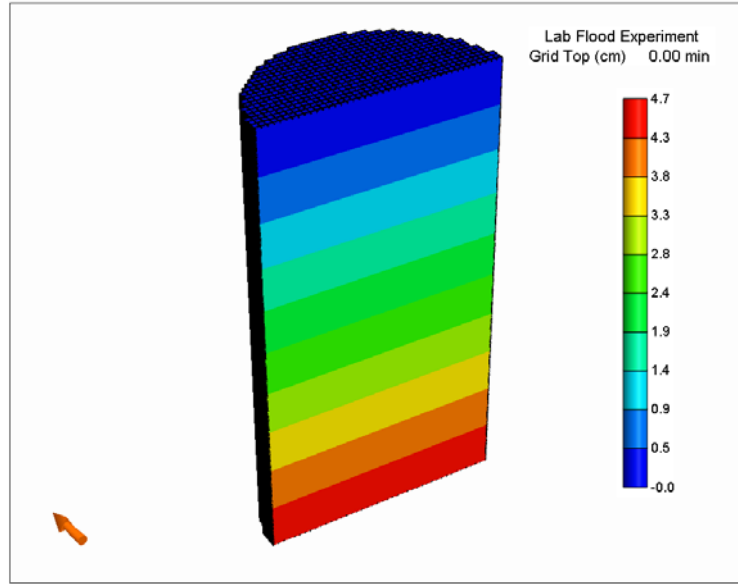


Figure 4-11: 3-D representation of the semi-synthetic model showing depth of the centre of the block

4.2.1 Determination of Oil-Water Relative Permeability and Capillary Pressure

Oil-water relative permeabilities for matrix and capillary pressure for both matrix and fracture were determined simultaneously in this case. Three uniformly spaced control points (CS_{w1}, Ckr_{o1}) , (CS_{w2}, Ckr_{o2}) , (CS_{w3}, Ckr_{o3}) and four uniformly spaced control points (CS_{w1}, Ckr_{w1}) , (CS_{w2}, Ckr_{w2}) , (CS_{w3}, Ckr_{w3}) , (CS_{w4}, Ckr_{w4}) were determined to construct oil and water relative permeability respectively. For capillary pressure, CP_c and CP_{cf} were used to construct capillary pressure curves in the matrix and fracture, following Eq. 4.6 (Brooks and Corey, 1964).

$$P_c = \frac{C}{(S_e)^{0.5}}$$

$$S_e = \frac{S_w - S_{wirr}}{1 - S_{or} - S_{wirr}}$$

4.6

After optimizing those nine parameters simultaneously, the following relative permeability and capillary pressure curves were obtained (Fig. 4-12, Fig. 4-13 and Fig. 4-14).

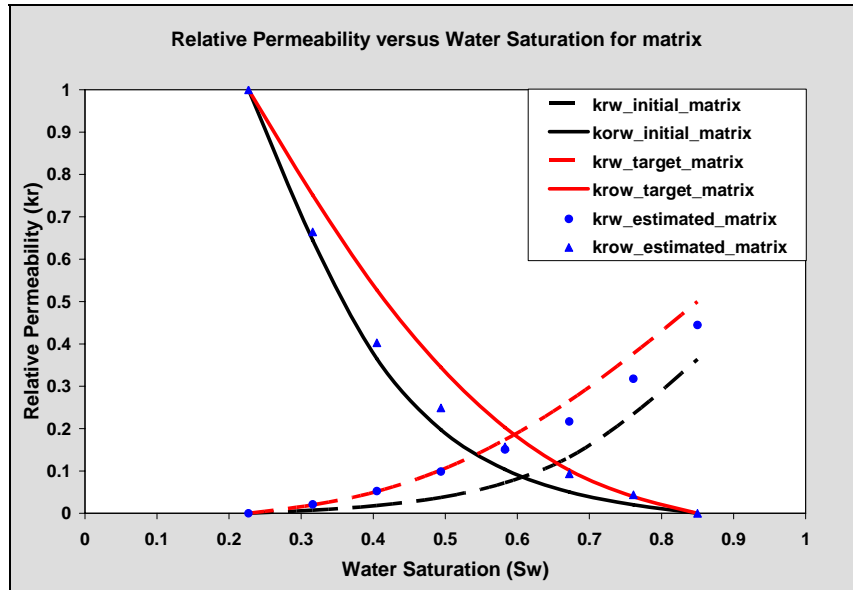


Figure 4-12: Relative permeability vs. water saturation plot for matrix and fracture

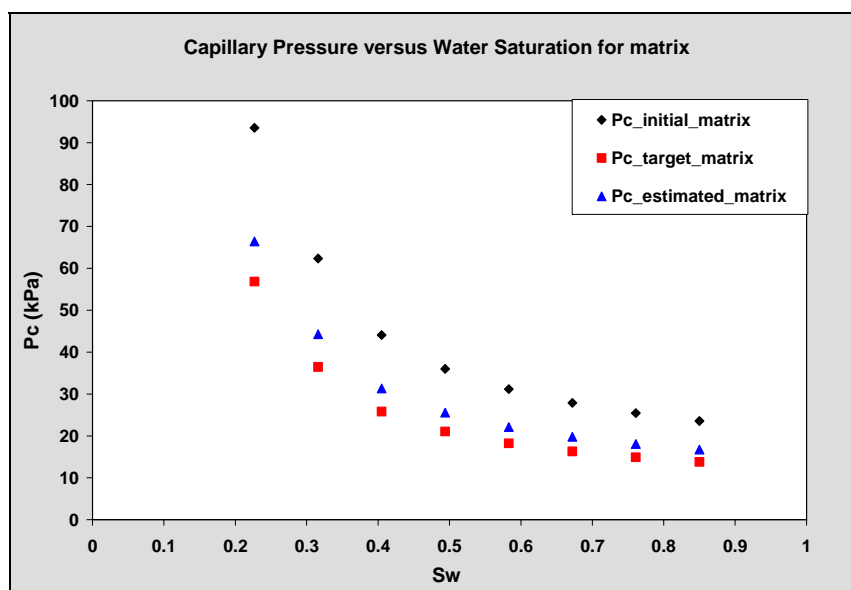


Figure 4-13: Capillary pressure vs. water saturation plot for matrix

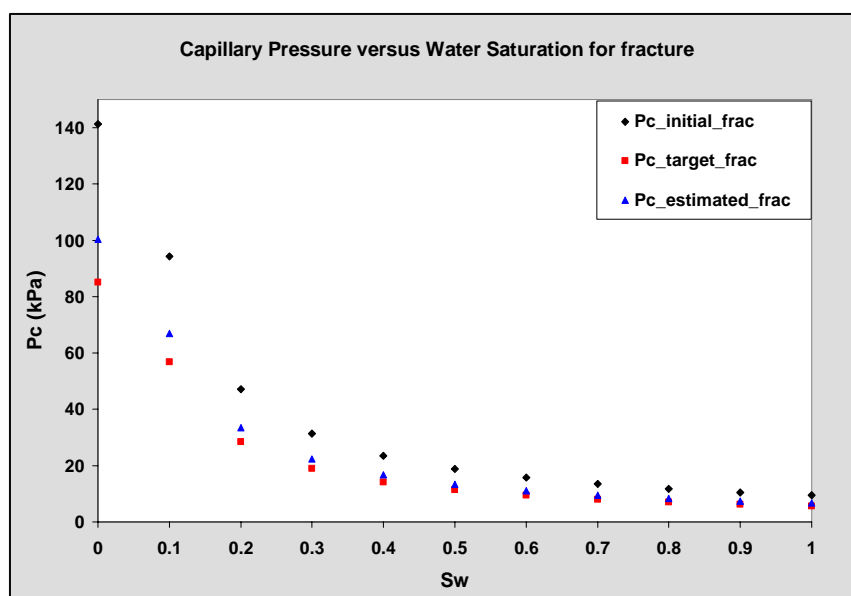


Figure 4-14: Capillary pressure vs. water saturation plot for fracture

It can be perceived from Fig. 4-12, Fig. 4-13 and Fig. 4-14 that relative permeability and capillary pressure curves are successfully determined simultaneously although some discrepancies were observed between the target and the estimated values for specific ranges of water saturation. This may be attributed to the selection of irreducible water saturation as well as the observation of unaltered water saturation distribution between the iterations. Since this case is semi-synthetic, irreducible water saturation was selected as 22.7 % for the matrix, which satisfies the condition of having average permeability of 100 mD obtained from experimental observations. Therefore, the optimization algorithm could not capture saturation changes below this value which leads to mismatch of relative permeability and capillary pressure values for some specific water saturation ranges. However, the proposed algorithm can handle the optimization of multiple parameters used for the construction of relative permeability and capillary pressure curves for most of the saturation values.

In addition, simultaneous optimization results are given in Fig. 4-15, in which the current value of nine variables controlling relative permeability and capillary pressure curves (Fig. 4-15.a), current objective function values (Fig. 4-15.b), step size (Fig. 4-15.c), total objective function evaluations (Fig. 4-15.d), norm of residuals (Fig. 4-15.e), and first-order optimality (Fig. 4-15.f) were presented as a function of iteration. The first three variables in Fig. 4-15.a represent the current value alteration of parameters controlling the oil relative permeability curve whereas variables from 4 to 7 illustrate the change in controlling parameters used in the construction of relative permeability to water curve. Furthermore, capillary pressure curves for the matrix and the fracture were controlled by the last two variables respectively. It is observed from Fig. 4-15.a that five

of the variables (number 2, 4, 7, 8 and 9) were optimized better than the rest of the variables, since corresponding estimated values were close to the target values for those five variables. This observation verifies that capillary forces in the matrix and in the fracture controlled by variables 8 and 9 are the most dominant driving mechanisms affecting the saturation changes in spontaneous capillary imbibition process compared to relative permeabilities. Therefore, the optimization of variables 8 and 9 as well as the optimized relative permeability curves for some specific saturation intervals would be sufficient for obtaining the target saturation distribution, which is also consistent with the tendency of norm of residuals in Fig. **4-15.e**. According to this figure, norm of residuals are quickly approaching zero and stay constant after the fourth iteration, which validates the existence of unaltered saturation values between the two successive iteration. This observation also implies that the change in relative permeability and capillary pressure controlled by nine parameters are not affecting the saturation distribution after the fourth iterations, which also leads to those discrepancies observed in Fig. **4-12**, Fig. **4-13** and Fig. **4-14** for some water saturation intervals.

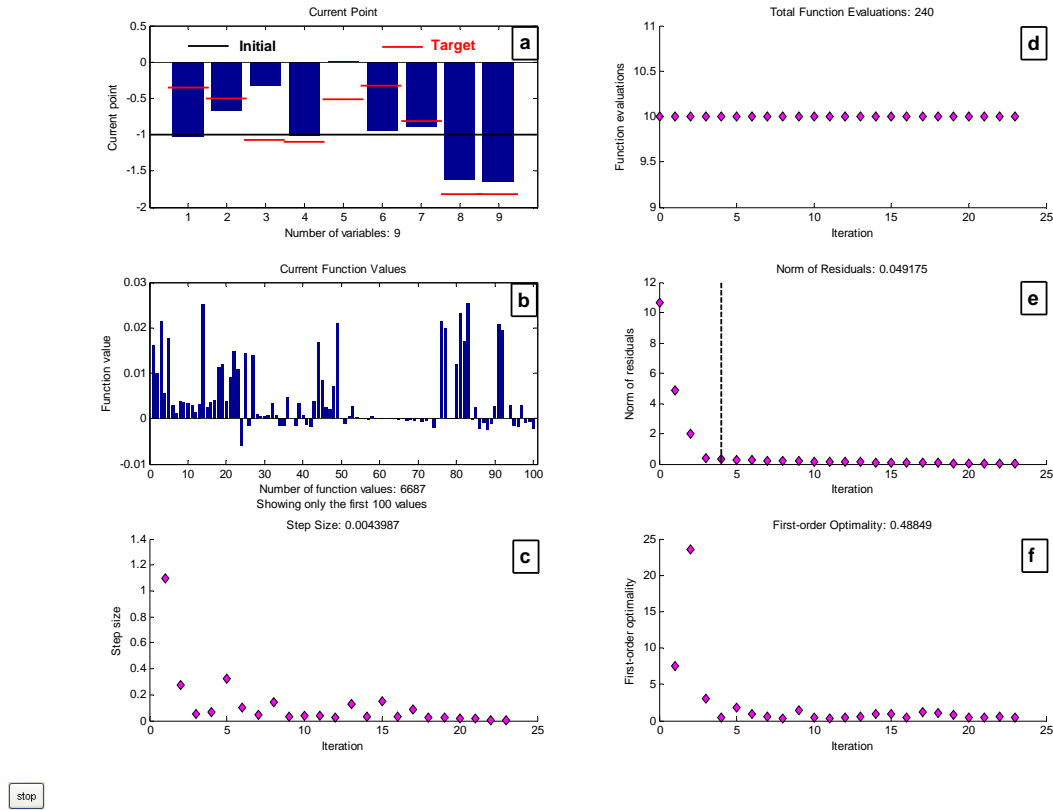


Figure 4-15: Optimization results as a function of iteration, current value (a), function value (b), step size (c), total function evaluation (d), norm of residuals (e), first-order optimality (f)

4.3 Experimental Case

After validating the developed methodology with synthetic and semi-synthetic cases, the proposed history matching approach was used to determine unknown values of oil-water relative permeability for matrix and capillary pressure for both matrix and fracture, corresponding to a spontaneous capillary imbibition experiment. As opposed to synthetic and semi-synthetic cases, time-dependent saturation profiles of spontaneous

capillary imbibition experiment obtained from CT scan data were utilized as the target saturation values for the optimization of controlling parameters describing unknown relative permeabilities and capillary pressure.

The reservoir characteristics and reservoir rock properties used in the preparation of the experimental case was identical to properties used in the semi-synthetic case (Table 4-13) as well as the porosity distribution. However, Timur's correlation given by Eq. 3.2 has been modified to obtain the appropriate permeability distribution controlled by the average permeability of 100 mD since the irreducible water saturation of 0.08 was used after analyzing the experimental saturation distribution at the end of 1072 min. Therefore, the modified Timur's correlation is given by the following Eq. 4.7.

$$k = 0.0168 \frac{\phi^{4.4}}{S_{wirr}^2} \quad 4.7$$

After the implementation of above equation, the permeability distribution presented by Fig. 4-16 was obtained for the construction of the reservoir model.

A discontinuous plane fracture with a permeability of 3000 mD and a porosity of 0.35 was used in the development of the reservoir model. Detailed descriptions of the fracture structure as well as the relative permeability and capillary pressure curves utilized in the model will be presented in chapter 5.1.

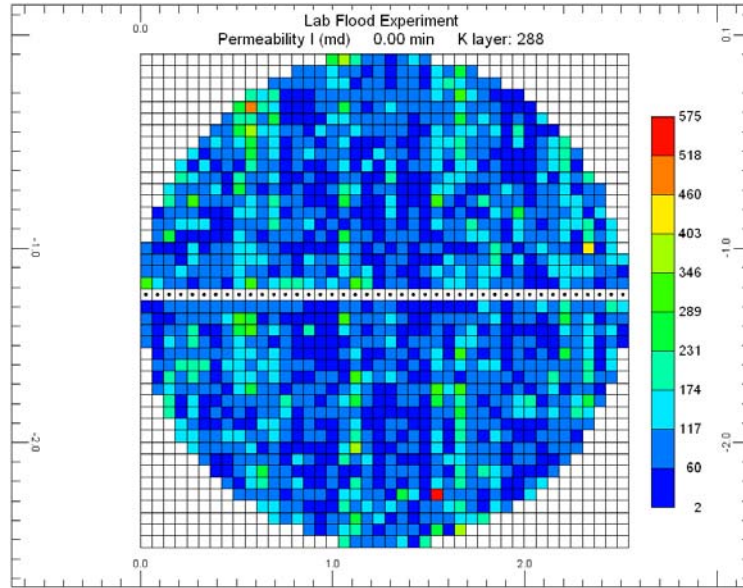


Figure 4-16: Representative areal permeability distribution, mD

4.3.1 Extraction of Time-Dependent Saturation from CT Data

Time-dependent saturation profiles were extracted from CT data to investigate the progression of the imbibing front. Target water saturation was calculated for each volume of element from subtracted CT values using the Eq. 4.8.

$$S_{W,voxel} = S_{W,avg} * \left[1 - \frac{CT_{subtracted,avg} - CT_{subtracted,voxel}}{CT_{subtracted,avg}} \right] \quad 4.8$$

where the average water saturation ($S_{W,avg}$) was 5%, as referenced in the experimental work (Karpyn *et al.*, 2008).

After the implementation of up-scaling scheme by a factor of 5 and Eq. **4.8**, extracted experimental water saturations for CT slices 28.5 mm (a), 9.5 mm (b) and 3 mm (c) above the bottom of the core sample at the end of 1072 min are demonstrated in Fig. **4-17**.

Resulting saturation values corresponding to each slice are different from each other as seen in Fig. **4-17**. There are also saturation alterations within the slice itself, which indicates that multiple flow mechanisms such as countercurrent and co-current flow occurring during the spontaneous imbibition exist as referenced in the study of Karpyn *et al.* (2008). For instance, water saturations are varying in the range of 0-0.22 for the slice 3 mm above the bottom of the core sample (Fig. **4-17.c**) whereas slices located 9.5 mm (Fig. **4-17.b**) and 28.5 mm (Fig. **4-17.a**) above the bottom of the core have saturation values ranging from 0 to 0.18 and 0 to 0.1 respectively. In addition, Fig. **4-17.a** indicates that the injected water propagates as if it was coming from the edges of the fracture, which might be due to the higher permeabilities associated to those fracture blocks at the edges.

Similar observation can be obtained by examining the imbibing front in Fig. **4-18**, Fig. **4-19** and Fig. **4-20** showing longitudinal views of water saturations at the end of 1072 min in yz direction (perpendicular to the fracture plane), xz direction (parallel to the fracture plane) and 3-D views of water saturation the end of 1072 min respectively.

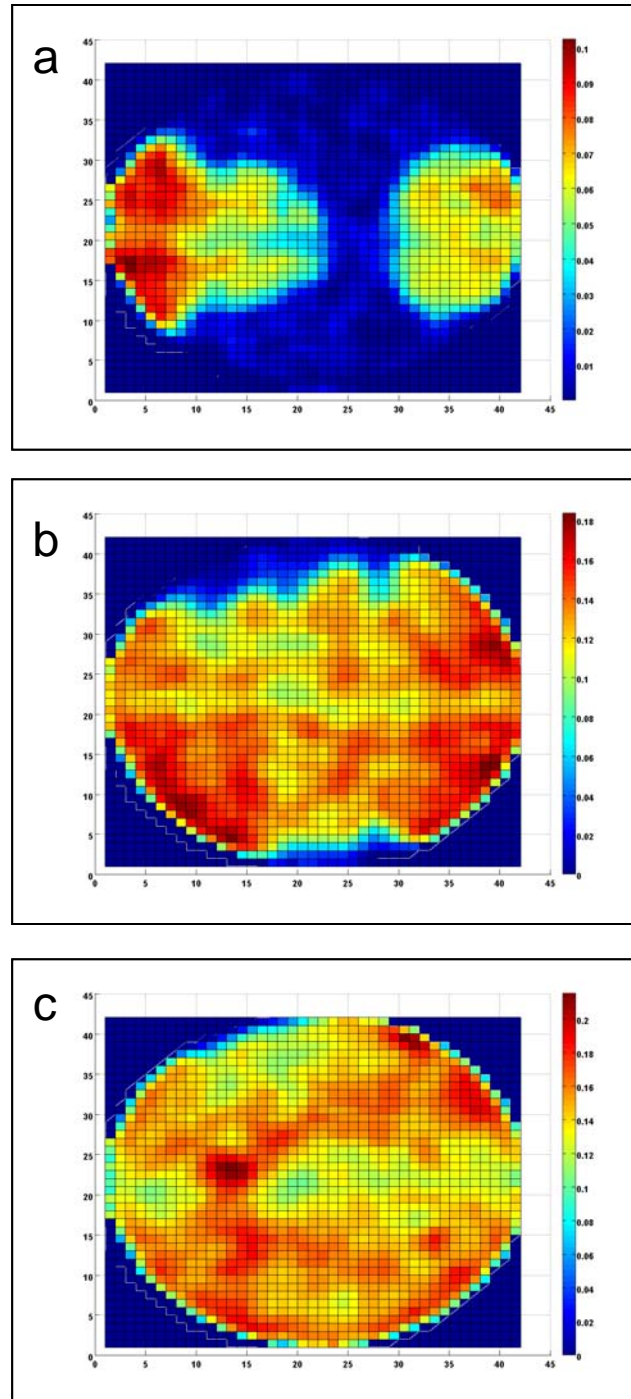


Figure 4-17: Experimental water saturations of CT slice located 28.5 mm (a), 9.5 mm (b) and 3 mm (c) above the bottom of the core sample at the end of 1072 min.

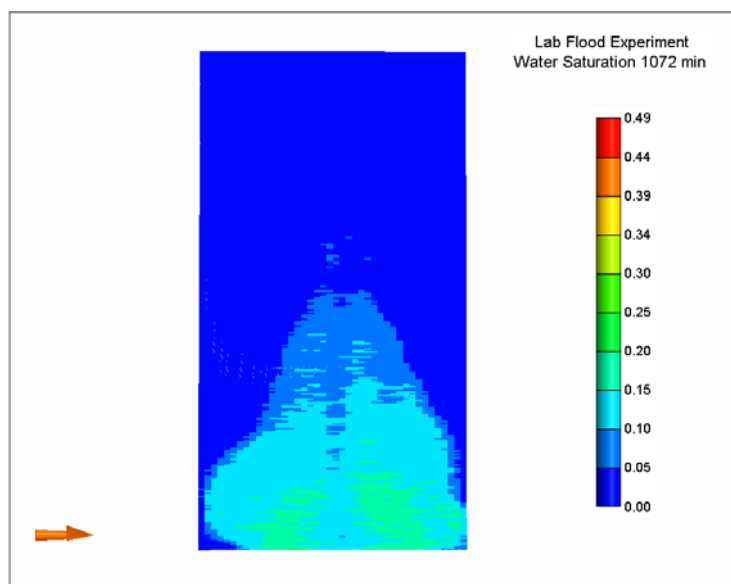


Figure 4-18: Longitudinal representation of experimental water saturation at the end of 1072 min in yz direction perpendicular to the fracture plane

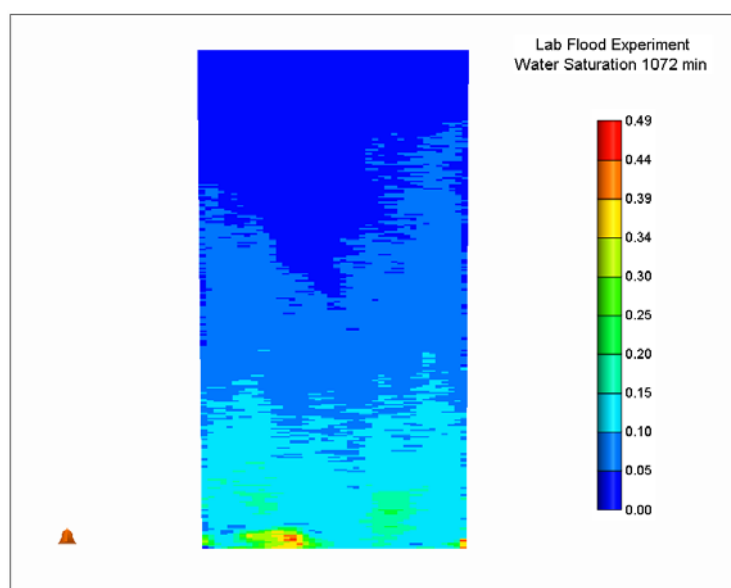


Figure 4-19: Longitudinal representation of experimental water saturation at the end of 1072 min in xz direction parallel to the fracture plane

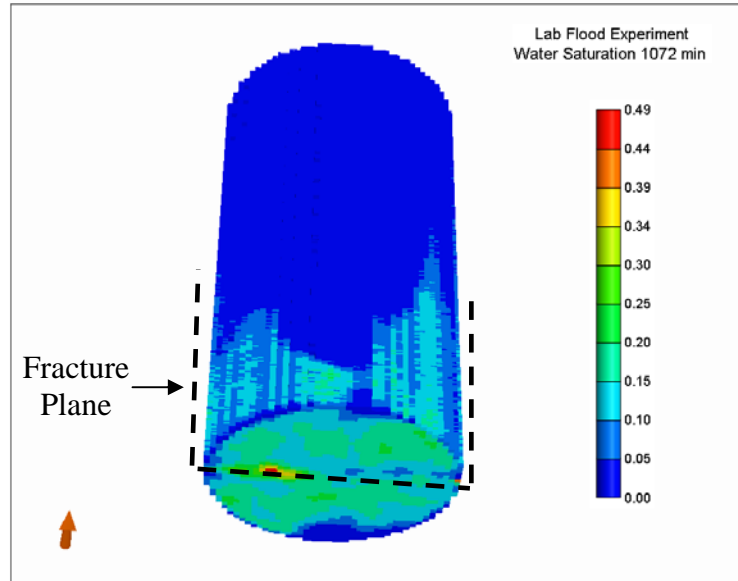


Figure 4-20: 3-D representation of experimental water saturation at the end of 1072 min

4.3.2 Sample Simulation Results

In this section, sample simulation results and observations corresponding to the spontaneous capillary imbibition experiment are presented to better examine the applicability of the proposed history matching approach for determining the unknown transport properties. Similar to the extracted experimental saturation distributions, Fig. 4-21 depicts the simulated water saturation distribution of slices 28.5 mm (a), 9.5 mm (b) and 3 mm (c) above the bottom of the core sample at the end of 1072 min. Moreover, longitudinal views of simulated water saturation in yz and xz directions at the same location of slices together with 3-D representation of water saturation at the end of 1072

min are demonstrated in Fig. 4-22, Fig. 4-23 and Fig. 4-24 respectively. For the three slices presented in Fig. 4-21, the disperse water saturation alterations, as well as the general tendency of water movement obtained in the experiment, could not be observed in the simulation outcomes. Water saturation values stabilize at approximately irreducible water saturation value of 0.08 at the end of simulation (1072 min) in the majority of the core. However, water saturations are varying from 0.08 to 0.2 in the experiments (Fig. 4-17). In addition, the general tendency of water propagation in the simulation results does not correspond with experimental findings (Figs. 4-22, 4-23 and 4-24). For example, the fracture plane was filled up by water having a constant saturation value of 0.08 in the simulation (Fig. 4-22 and Fig. 4-23) whereas water with varying saturations propagated to almost 75% portion of the fracture plane in the experiment (Fig. 4-19). There is also indication in Fig. 4-18 that water moves faster through the edges of the fracture in the experiment, which was not observed in the simulation since the continuous plane fracture with constant permeability and porosity was utilized as the fracture structure. The effect of fracture structure on spontaneous imbibition will be investigated in chapter 5.1 in detail. Therefore, those observations can be attributed to the incapability of simulation model in capturing the multiple flow mechanisms occurred during spontaneous capillary imbibition, which mainly leads to altered saturation values throughout the core. Furthermore, the existence of water propagation through the edges of the fracture plane observed in the experiments might result in those discrepancies between the experimental and simulated saturation values.

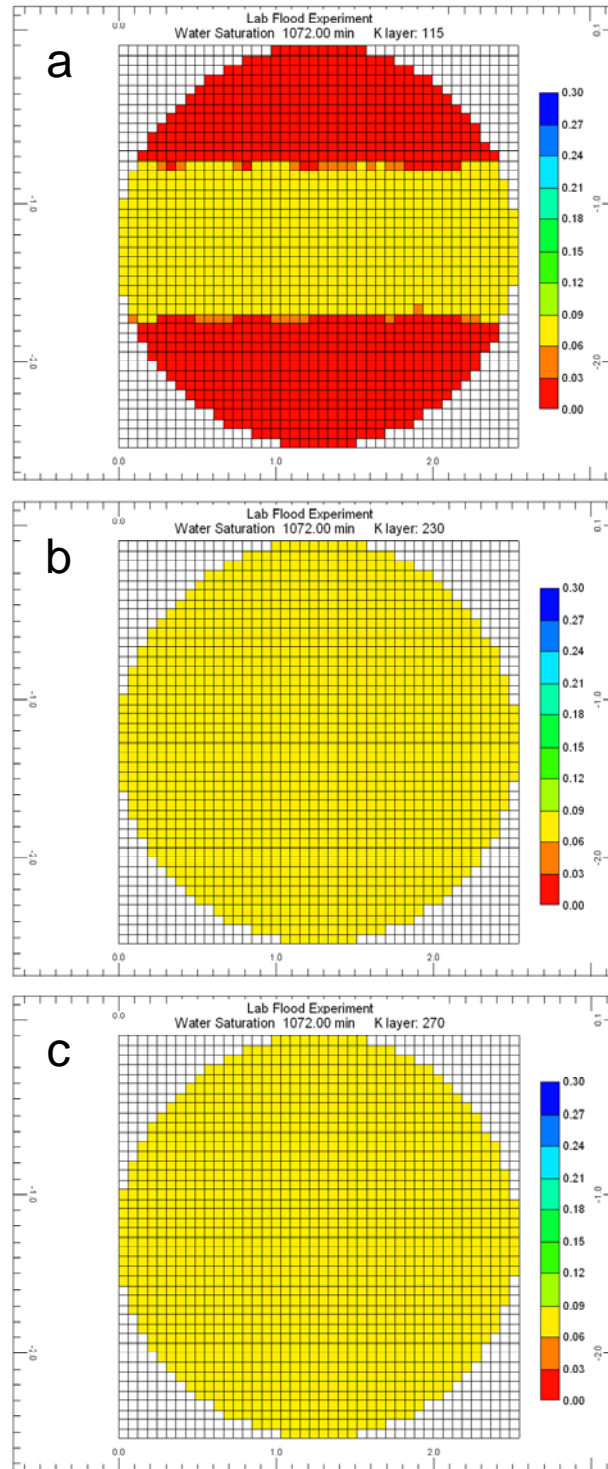


Figure 4-21: Simulated water saturations of CT slice located 28.5 mm (a), 9.5 mm (b) and 3 mm (c) above the bottom of the core sample at the end of 1072 min.

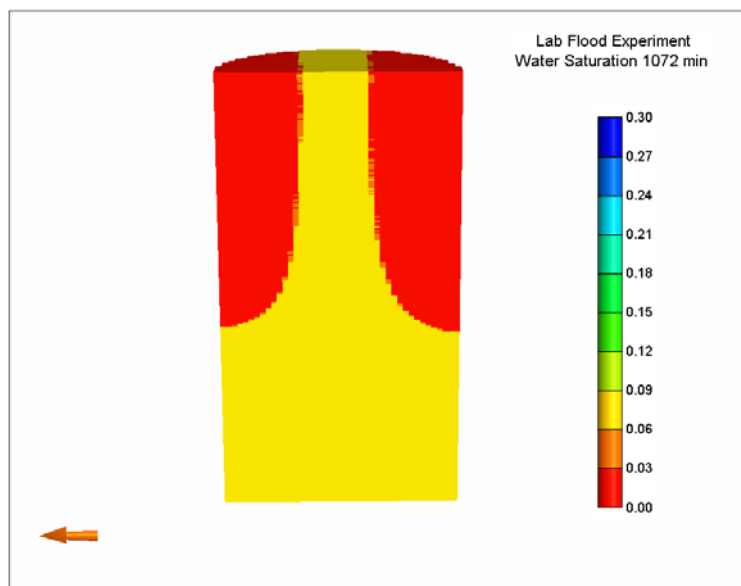


Figure 4-22: Longitudinal representation of simulated water saturation at the end of 1072 min in yz direction perpendicular to the fracture plane

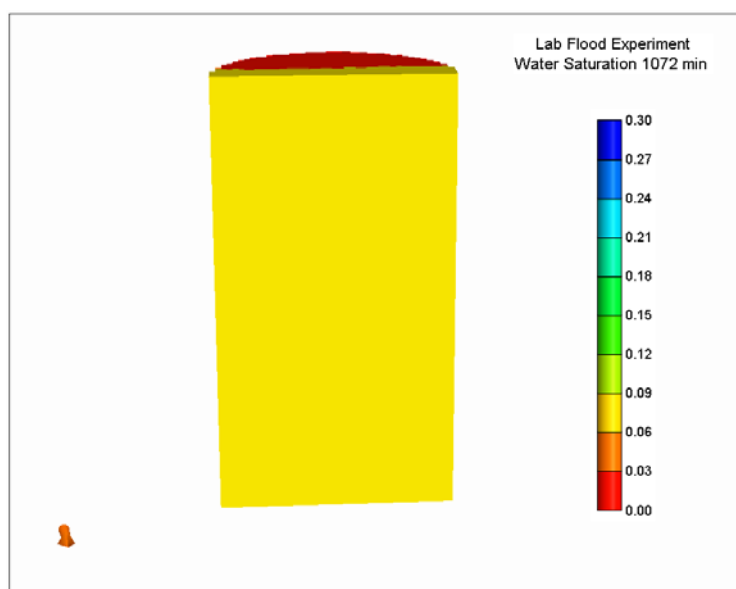


Figure 4-23: Longitudinal representation of simulated water saturation at the end of 1072 min in xz direction parallel to the fracture plane

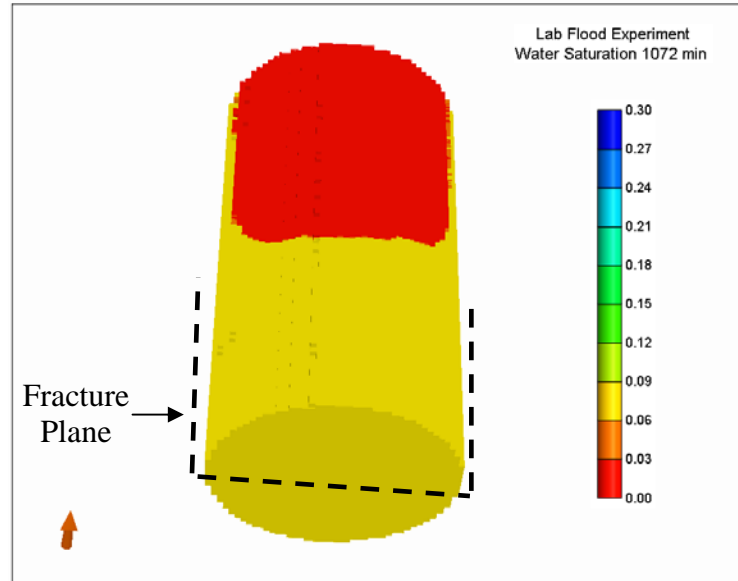


Figure 4-24: 3-D representation of simulated water saturation at the end of 1072 min

Another potential reason for the mismatch of saturations is the fact that hysteresis was ignored in the construction of relative permeability and capillary pressure curves for matrix and fracture, which could allow the model to capture complex flow mechanisms occurring in the experiment. Detailed observations regarding the effect of matrix capillary pressure hysteresis on spontaneous capillary imbibition are discussed in chapter 5.7.

However, similar to the experimental observations (Karpyn *et al.*, 2008), three distinctive flow intervals such as early, intermediate and late-time were identified during the advance of the spontaneous imbibition in the simulation, although the duration of those intervals especially in the early and intermediate periods are different from the experimental findings. An early-time interval covers approximately the first 5 minutes of

imbibition in the simulation whereas experimental observations show 25 minutes of imbibition during an early-time progress of water. Similarly, an intermediate time interval corresponds to a time lapse from 5 minutes to 100 minutes of imbibition in the simulation unlike this interval prolongs between 25 minutes and 100 minutes of imbibition in the experiment. Finally, a late-time interval begins nearly after 100 minutes of imbibition for both simulation and the experiment. Those three time intervals in the simulation are identified in Fig. 4-25 demonstrating the average water saturation in the slice 3 mm above the bottom of the core as well as the average water saturation in the fracture as a function of time for the same slice.

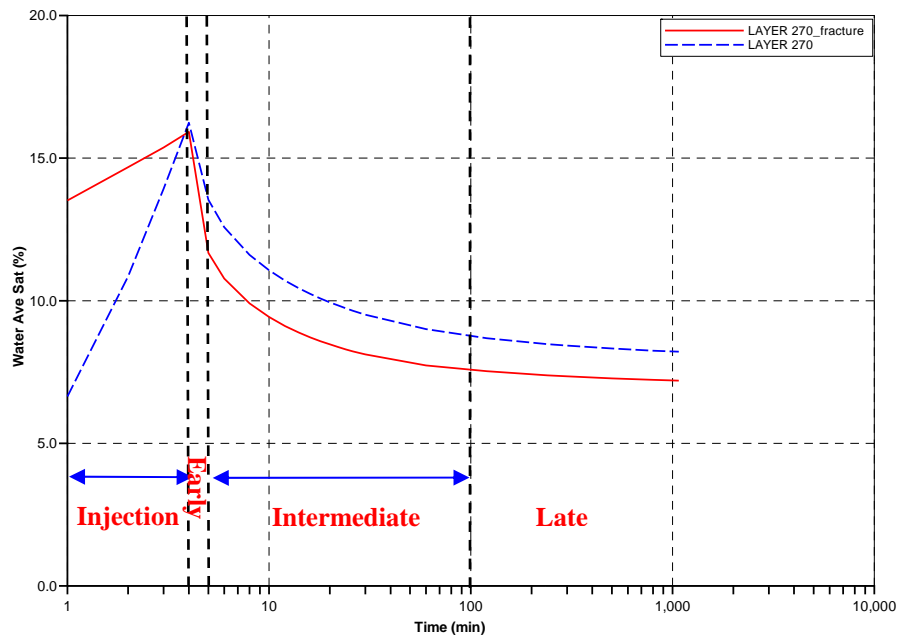


Figure 4-25: Average water saturation in the fracture and in the slice, 3 mm above the bottom of the core

During the injection period, the average water saturation in the fracture for the specified slice varies between 13.5-16% whereas the entire slice has an average saturation value ranging from 7 to 16%. Higher average water saturation in the fracture indicates that water rises up in the fracture plane initially and propagates towards matrix grid blocks later. This observation can be better obtained by analyzing Fig. **4-26** and Fig. **4-27** in which the magnitude of water and oil flux together with their direction at the end of injection period (4 min) are illustrated for the half of slices 28.5 mm (Fig. **4-26.a** and Fig. **4-26.b**) and 3 mm (Fig. **4-27.a** and Fig. **4-27.b**) above the bottom of the core respectively. Half of slices were selected in order to better present the direction of flux since fluid distributions were symmetrical for each half. During this period, water fluxes are moving from the fracture perpendicularly towards matrix blocks for both slices (Fig. **4-26.a** and Fig. **4-27.a**), countercurrent to the oil phase (Fig. **4-26.b** and Fig. **4-27.b**) which is a result of forced imbibition by water injection and oil production through the fracture as well as the existence of capillary contrast in the rock.

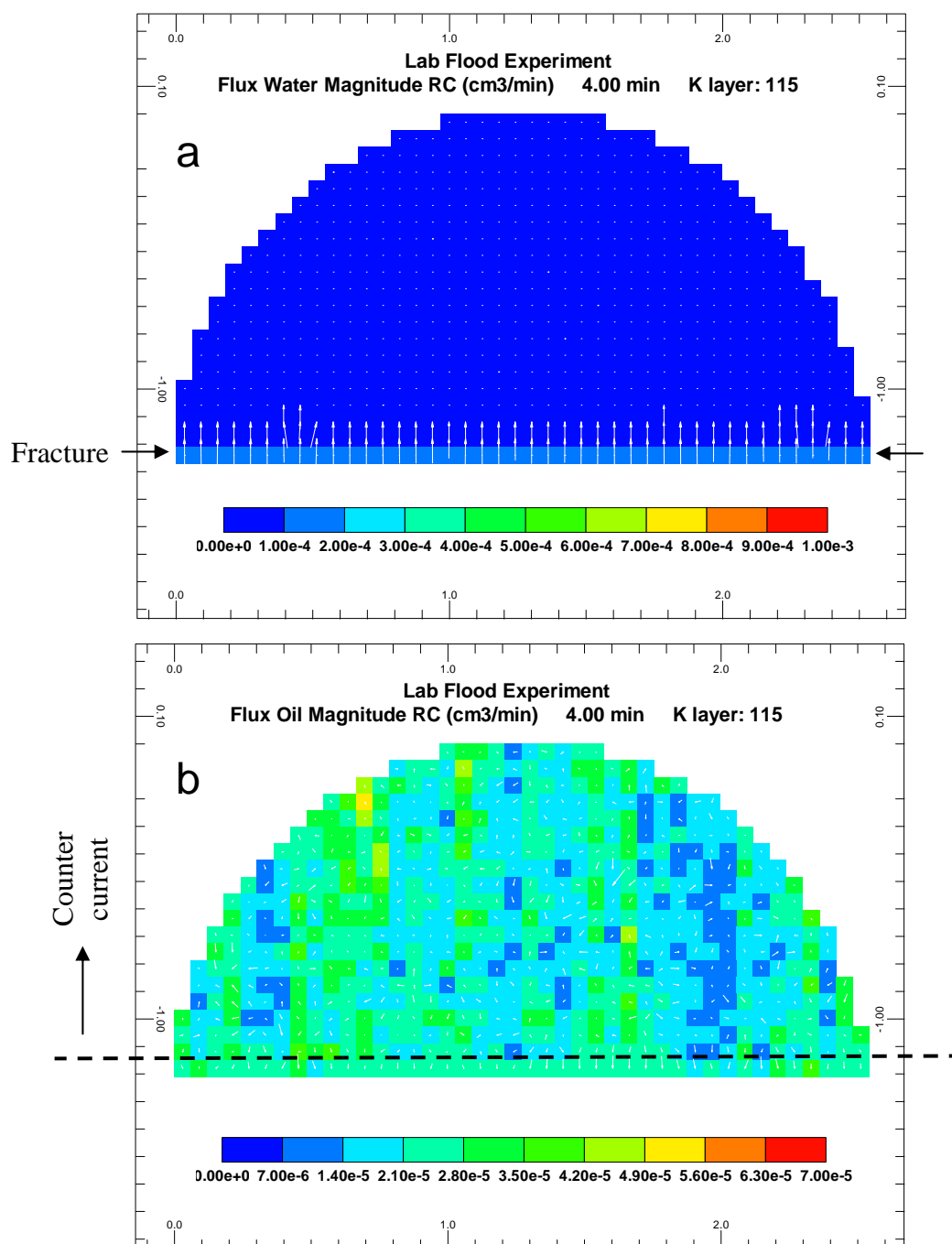


Figure 4-26: Water (a) and oil (b) flux for the slice 28.5 mm above the bottom of the core at the end of injection period (4 min)

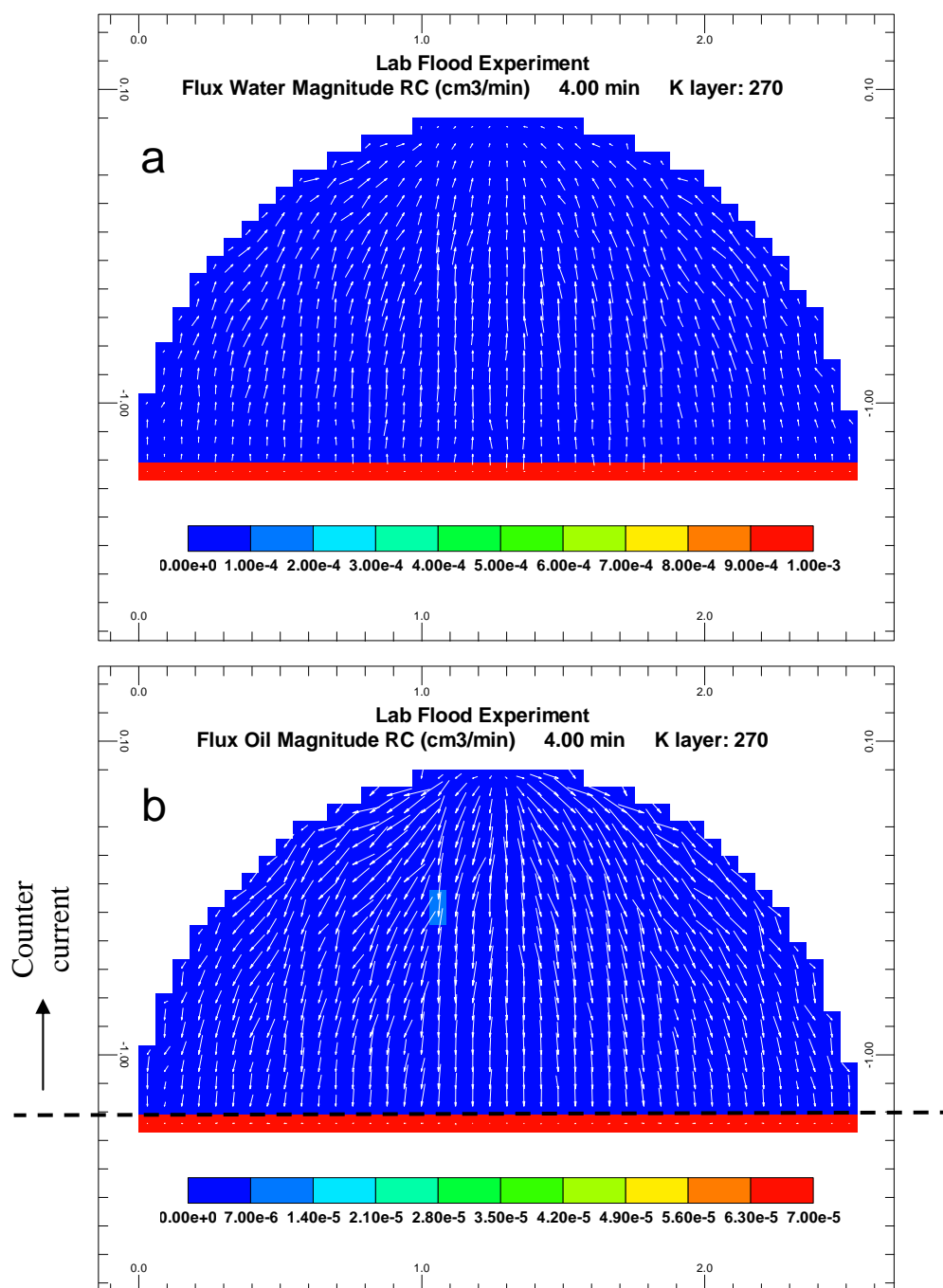


Figure 4-27: Water (a) and oil (b) flux for the slice 3 mm above the bottom of the core at the end of injection period (4 min)

After the injection stopped namely at early-time period, capillary contrast and cross-layer flow are the decisive driving mechanisms for the propagation of water. For the slice 3 mm above the bottom of the core, cross-layer flow in the fracture is more dominant than the capillary contrast, which leads to the water movement towards fracture (Fig. 4-29.a) while oil is leaving from the fracture (Fig. 4-29.b) in a counter-current manner. This observation can also be validated by examining the average water saturation at early-time in Fig. 4-25. Although water is entering the fracture for that slice as indicated above by water flux distributions, the average water saturation significantly decreases in the fracture, which confirms that cross-layer flow in the fracture exists and overcomes the effect of capillary contrast in the rock. On the other hand, water is continuously drained from the fracture for the upper slice 28.5 mm above the bottom of the core due to the strong capillary forces in the matrix (Fig. 4-28.a), still counter-current to oil phase (Fig. 4-28.b). In the light of these observations, it can be concluded that oil recovery from the porous media during the early-time period, takes place essentially through counter-current imbibition, which was also verified by the experimental study of Karpyn *et al.* (2008). Similar counter-current oil-water flow behaviors are observed for the lower slice at intermediate (Fig. 4-31) and late (Fig. 4-33) time intervals. However, oil and water flow in opposite directions for the upper slice at intermediate (Fig. 4-30) and late (Fig. 4-32) time periods compared to directions in the lower slice, in which counter-current flow prevails in the region adjacent to the fracture.

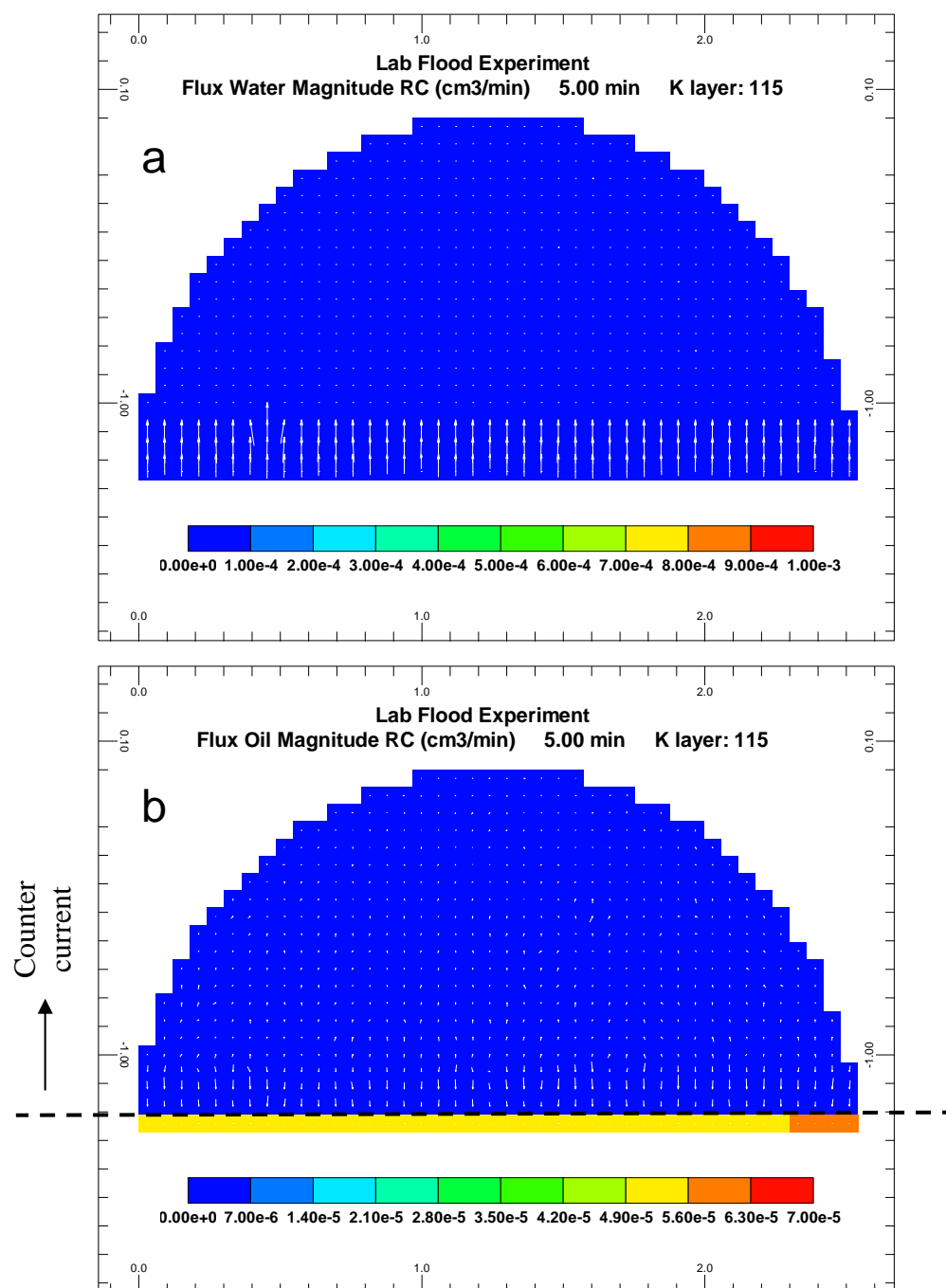


Figure 4-28: Water (a) and oil (b) flux for the slice 28.5 mm above the bottom of the core at early-time period (5 min)

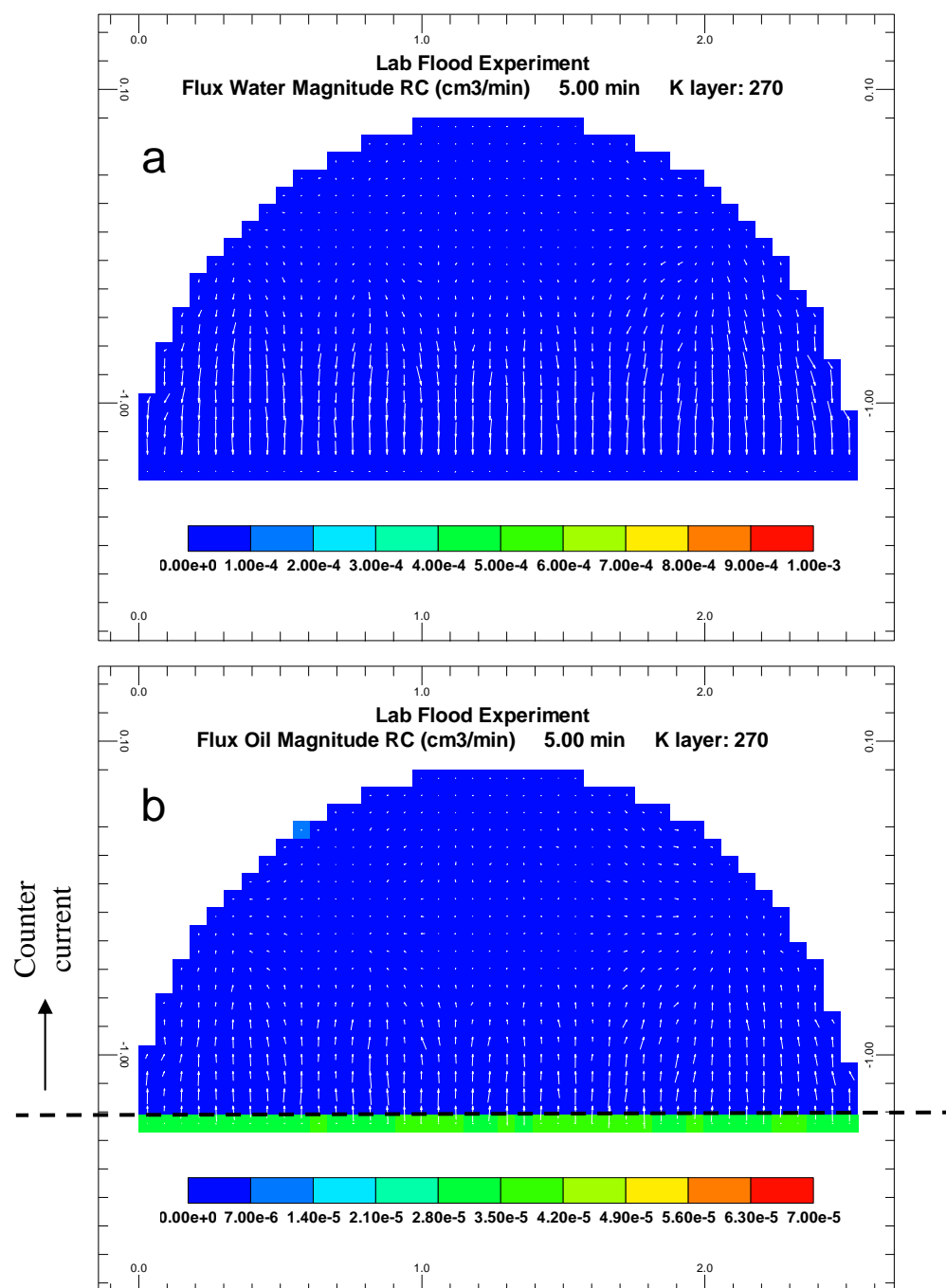


Figure 4-29: Water (a) and oil (b) flux for the slice 3 mm above the bottom of the core at early-time period (5 min)

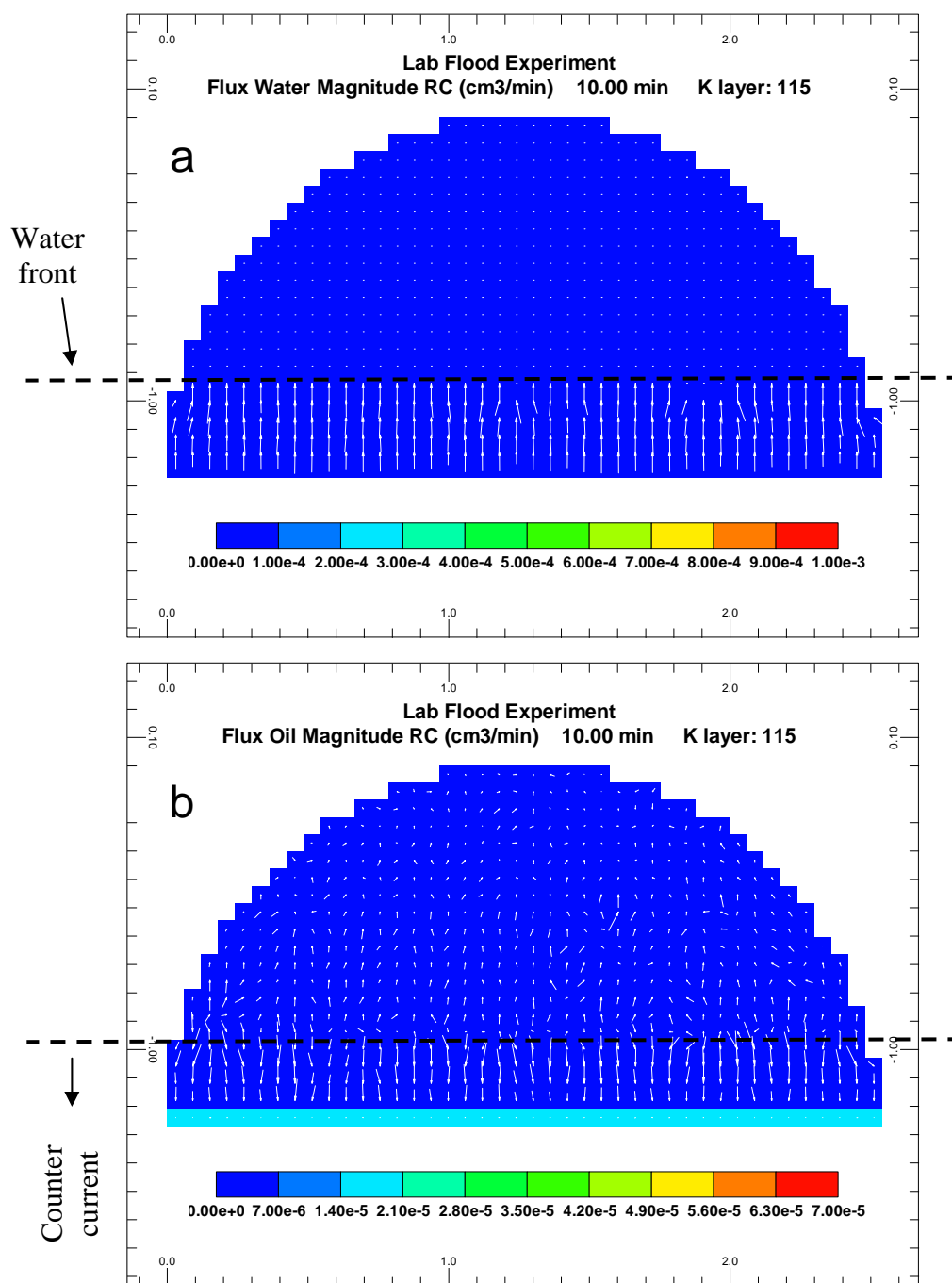


Figure 4-30: Water (a) and oil (b) flux for the slice 28.5 mm above the bottom of the core at intermediate-time period (10 min)

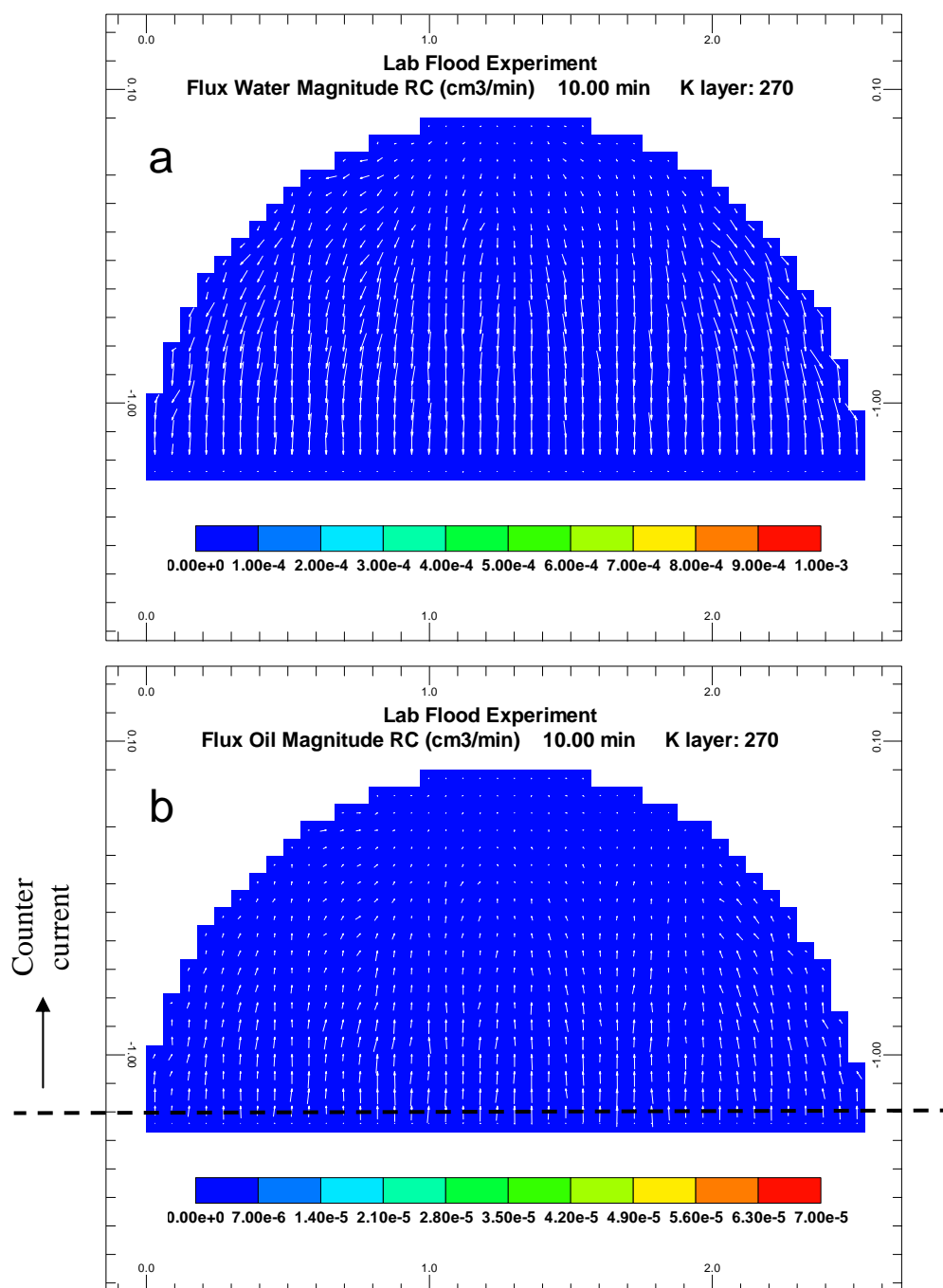


Figure 4-31: Water (a) and oil (b) flux for the slice 3 mm above the bottom of the core at intermediate-time period (10 min)

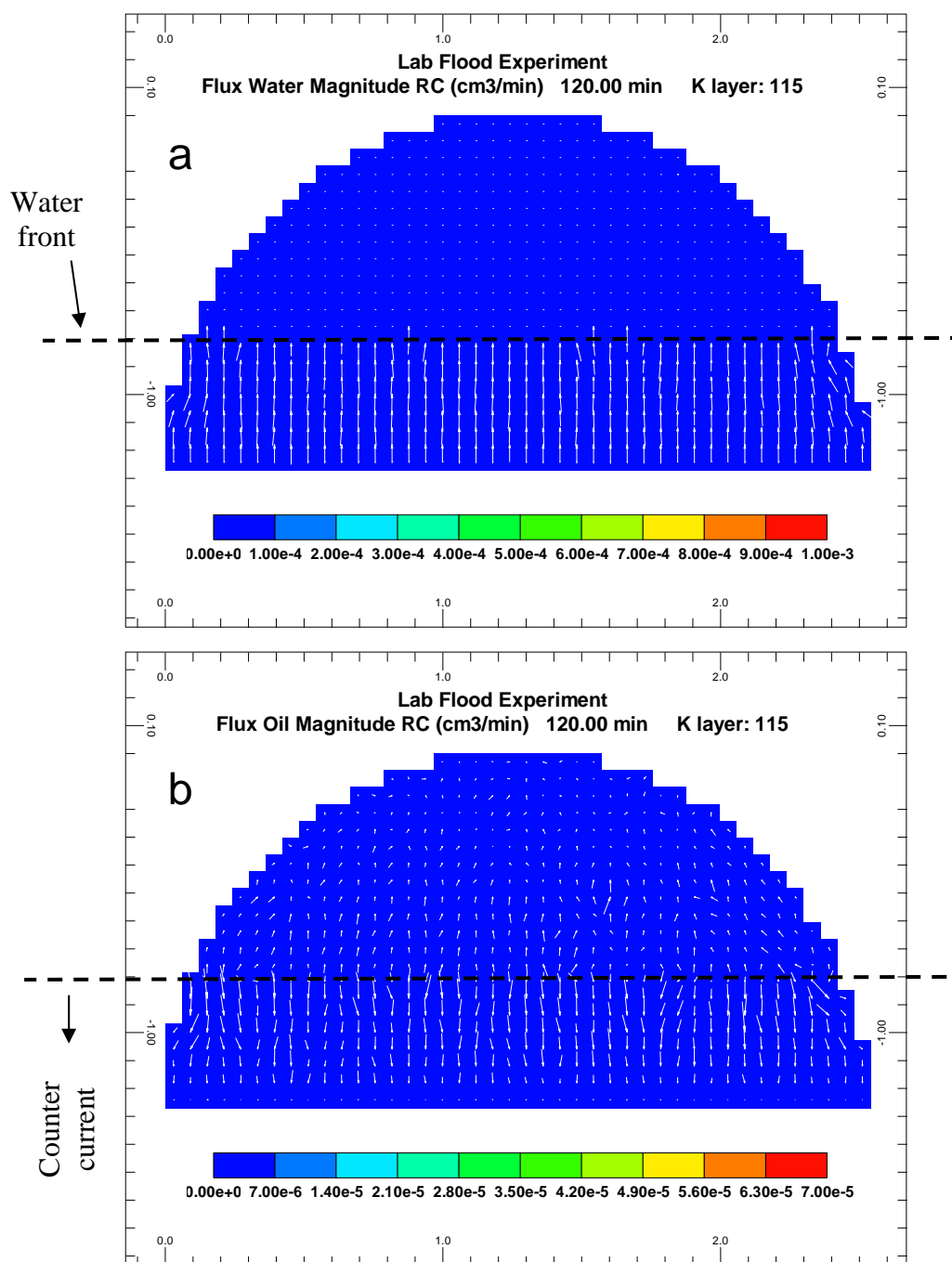


Figure 4-32: Water (a) and oil (b) flux for the slice 28.5 mm above the bottom of the core at late-time period (120 min)

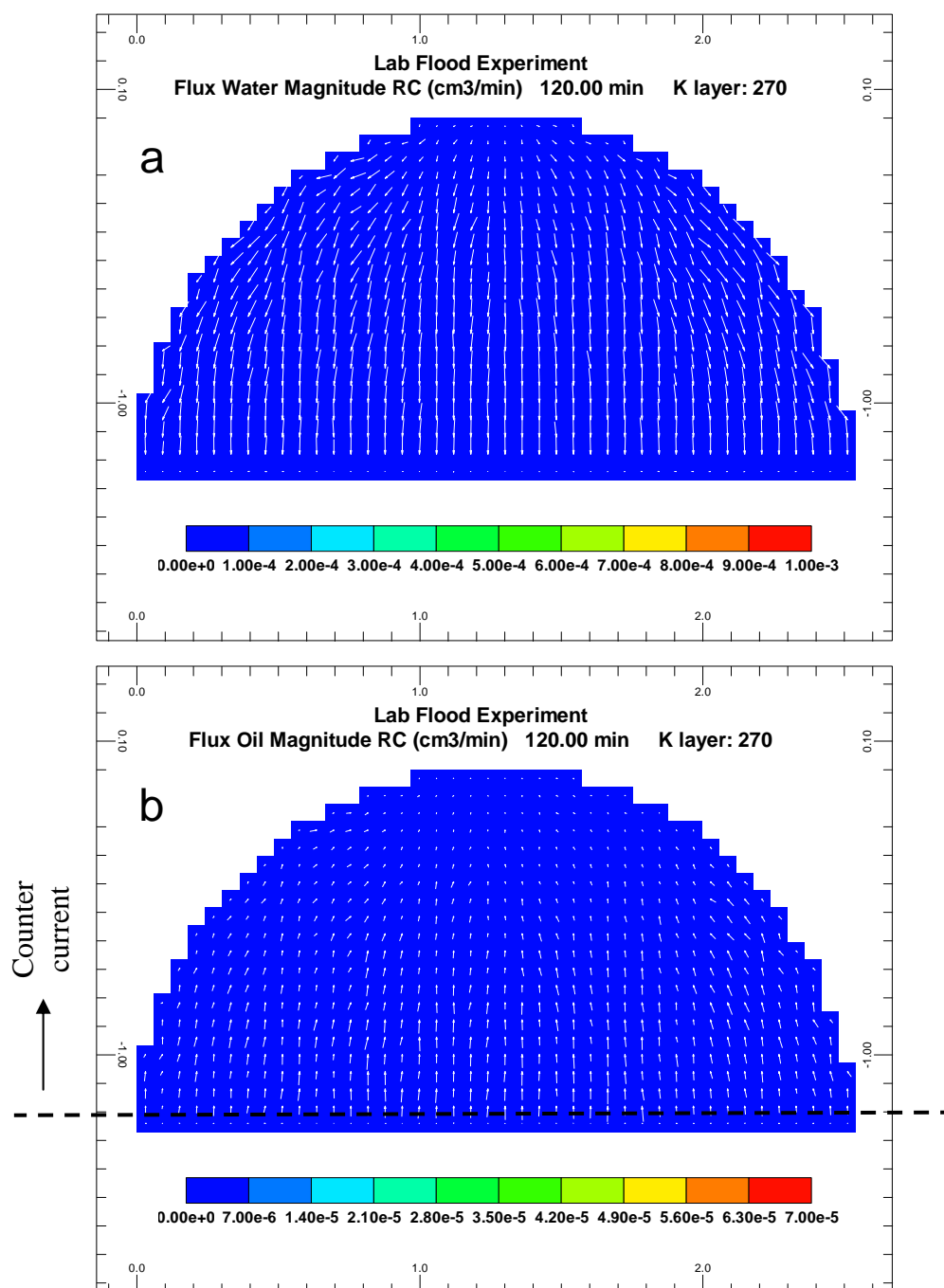


Figure 4-33: Water (a) and oil (b) flux for the slice 3 mm above the bottom of the core at late-time period (120 min)

After observing the sample simulation results, the optimization was performed in the entire core sample to determine the relative permeability and capillary pressure curves for matrix and fracture. However, the optimization was terminated after couple of iterations due to the mismatch of saturation values as well as the incapability of the simulation model in capturing the complex flow mechanisms existing during the spontaneous imbibition as a result of aforementioned observations while comparing the experimental and simulated outcomes. Therefore, sensitivity analyses were conducted in order to better investigate the effects of matrix and fracture transport properties on spontaneous imbibition for the construction of proper simulation models corresponding to experiment.

Chapter 5

Sensitivity Analysis

In this chapter, sensitivity analyses were performed in order to analyze the effects of some transport properties of the fracture and matrix on the spontaneous capillary imbibition process. Particularly, impacts of the fracture structure, capillary pressure and relative permeability in the matrix as well as the fracture, fracture permeability and capillary hysteresis in the matrix on the spontaneous imbibition will be presenting in the following sections.

5.1 Fracture Structure

Two different fracture structures, a discontinuous and a continuous plane fracture were used in the construction of the reservoir model to investigate the effects of fracture structure on spontaneous capillary imbibition. The discontinuous fracture structure was defined using the methodology described in chapter 3.1, whereas the continuous fracture structure corresponds to the central longitudinal plane separating the core into two identical halves. As previously described in chapter 3.1, three different up-scaling schemes were implemented in the construction of the reservoir model (Fig.3-2). Those reservoir models were compared according to their fracture connectivity presented in Fig. 5-1. A reservoir model constructed by using an up-scaling scheme factor of 5 in x, y and z directions is presented in Fig. 5-1.a. Remaining reservoir models were obtained by

implementing an up-scaling scheme factor of 7 in x, y and 10 in z directions (Fig. **5-1.b**) and a factor of 10 in all directions (Fig. **5-1.c**) respectively. Red color represents fracture blocks unlike matrix blocks are illustrated by blue color in all three figures. It can be detected from those figures that the intensity of fracture blocks indicated by red colors as well as their connectivity diminishes while moving from Fig. **5-1.a** through Fig. **5-1.c**. This observation validates that the selection of an up-scaling scheme factor of 5 in all directions would be appropriate to maintain reasonable amount of fracture blocks in addition to sustain their connectivity for fluid flow purposes. Therefore, an up-scaling scheme factor of 5 in all directions was used in the implementation of both discontinuous and continuous fracture structures.

The discontinuous fracture structure is presented by water-oil capillary pressure distribution of the reservoir model in Fig. **5-2** and Fig. **5-3**. Similarly, Fig. **5-4** and Fig. **5-5** represent the longitudinal and cross-sectional views of the reservoir model with continuous fracture structure respectively. In all four figures, fracture blocks are represented by blue color whereas red color indicates the location of matrix blocks. Both fracture structure are a way of interpreting a fracture that we are familiar with from the experimental description. They were also created in such a way that the pore volume of the experimental fracture was sustained in the construction of the reservoir model. Reservoir rock and fluid properties for both cases given by Table 4-12 were used in the reservoir model with additional properties of a fracture permeability of 3000 mD and a fracture porosity of 0.35.

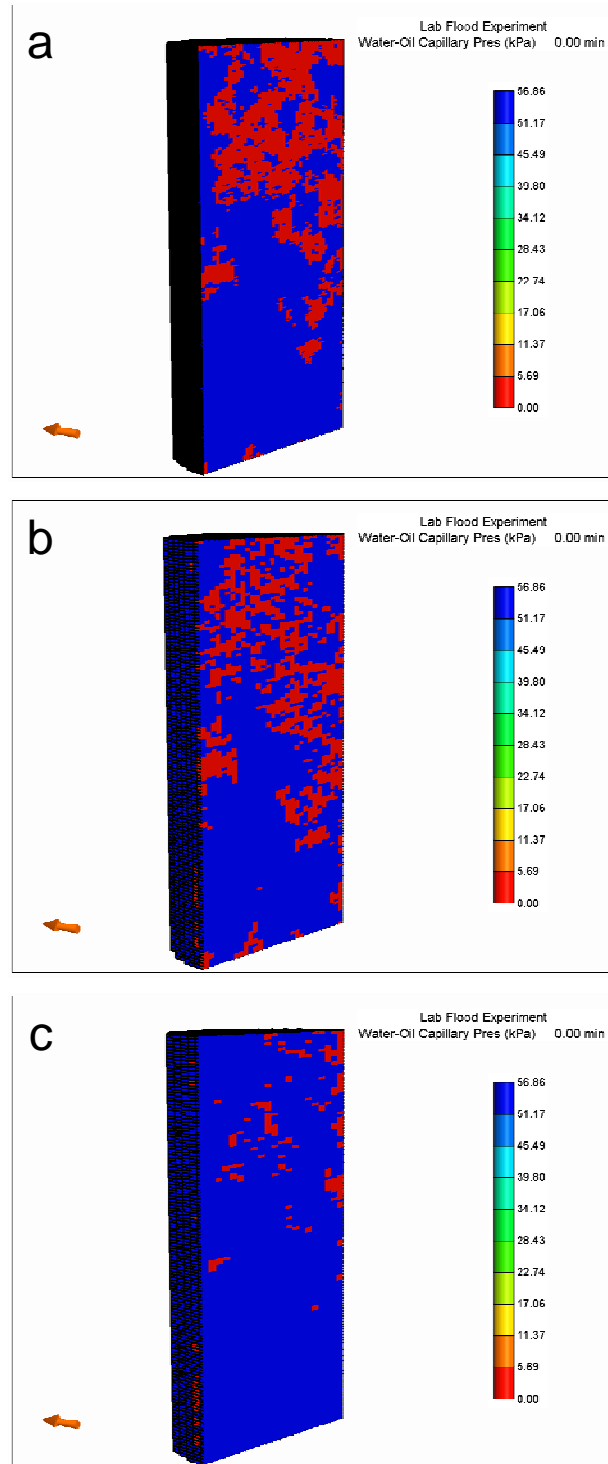


Figure 5-1: Comparison of up-scaling schemes, factor of 5 in all directions (a), factor of 7 in x, y and factor of 10 in z direction (b), and factor of 10 in all directions (c)

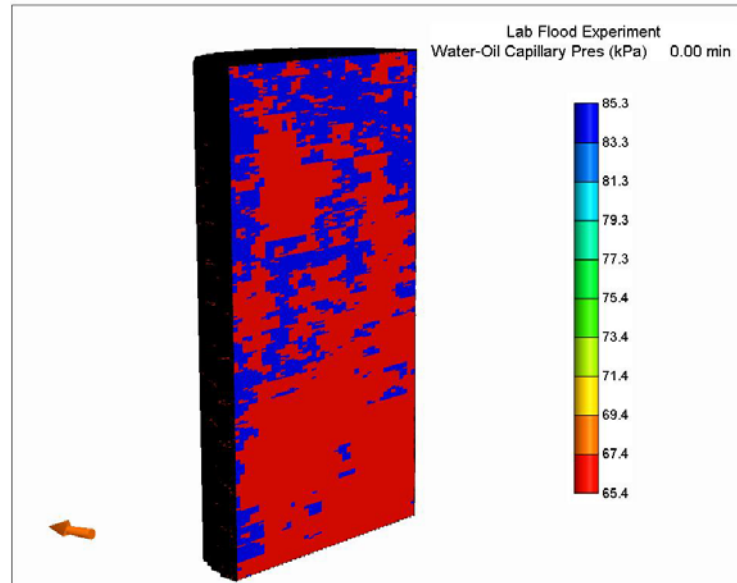


Figure 5-2: Longitudinal (xz) representation of the reservoir model with discontinuous fracture structure (blue: fracture, red: matrix)

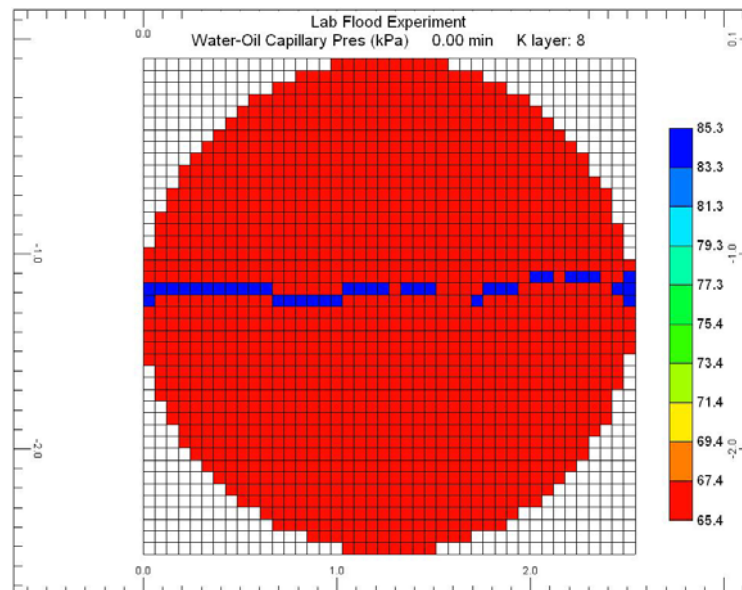


Figure 5-3: Cross-sectional (xy) representation of the reservoir model with discontinuous fracture structure (blue: fracture, red: matrix)

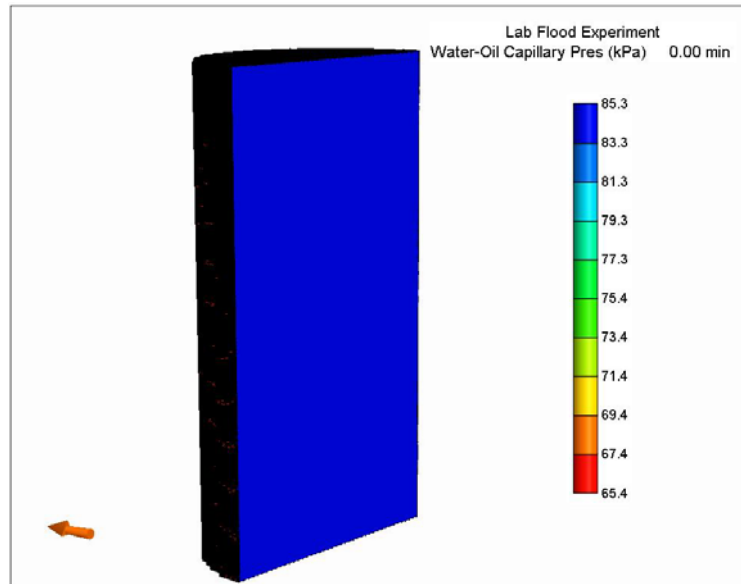


Figure 5-4: Longitudinal (xz) representation of the reservoir model with continuous fracture structure (blue: fracture, red: matrix)

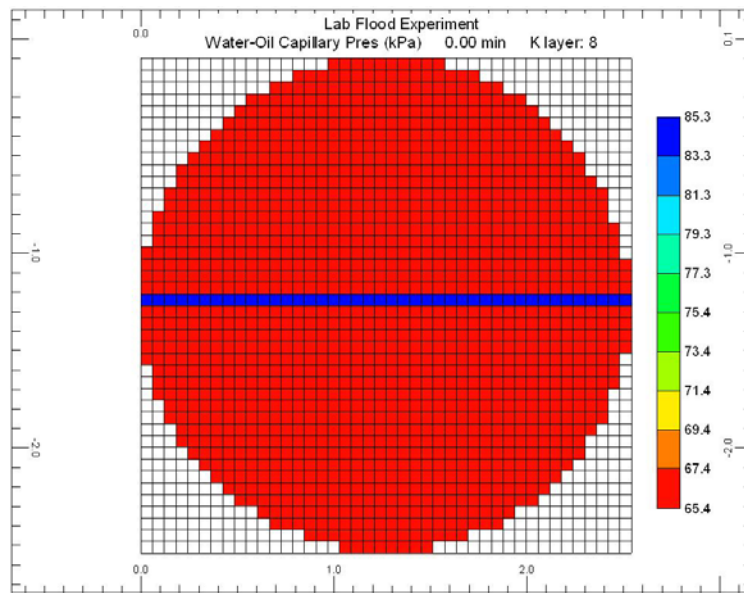


Figure 5-5: Cross-sectional (xy) representation of the reservoir model with continuous fracture structure (blue: fracture, red: matrix)

Capillary pressure and relative permeability curves for both fracture and matrix are illustrated in Fig. 5-6 and Fig. 5-7 respectively. Those relative permeability curves in Fig. 5-7 were constructed using the cubic B-spline representations expressed by Eq. 3.8 and Eq. 3.9. For capillary pressure curves presented in Fig. 5-6, Brooks and Corey (1964) definitions given by Eq. 4.6 were used with the selection of constants such as CP_c and CP_{cf} equal to 13.79 and 5.686 respectively. For the construction of both transport properties, irreducible water saturation of 0.08 and 0.05 residual oil saturation were used in the implementations of Eq. 3.8, Eq. 3.9 and Eq. 4.6.

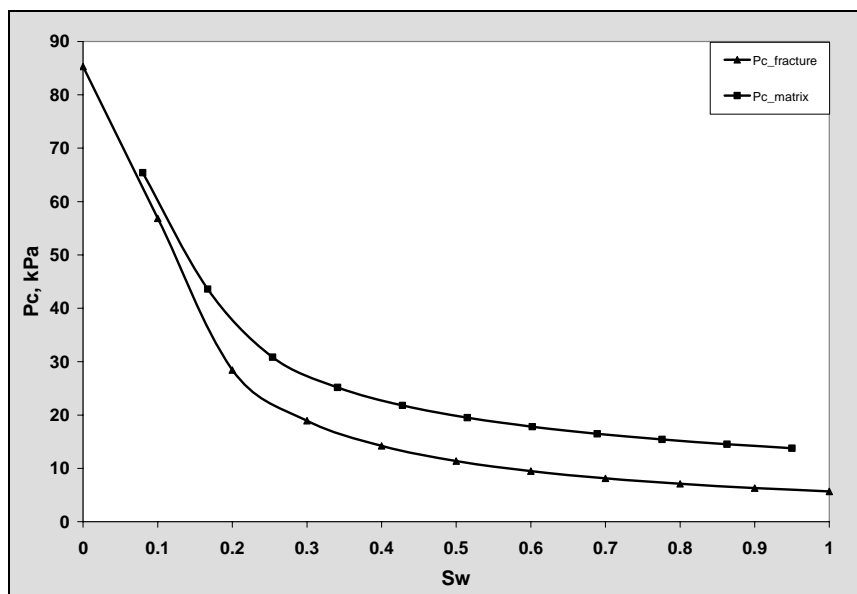


Figure 5-6: Capillary pressure vs water saturation for matrix and fracture

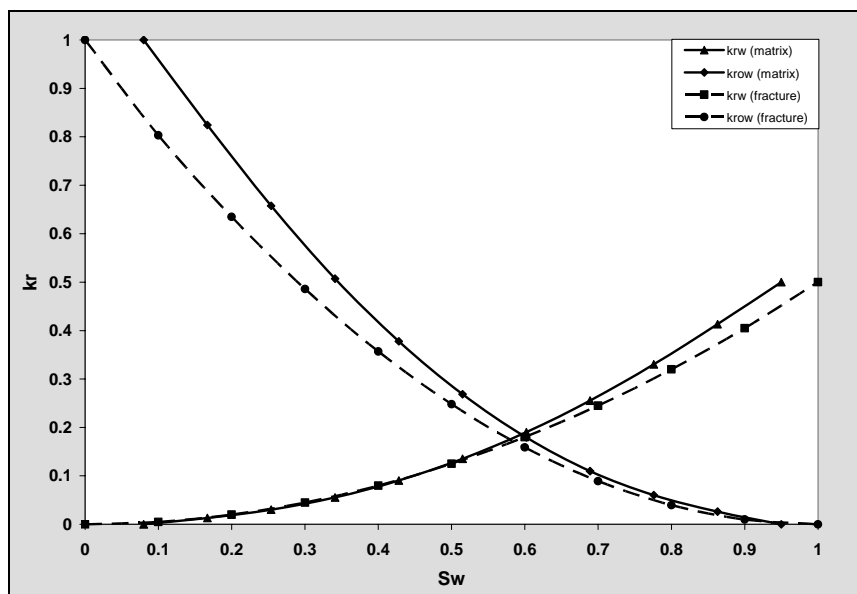


Figure 5-7: Relative permeability vs water saturation for matrix and fracture

After the preparation of reservoir models with two different fracture structures, these models were simulated for 1072 min to investigate the effect of fracture structure on the spontaneous imbibition process. Simulation models were prepared in such a way that they mimicked the spontaneous capillary imbibition experiment. The resulting cross-sectional and longitudinal views of water saturation distribution for both cases at six different simulation times (1, 2, 4, 5, 10 and 1072 min) are demonstrated in Fig. 5-8 - Fig. 5-11. Cross-sectional (xy) water saturation distributions are illustrated in Fig. 5-8 and Fig. 5-10 by presenting the water saturation distribution of the slice which is 3 mm above the bottom of the core sample. Similarly, longitudinal views of the reservoir model in xz direction indicating water saturation distribution in the fracture plane are shown in Fig. 5-9 and Fig. 5-11 for both cases respectively. It can be perceived from Fig. 5-8 and Fig. 5-10 that more cross-sectional (xy) water propagations in the matrix with higher water saturation values indicated by dark blue color were observed within the injection period for the case of discontinuous fracture. After the injection stopped (after 4 min), no significant difference between both cases was noticed in the distribution of water saturation for the selected slice in which final water saturations stabilized around the value of irreducible water saturation (0.08) at the end of the simulation (1072 min). In addition, a piston-like displacement in the fracture resulting in more water propagations due to the connectivity of fracture grid blocks was detected in the case of continuous fracture (Fig. 5-11) whereas no flat water front in the fracture was obtained by implementing the discontinuous fracture structure (Fig. 5-9). Similar observation can be obtained from Fig. 5-12 by examining the average water saturation distribution in the fracture with respect to time. For both fracture structures, the average water saturation in

the fracture increases with time during the injection period in which the average water saturation peaks at a value of 10% for the continuous fracture case whereas maximum of 6% average water saturation was observed for the discontinuous fracture structure case. However, the most significant difference between both structures was obtained during the spontaneous imbibition process (after 4 min). The average water saturation is increasing with respect to time for discontinuous fracture case unlike continuous fracture structure leads to a decrease in the average water saturation after the injection. This decreasing tendency in the average water saturation in the fracture for the continuous fracture structure case could also be validated by the experimental observations (Karpyn, *et al.*, 2008). Therefore, the continuous plane fracture structure was used to examine the effect of other parameters on spontaneous imbibition for the rest of analysis since the connectivity of fracture grid blocks was guaranteed in the implementation of this structure as well as its consistency with the experimental observations. In addition, the capillary pressure and relative permeability curves for both matrix and fracture given in Fig. 5-6 and Fig. 5-7 were used as a base case for the rest of sensitivity analyses. As a result of those observations, it can be concluded from this section that the fracture structure, and consequently the continuity of the fracture, have a significant impact on the encroachment of water throughout the core and therefore corresponding reservoir models should be carefully developed for the accurate representation of experiments.

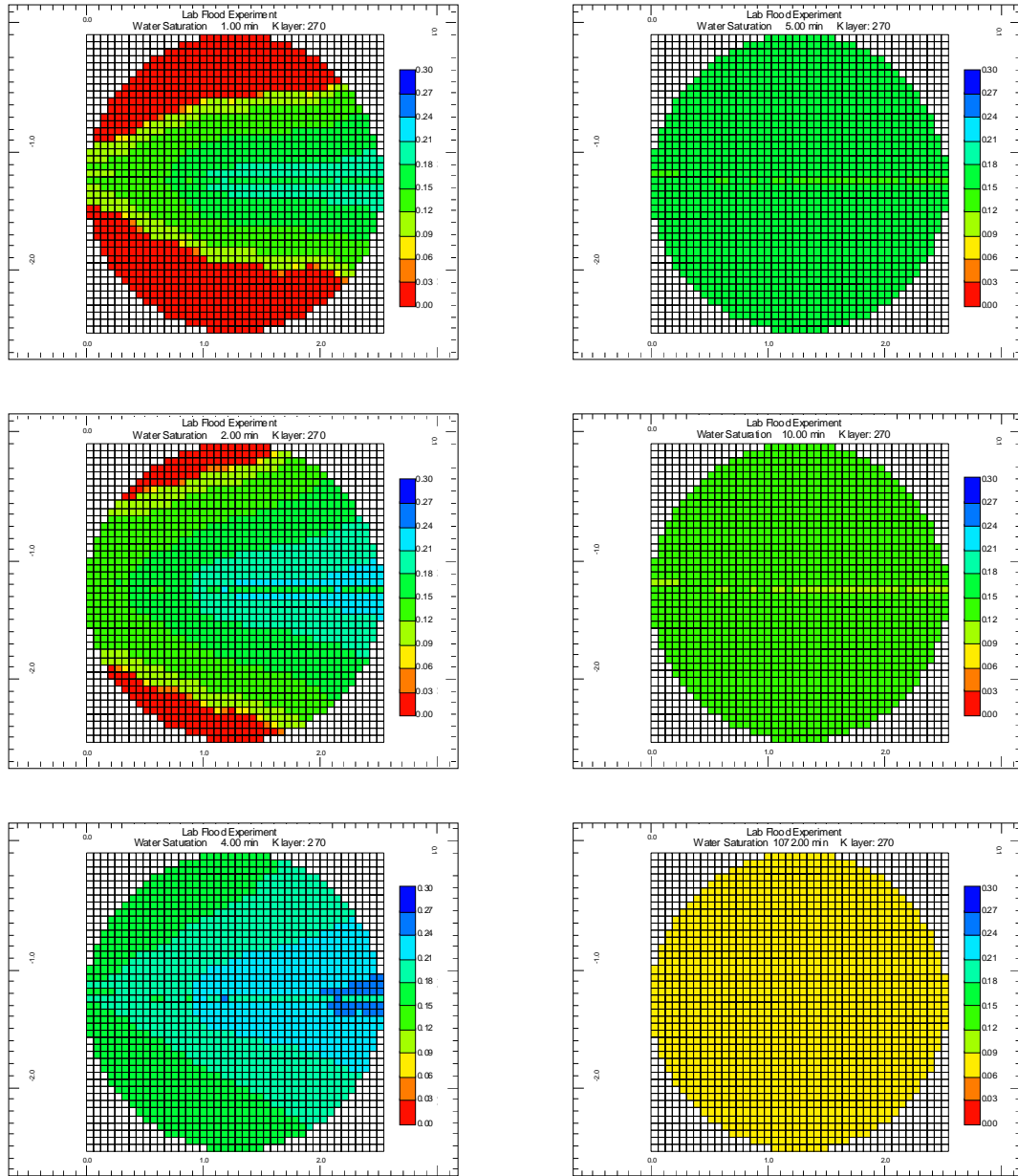


Figure 5-8: Cross-sectional (xy) water saturation distribution of the slice 3 mm above the bottom of the core model with discontinuous fracture structure

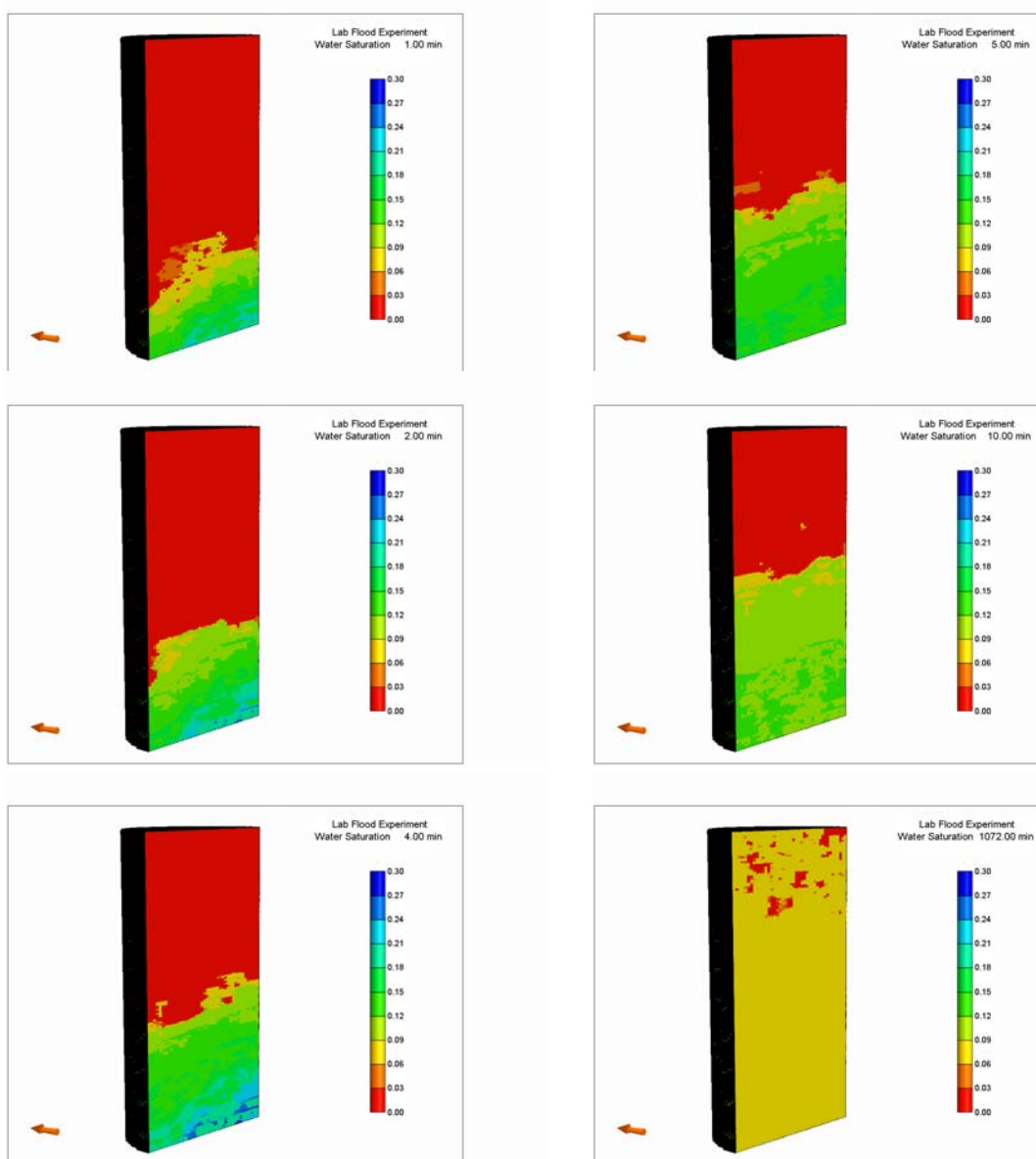


Figure 5-9: Longitudinal (xz) water saturation distribution of the core model with discontinuous fracture structure

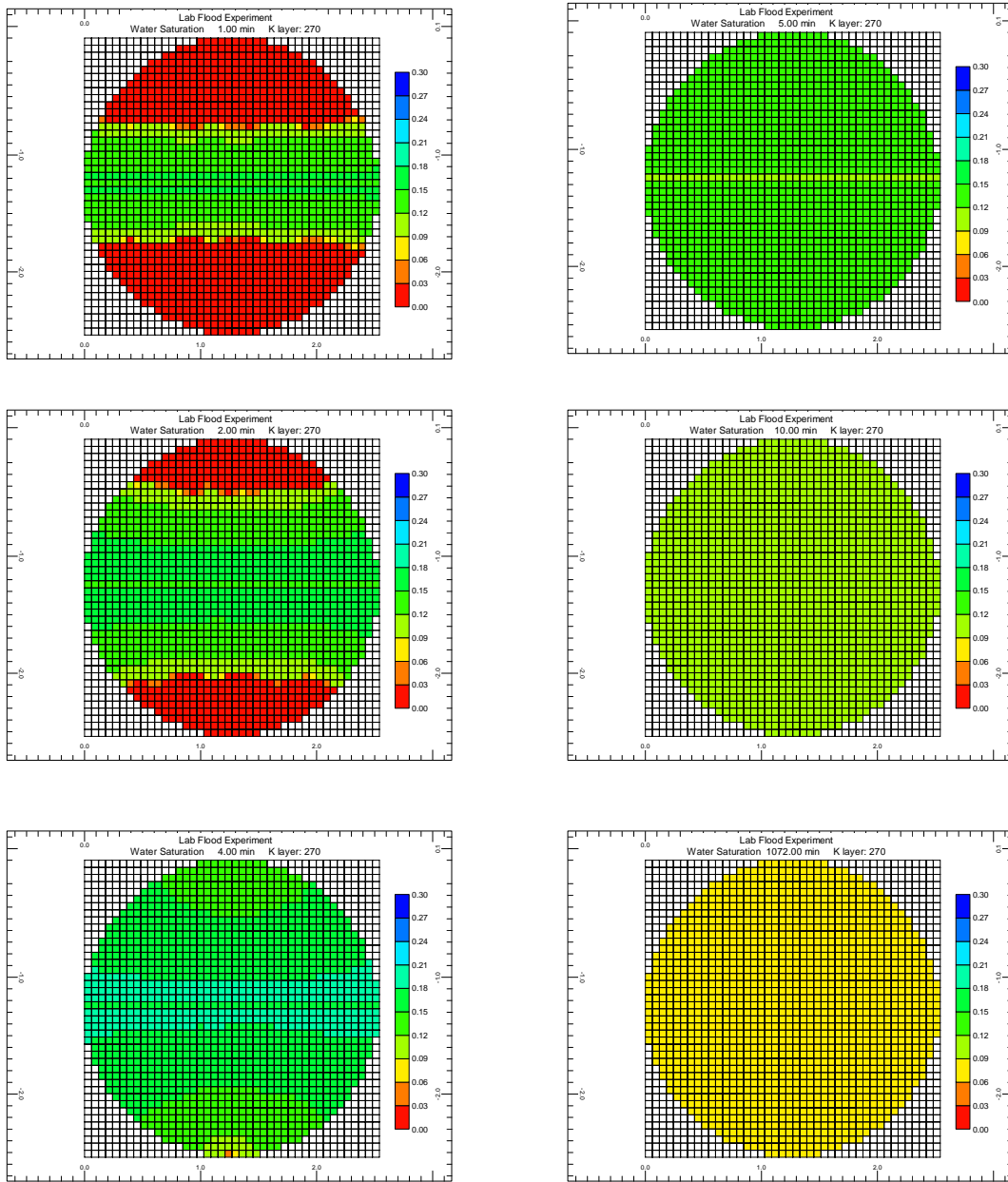


Figure 5-10: Cross-sectional (xy) water saturation distribution of the slice 3 mm above the bottom of the core model with continuous fracture structure

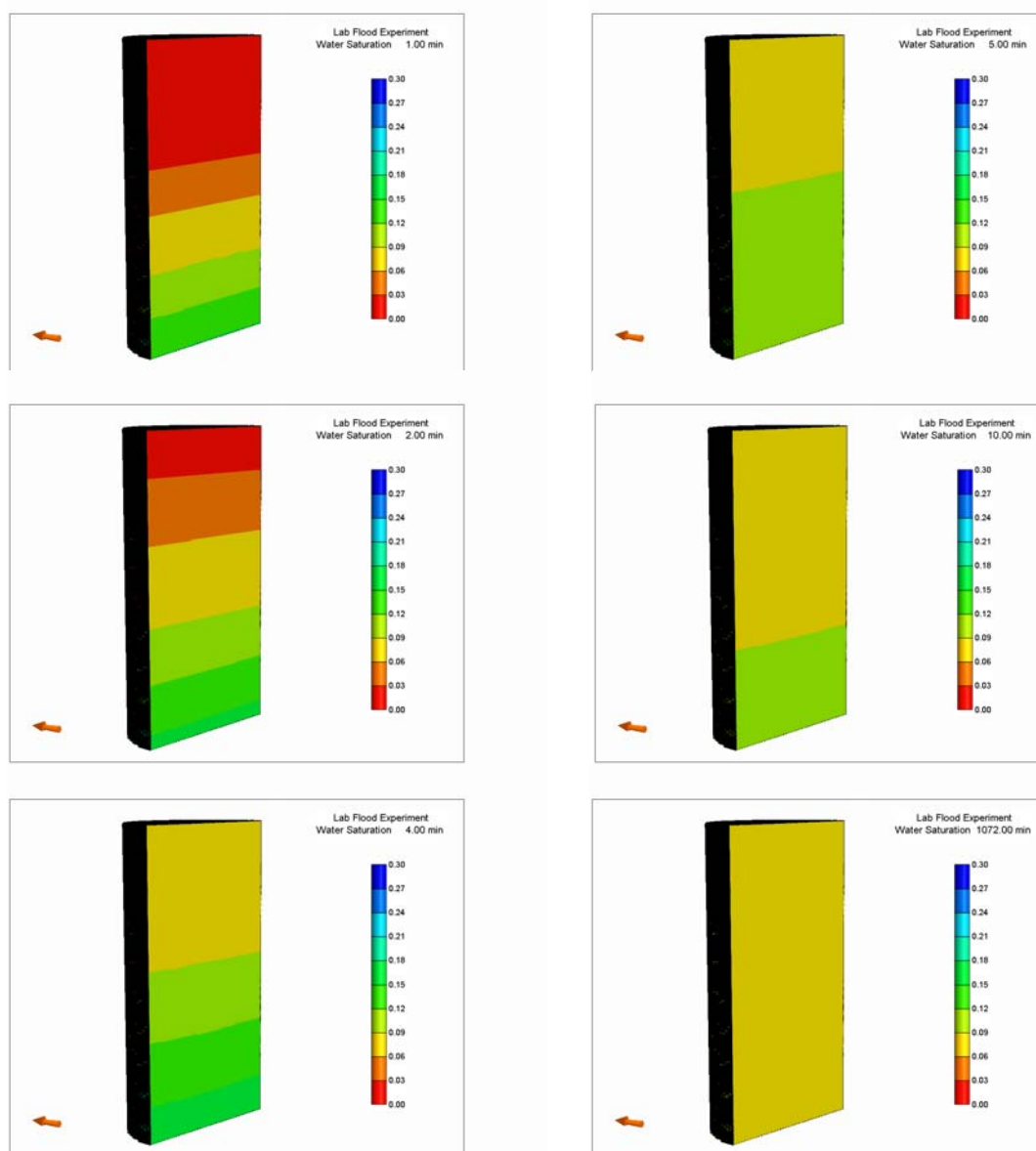


Figure 5-11: Longitudinal (xz) water saturation distribution of the core model with continuous fracture structure

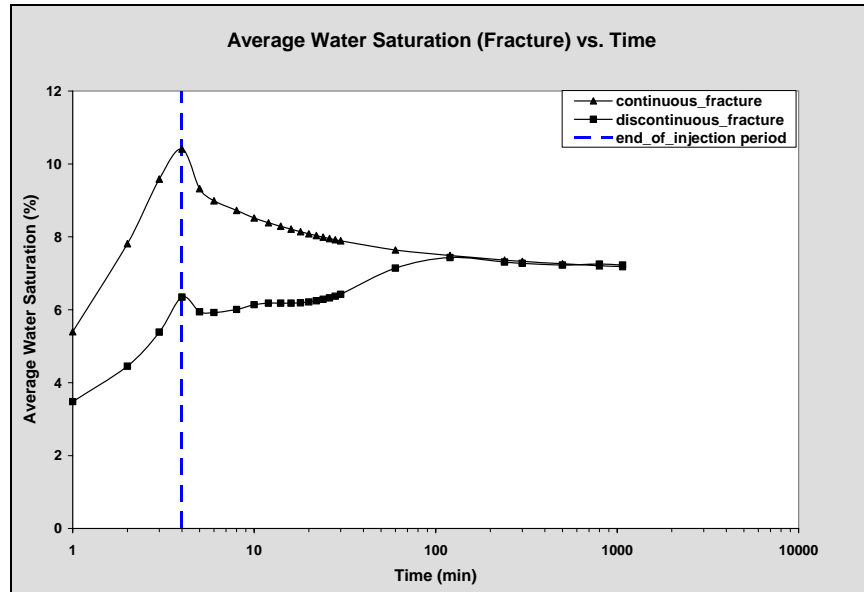


Figure 5-12: Average water saturation in the fracture as a function of time

5.2 Matrix Capillary Pressure

Three different matrix capillary pressure curves shown in Fig. 5-13 were used in this analysis to examine the effect of matrix capillary pressure on spontaneous capillary imbibition. In addition to matrix-fracture capillary pressure curves given as a base case in section 5.1, two other curves were constructed by selecting higher values of CP_c such as 17.2375 and 20.67 respectively to maintain the matrix capillary pressure greater than the fracture capillary pressure. After simulating the three cases for 1072 min, 3-D representations of water saturation distributions were obtained as in Fig. 5-14 through Fig. 5-16.

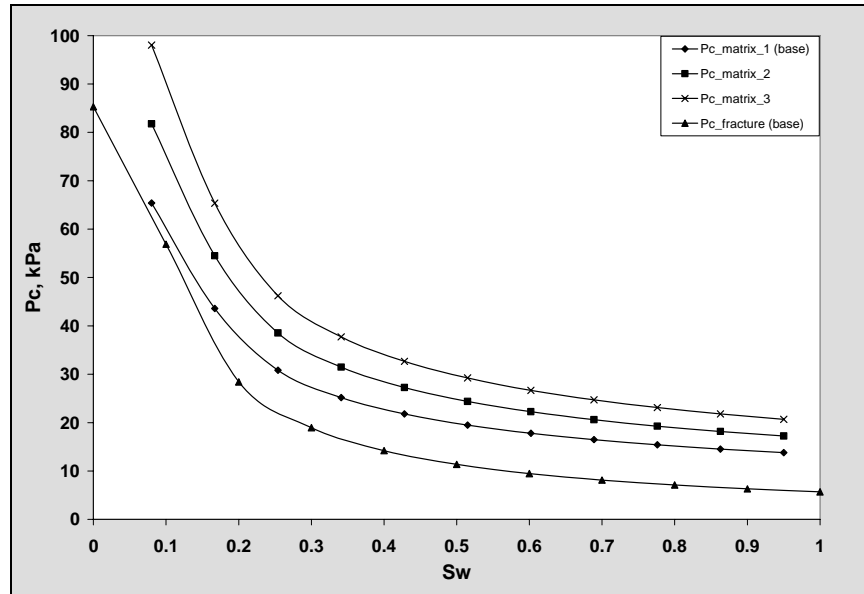


Figure 5-13: Capillary pressure vs water saturation for matrix and fracture

It is observed from those figures that the increase in matrix capillary pressure as moving from the base case (Fig. 5-14) to the third case (Fig. 5-16) causes more areal water propagation in the matrix as opposed to the fracture. Water is drained from the fracture at the end of simulation due to the strong capillary forces in the matrix for the second case (Fig. 5-15) and the third case (Fig. 5-16). This observation can be attributed to the relative difference between the matrix capillary pressure and the fracture capillary pressure. The increase in the relative difference between two capillary forces leads to more water encroachment through the matrix blocks since the capillary pressure is the most dominant driving mechanism in spontaneous imbibition processes. Moreover, experimental observations indicate that the injected water is rising up in the fracture initially and then starts to propagate to the matrix blocks, which also requires a small difference between the matrix capillary pressure and the fracture capillary pressure.

Therefore, the matrix capillary pressure should be balanced with the fracture capillary pressure in the development of these types of reservoir model in order to mimic the experimental results adequately.

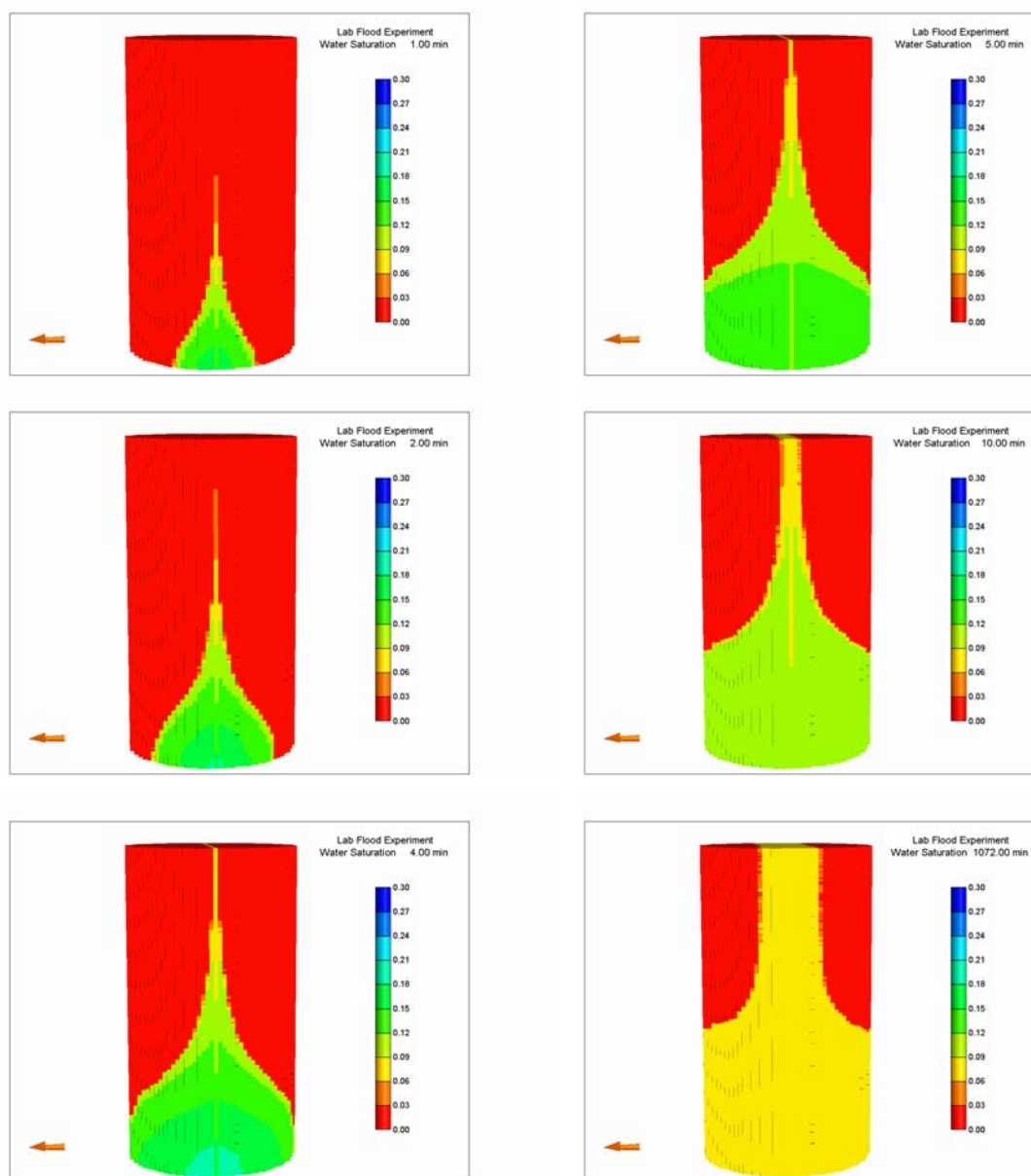


Figure 5-14: 3-D Representations of water saturation distribution for the model developed by using Pc_matrix_1 curve (base)

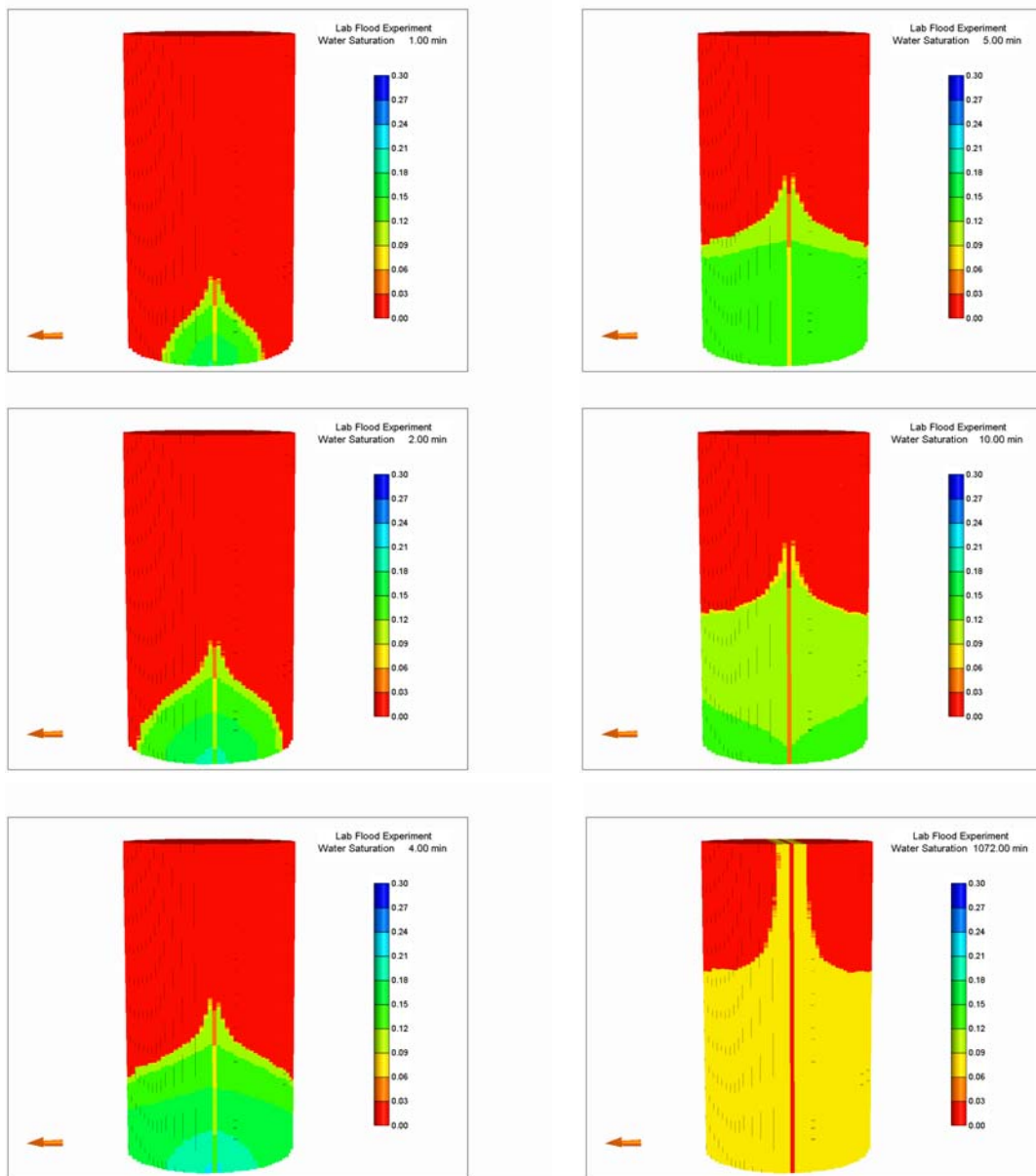


Figure 5-15: 3-D Representations of water saturation distribution for the model developed by using Pc_matrix_2 curve

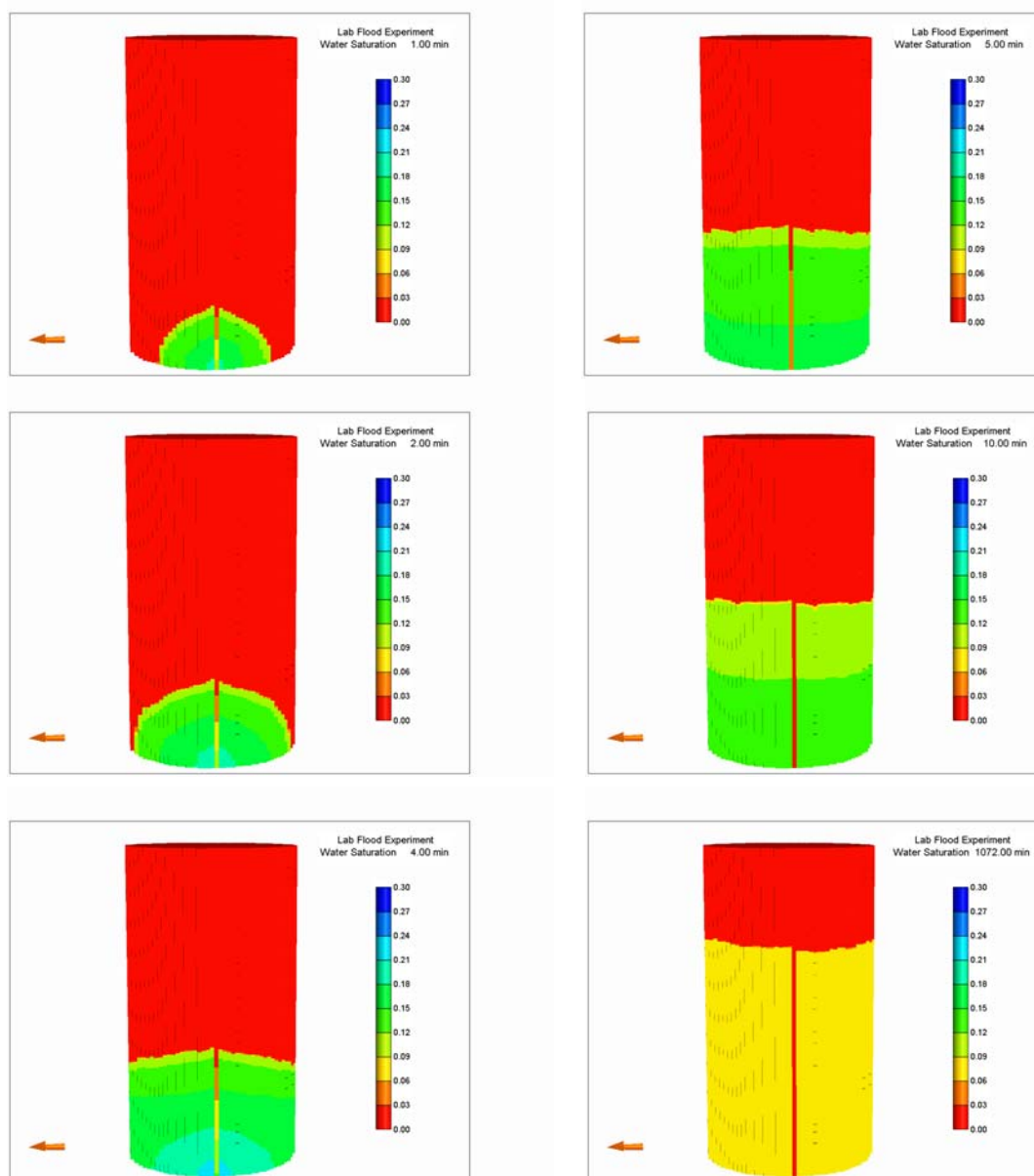


Figure 5-16: 3-D Representations of water saturation distribution for the model developed by using Pc_matrix_3 curve

Similar observations can be made by examining the average water saturation distributions in the fracture as well as in the slice 3 mm above the bottom of the model given in Fig. 5-17 and Fig. 5-18 respectively. The average water saturation in the fracture increases during the injection period (4 min) and decreases after the injection ceased for all cases whereas it decreases by increasing the matrix capillary pressure at a specific time. For instance, the average water saturation in the fracture reaches the maximum value of 10% at the end of injection period for the base case having the smallest matrix capillary pressure whereas 4.8% and 2.5% average water saturation values were observed for the remaining cases in which capillary forces in the matrix become more dominant (Fig. 5-17). In addition, it is perceived from Fig. 5-18 that the average water saturation for the slice 3 mm above the bottom of the model has similar increasing and decreasing tendencies during the injection and after the injection periods respectively. However, no significant difference in average water saturation values was observed between the three cases as compared to the discrepancies in the average water saturation values in the fracture for all cases. For instance, the maximum average water saturation values range from 16% to 18% as moving from the case having the highest matrix capillary pressure to the base case.

Therefore, those observations also show the importance of the proper description of matrix and fracture capillary pressure in the development of capillary imbibition models.

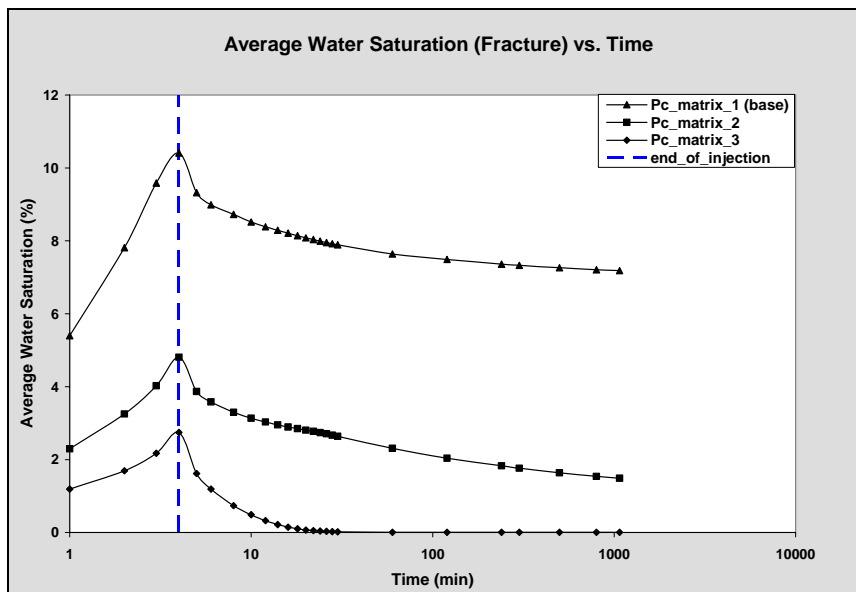


Figure 5-17: Average water saturation in the fracture as a function of time

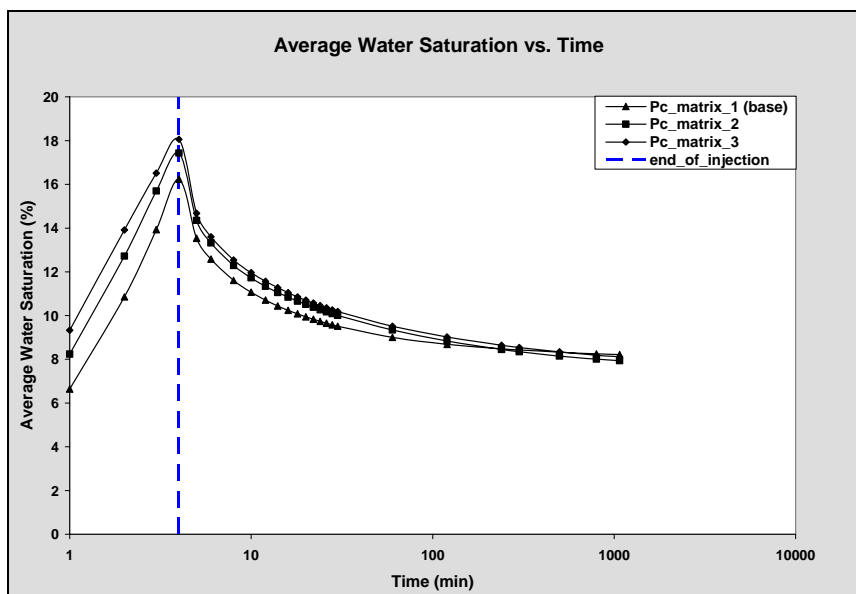


Figure 5-18: Average water saturation in the slice 3 mm above the bottom of the model as a function of time

5.3 Matrix Relative Permeability

In this analysis, three different relative permeability sets for the matrix given in Fig. 5-19 were implemented in the model to investigate the effect of matrix relative permeability on spontaneous imbibition. In addition to the base case, other two relative permeability sets were constructed by increasing and decreasing oil-water relative permeability simultaneously. These additional relative permeabilities were created by selecting different control points in the implementation of B-spline representation. After the implementation of these relative permeability curves in the model, both cases were simulated for 1072 min and the resulting cross-sectional (xy) water saturation distributions of the slice 3 mm above the bottom of the model at six different simulation times are demonstrated in Fig. 5-20 and Fig. 5-21 for these cases respectively.

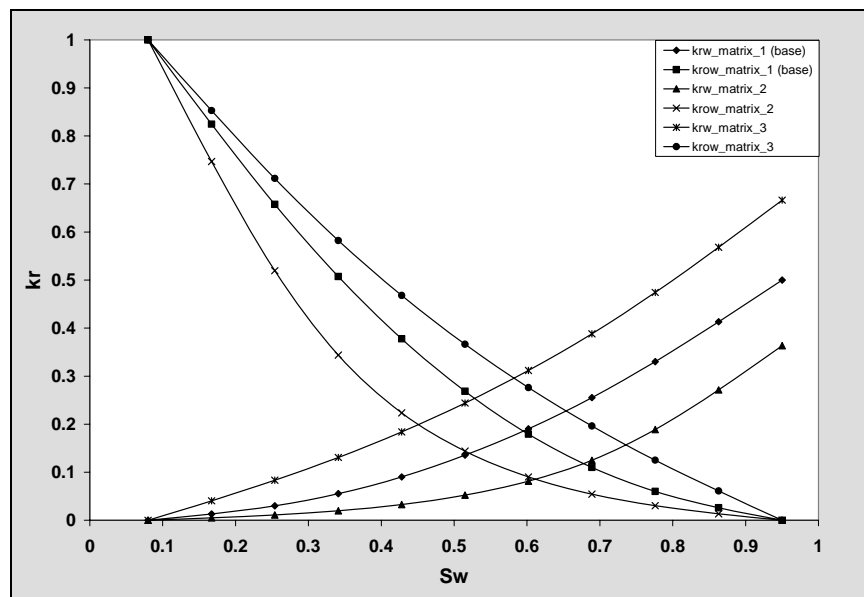


Figure 5-19: Matrix relative permeability vs water saturation

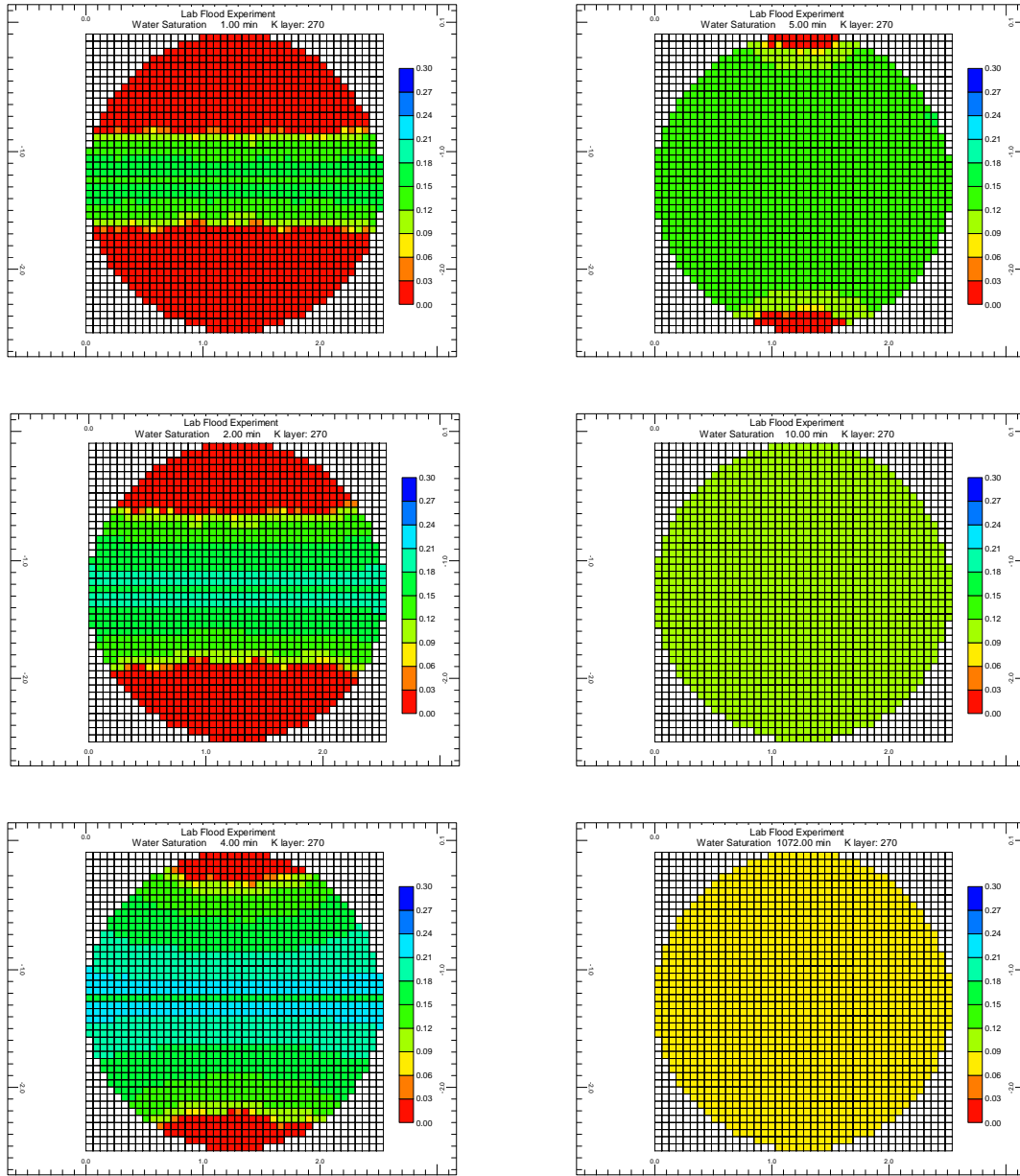


Figure 5-20: Cross-sectional (xy) water saturation distribution of the slice 3 mm above the bottom of the core model with the second sets of relative permeability

Fig. **5-20** demonstrates less areal water propagations in the matrix during the injection period compared to the base case (Fig. **5-10**) and the third case (Fig. **5-21**) since the relative permeability in the matrix is lowered for the second case, which slows down the movement of the water through matrix blocks. As a result of this, higher water saturations at the neighboring blocks of the fracture, which is presented by dark blue color in Fig. **5-20**, are observed for the case with the lowest matrix relative permeabilities. However, the base case has the maximum average saturation value of 16.25% at the end of injection period and the third case having the highest relative permeability values in the matrix reaches the minimum average saturation value of 15.25% for the slice 3 mm above the bottom of the model (Fig. **5-23**). This observation indicates that the effect of relative permeability in the matrix could sometimes be less noticeable when the combination impact of relative permeability and other transport properties come into the picture. On the other hand, the increase in relative permeability values in the matrix as moving from the second case to the base case and thus the third case results in decreasing average water saturation values in the fracture as expected since the water encroachment in the fracture is mainly affected by capillary forces, which does not allow any combination effect of relative permeability and other transport properties (Fig. **5-22**).

Therefore, the impact of relative permeability alteration in the matrix are not as significant as the effect of capillary pressure changes in the matrix. The effect of relative permeabilities could be compensated by the effect of other transport properties as illustrated above, depending on the transport properties selected in the model.

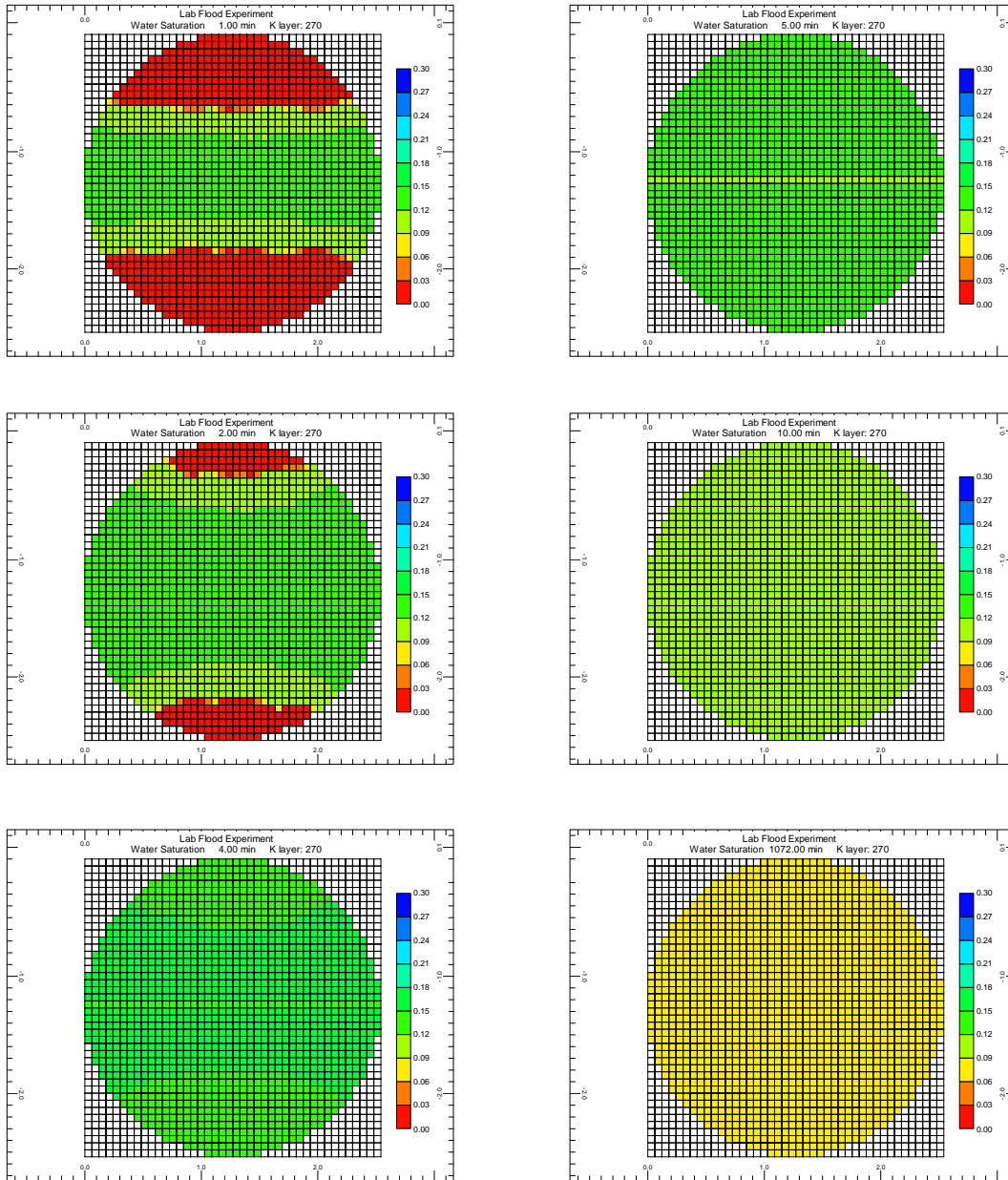


Figure 5-21: Cross-sectional (xy) water saturation distribution of the slice 3 mm above the bottom of the core model with the third sets of relative permeability

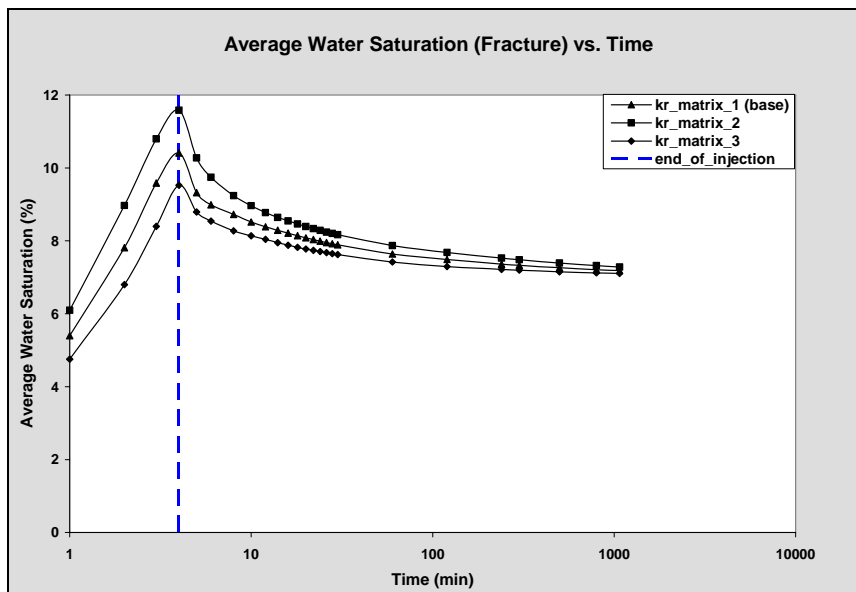


Figure 5-22: Average water saturation in the fracture as a function of time

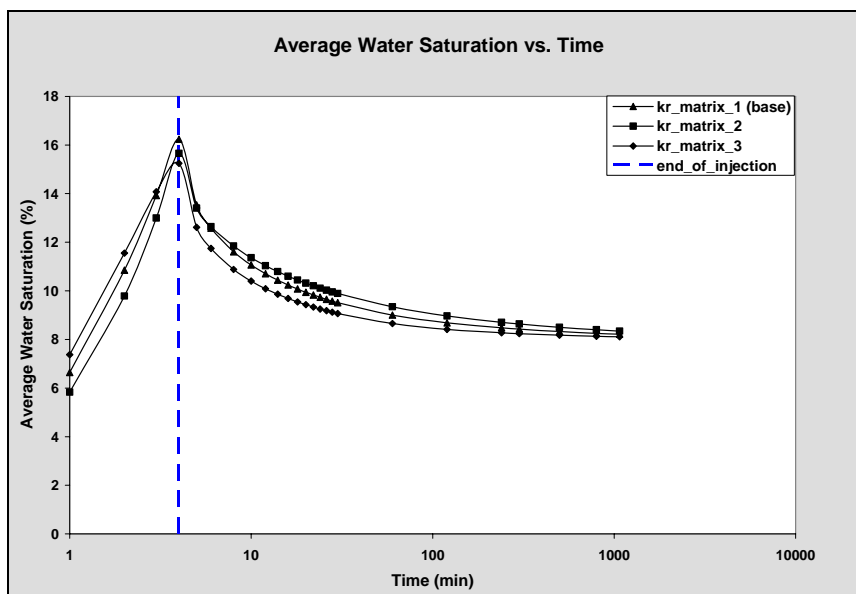


Figure 5-23: Average water saturation in the slice 3 mm above the bottom of the model as a function of time

5.4 Fracture Capillary Pressure

In order to analyze the effect of fracture capillary pressure, three different sets of fracture capillary pressure illustrated in Fig. 5-24 were utilized in the construction of the reservoir model. The first set is described as the base case previously and the remaining two curves were obtained by selecting lower values of CP_{cf} such as 4.8233 and 3.0545 respectively to sustain the fracture capillary pressure less than the matrix capillary pressure. The resulting longitudinal (xz) water saturation distributions are presented at six different simulation times for both cases in Fig. 5-25 and Fig. 5-26 respectively. Corresponding results of the base case are previously presented in Fig. 5-11.

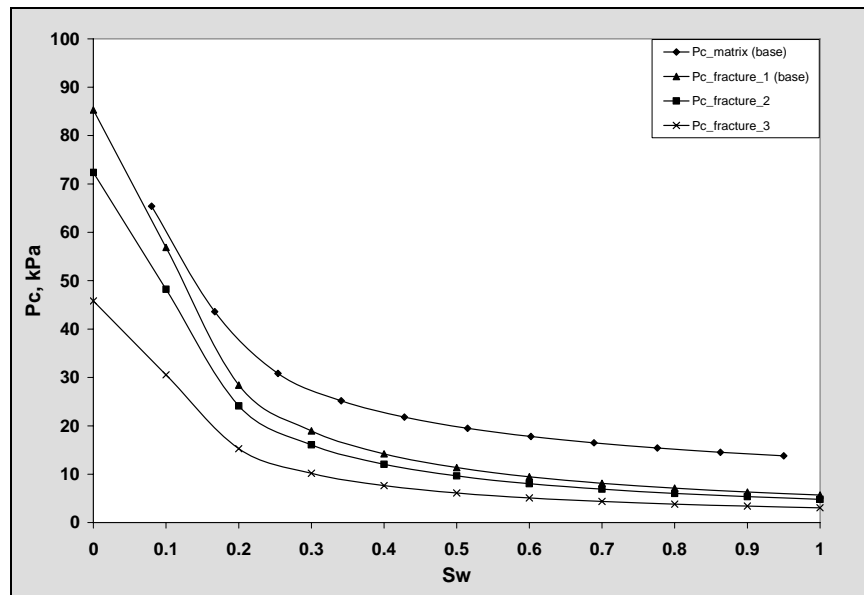


Figure 5-24: Capillary pressure vs water saturation for matrix and fracture

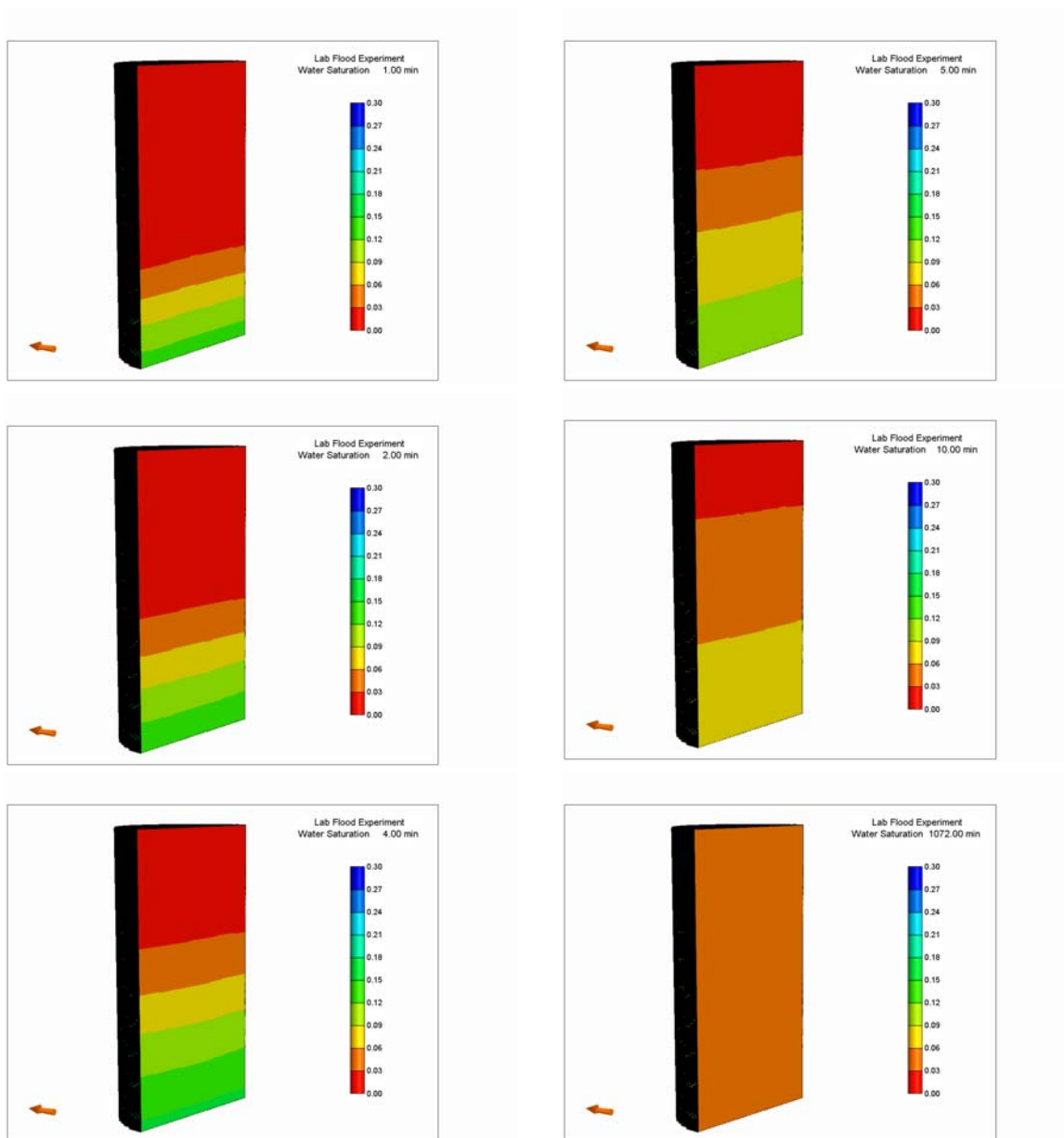


Figure 5-25: Longitudinal (xz) water saturation distribution of the core model developed by using Pc_fracture_2 curve

It can be observed in Figs. **5-11**, **5-25** and **5-26** that fracture capillary pressure is one of the most important parameter affecting the water propagation in the fracture plane as well as the entire core sample. There is a significant water saturation alteration in the fracture plane as fracture capillary pressure changes. Fig. **5-11** demonstrates that water front advances faster in the fracture plane when the fracture capillary pressure increases compared to Figs. **5-25** and **5-26**. For instance, the fracture plane was filled up with water at the end of the injection period (4 min) for the case having the highest fracture capillary pressure values (Fig. **5-11**) whereas less amount of water propagates in the fracture plane at the same time of the simulation for the remaining cases respectively (Figs. **5-25** and **5-26**). In addition to these observations, water saturation stabilizes in the saturation range of 0.03-0.09 at the end of simulation (1072 min) for the first two cases (Figs. **5-11** and **5-25**) unlike the last case with the lowest fracture capillary pressure (Fig. **5-26**) has almost zero water saturations in the fracture plane at the end of simulation which also indicates the necessity of proper fracture capillary pressure definition in the construction of the reservoir model. Similar results can be observed by examining the average water saturation distribution in the fracture as a function of time given in (Fig. **5-27**). The increase in the fracture capillary pressure going from the third case to the base case brings about increasing average water saturation values for the entire simulation times. The maximum average water saturation of 10% was attained at the end of injection period (4 min) in the base case in which the highest fracture capillary pressure was introduced into the model whereas in the third case, the average water saturation peaks at the value of 2% at the end of injection period and approaches to zero values for the rest of the simulation.

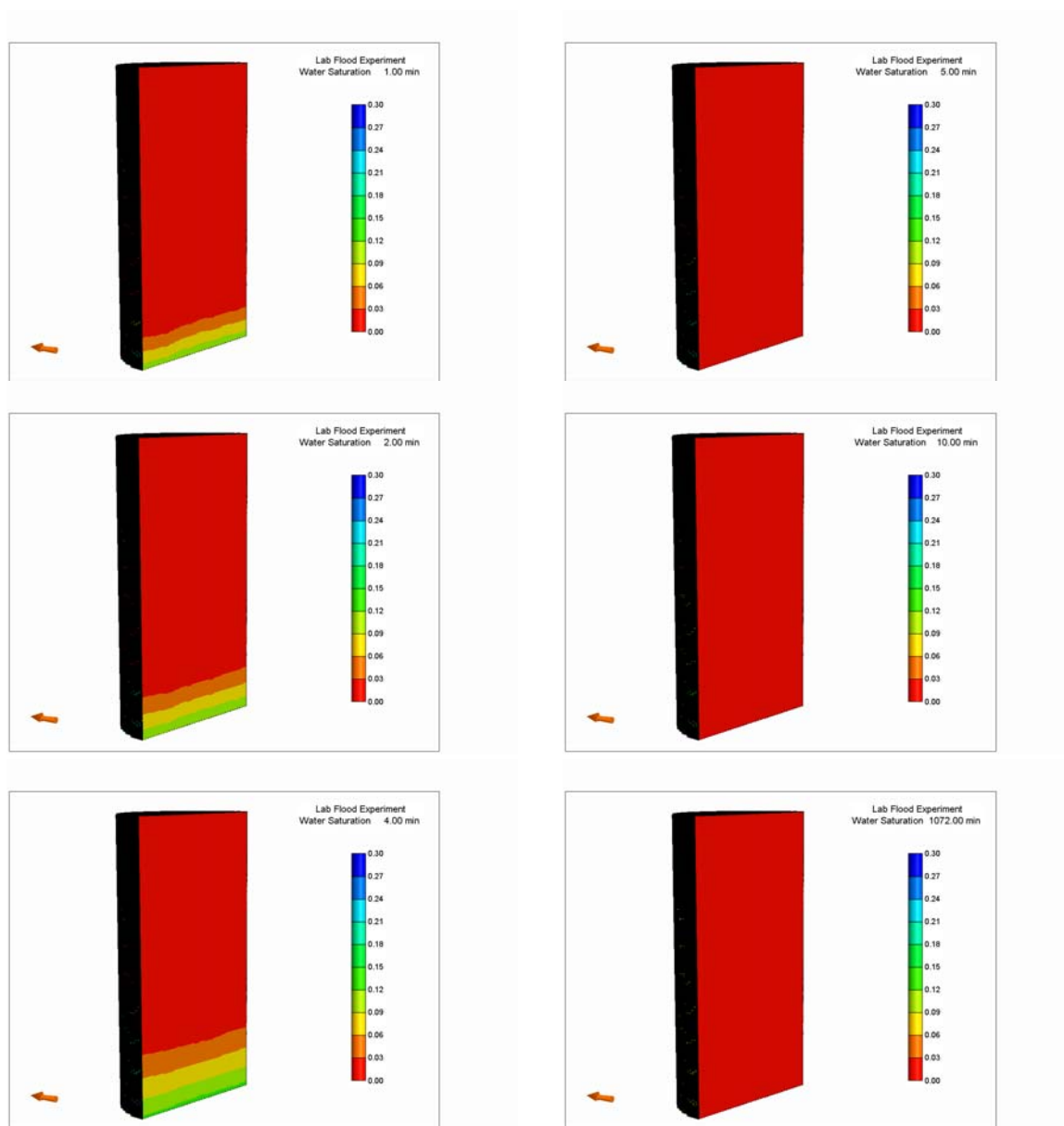


Figure 5-26: Longitudinal (xz) water saturation distribution of the core model developed by using Pc_fracture_3 curve

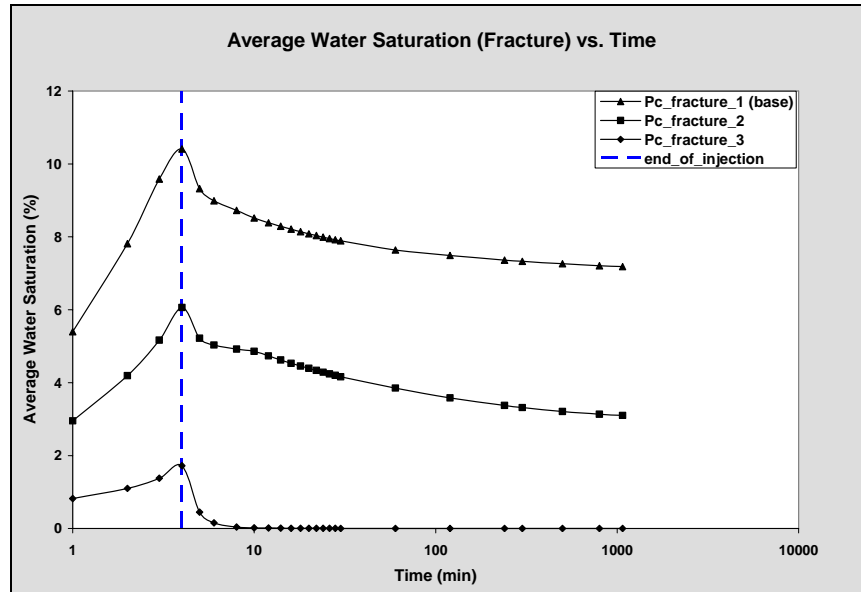


Figure 5-27: Average water saturation in the fracture as a function time

5.5 Fracture Relative Permeability and Capillary Pressure

The effect of straight line relative permeabilities and zero capillary pressure in the fracture on spontaneous capillary imbibition is investigated in this analysis. The average water saturation distribution in the fracture for the base case and the case with zero Pc & straight-line relative permeability in the fracture are demonstrated in Fig. 5-28. It is observed from this figure that zero water saturation was obtained in the fracture plane at each simulation times by implementing zero Pc & straight-line relative permeability for the fracture whereas maximum of 10% water saturation was detected at the end of injection period (4 min) in the base case. Therefore, non-zero Pc & non-straight line relative permeability curves need to be implemented for the fracture in order to attain noticeable water saturation alteration in the fracture, which was also observed by the

experimental study of Karpyn *et al.* (2008). Similarly, the resulting 3-D representations of water saturation distributions given in Fig. 5-29 demonstrate that zero water saturation distribution in the fracture was observed at each time of simulations. All injected water propagated through matrix grid blocks since there is no resistant force such as fracture capillary pressure to compete with matrix capillary pressure, which emphasizes the necessity of non-zero capillary pressure and non-straight line relative permeabilities in the fracture.

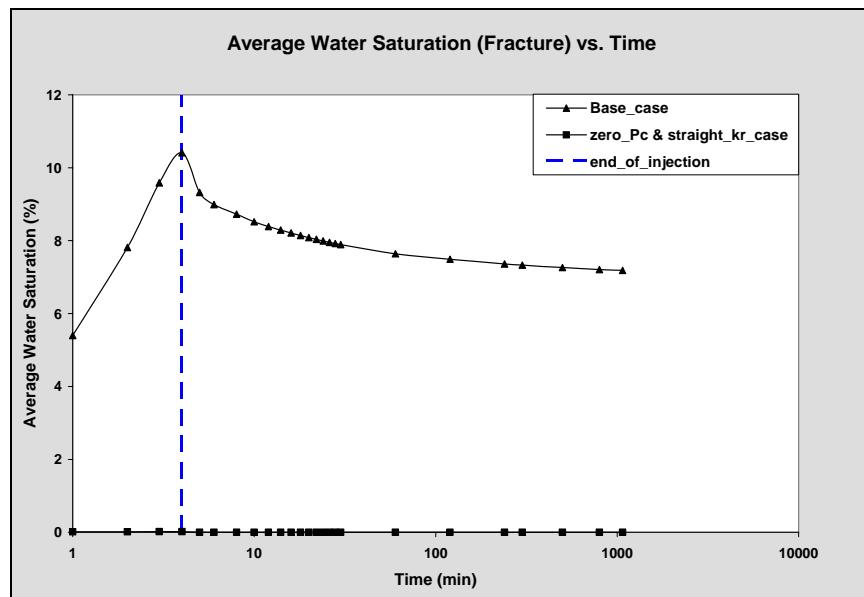


Figure 5-28: Average water saturation in the fracture as a function of time

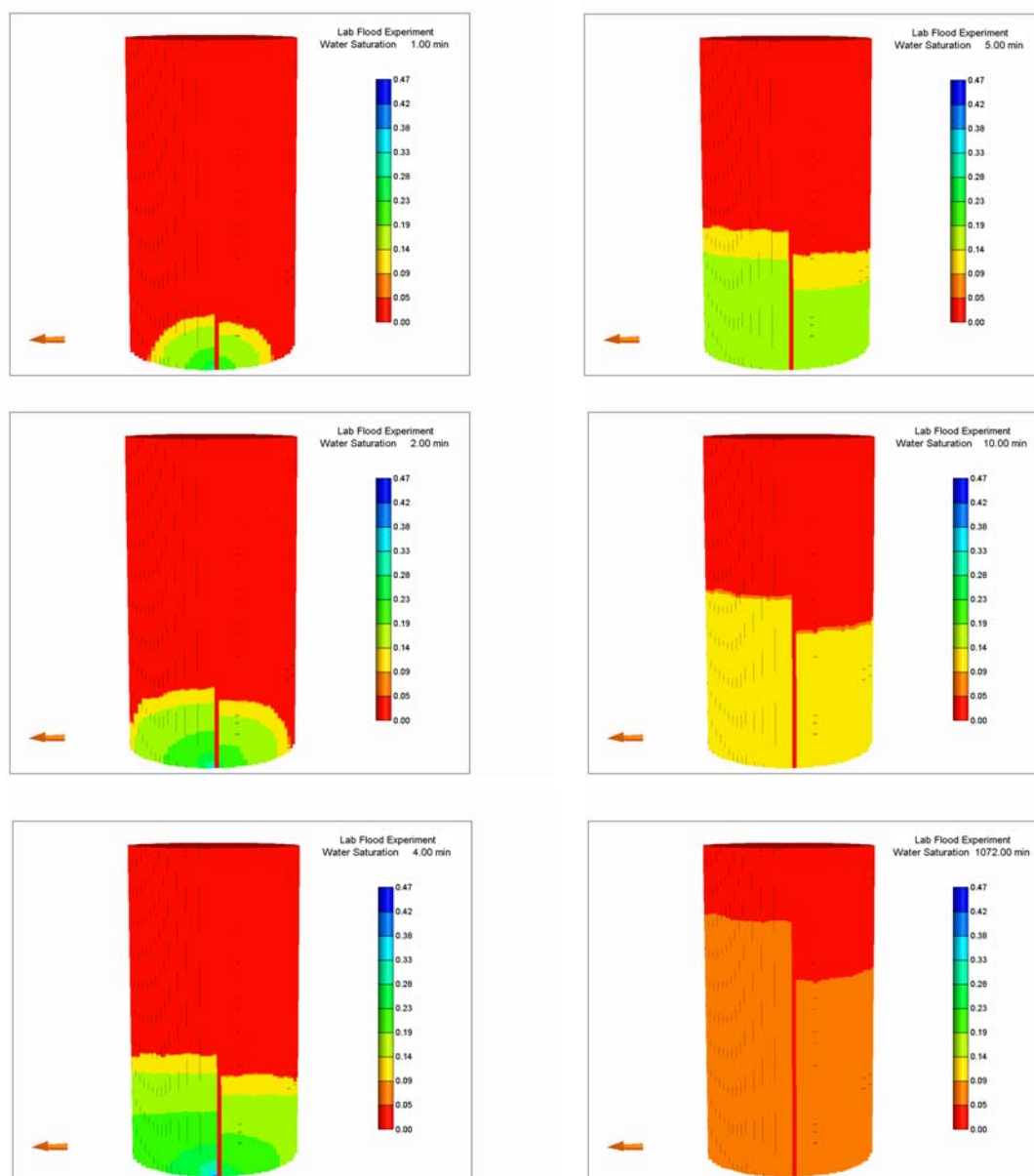


Figure 5-29: 3-D Representations of water saturation distribution for the model with zero P_c & straight-line relative permeability in the fracture

5.6 Fracture Permeability

In this analysis, three different fracture permeability values were implemented in the construction of the model. In addition to the base case having a fracture permeability of 3000 mD, 500 mD and 6000 mD were selected as fracture permeabilities of other two cases in order to examine the effects of fracture permeability on spontaneous imbibition process. The average water saturation in the fracture as a function of time is given in Fig. 5-30. According to this figure, the average water saturation increases by increasing the permeability in the fracture during the injection period (0-4 min). However, the average water saturation values are decreasing for the cases having the fracture permeabilities of 3000 mD and 6000 mD whereas the fracture permeability of 500 mD leads to the increase in the average water saturations after the injection, which contradicts the experimental observations of Karpyn *et al.* (2008). Similar increasing water saturation distribution can also be obtained by examining the advancing water front in Fig. 5-31. After the injection period, especially at 5 min and 10 min, water front progress with an increase water saturation distribution as opposed to the experimental findings. These results can be attributed to the closeness of the fracture permeability of 500 mD to the matrix permeability values with the average permeability value of 100 mD, in which the effect of fracture permeability could be compensated by the impacts of other transport properties. In addition, longitudinal (xz) representations of the reservoir model with the fracture permeability of 6000 mD (Fig. 5-32) indicate that the injected water reaches the top of the reservoir even at the end of 2 min, which gives an opportunity of water production from the reservoir till the end of injection. However, water production from

the model is not desired in this type of study since experimental observations demonstrate no water production from the core sample. Therefore, those observations validates that fracture permeability of 3000 mD could be an appropriate assumption in simulating the spontaneous imbibition experiment previously conducted in Berea sandstone by Karpyn et al. (2008).

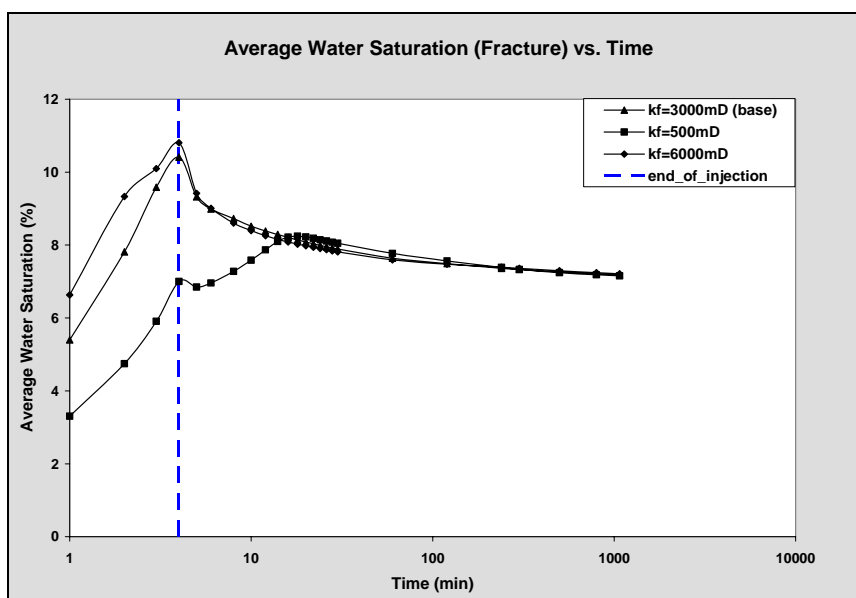


Figure 5-30: Average water saturation in the fracture as a function of time

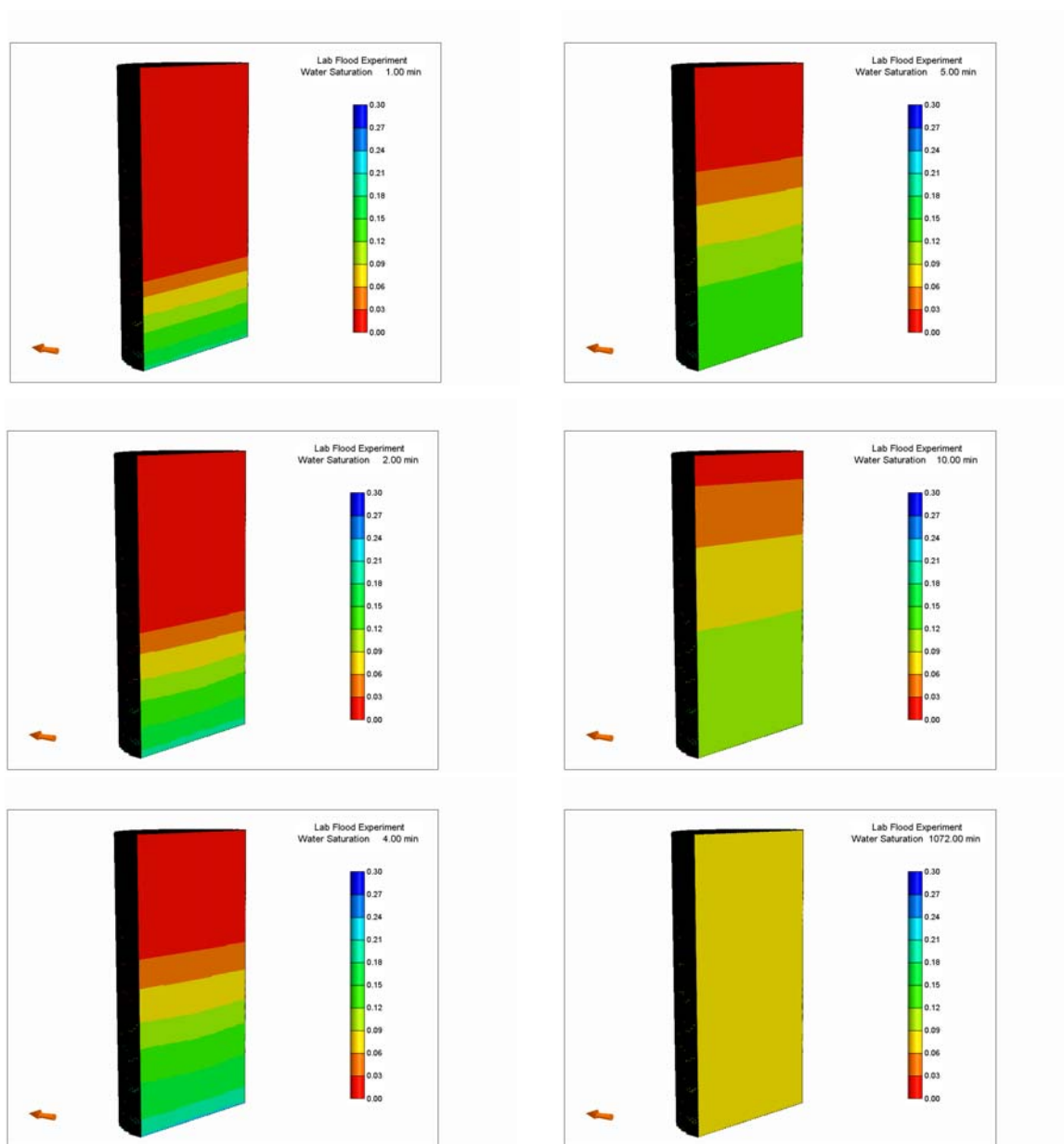


Figure 5-31: Longitudinal (xz) water saturation distribution of the core model with 500 mD of fracture permeability

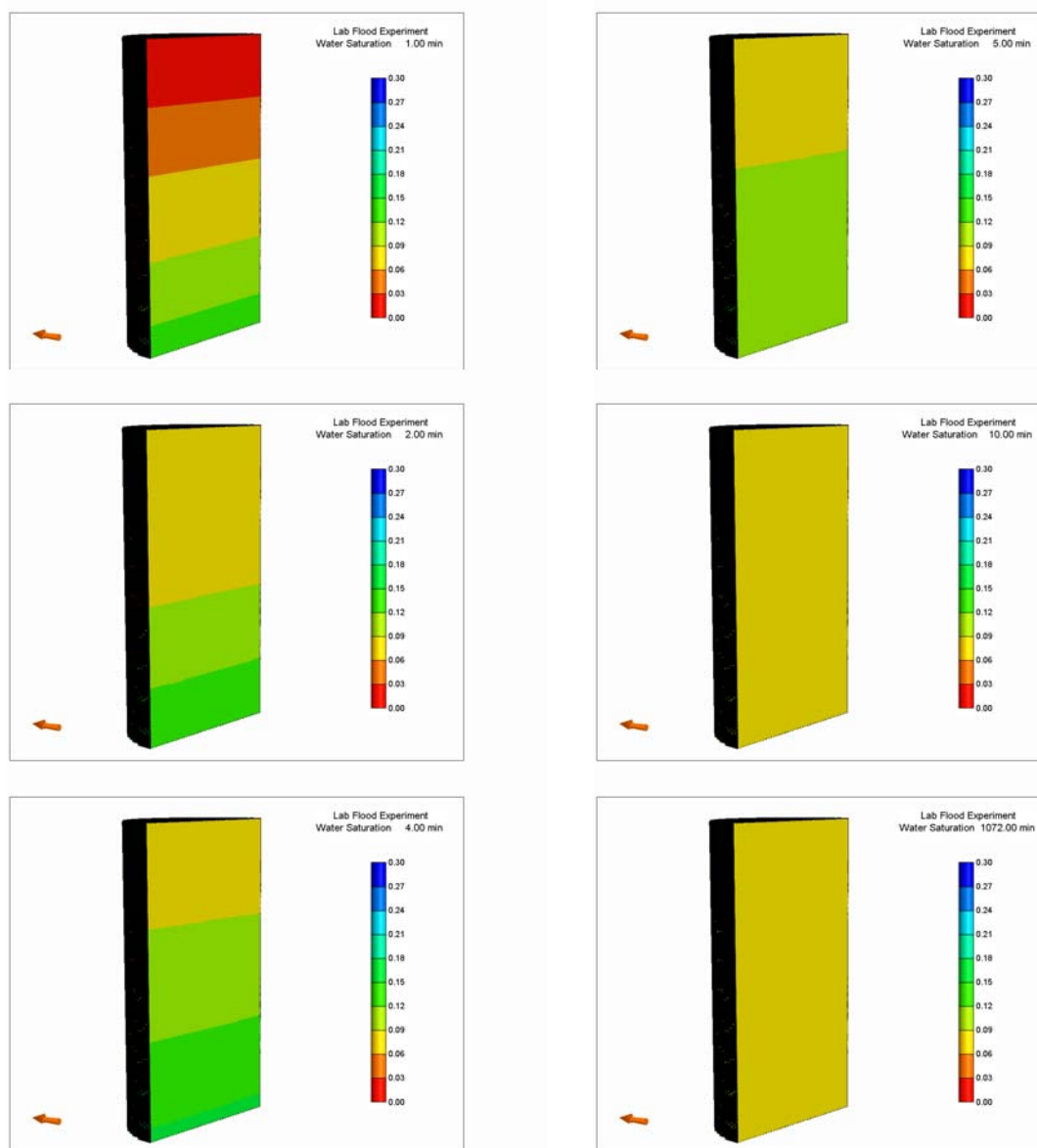


Figure 5-32: Longitudinal (xz) water saturation distribution of the core model with 6000 mD of fracture permeability

5.7 Capillary Hysteresis in the Matrix

The impact of capillary hysteresis in the matrix on water propagation is examined in this section. Drainage and imbibition capillary pressure curves used in this analysis are given in Fig. 5-33. After simulating the model, including capillary hysteresis effect in the matrix for 1072 min, the resulting cross-sectional (xy) water saturation distributions were presented in Fig. 5-34. Those water saturation distributions of the slice 3mm above the bottom of the model demonstrate that water propagates slower than the encroachment of water in the base case (Fig. 5-10) at each simulation times by considering the capillary hysteresis effect in the matrix. For instance, more water saturation alterations, varying between 10% and 13% water saturation, were observed at the simulation time of 5 min for the case with capillary hysteresis (Fig. 5-34) whereas water saturation stabilizes at around the value of 13% water saturation in the base case with no hysteresis (Fig. 5-10). However, the effect of hysteresis is less noticeable for simulation times of 10 min and 1072 min. Because the drainage and imbibition capillary pressure values are getting closer to each other at those small saturation values (0.08-0.1) as presented in Fig. 5-33. These observations indicate that the implementation of capillary hysteresis is essential in the development of reservoir models in order to capture the complex flow mechanisms existing during the spontaneous imbibition processes. Similar conclusions were also presented in the study of Li *et al.* (2005), which emphasizes the significance of capillary hysteresis effect in modeling of counter-current flow experiments.

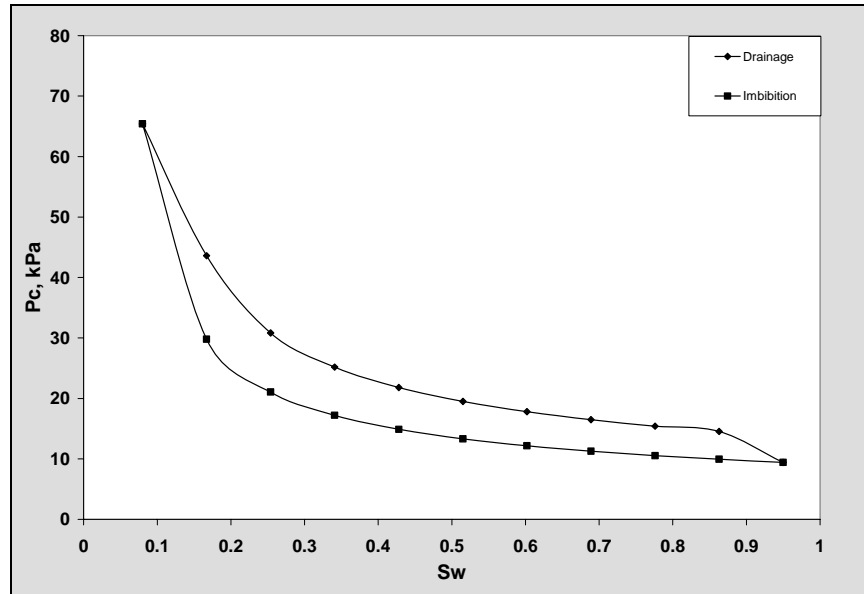


Figure 5-33: Imbibition and drainage capillary pressure curves for matrix

The average water saturation in the slice 3 mm above the bottom of the model and in the fracture as a function of time are given in Fig. 5-35 and Fig. 5-36 respectively. Both figures depict the impact of capillary hysteresis on average water saturations. By introducing the capillary hysteresis in the matrix, the average water saturation in the specified slice peaks at the value of 16% at the end of injection unlike the average water saturation has the maximum value of 14% without hysteresis effect. In addition, higher average water saturations were observed during the spontaneous imbibition period between 4 min and 30 min for the case with capillary hysteresis (Fig. 5-35). This observation is resulted from the effect of capillary hysteresis on spontaneous imbibition process, which provides the opportunity for the model to capture oil-water flow mechanisms during the process encountered in the experiments. Moreover, higher average water saturations were obtained in the fracture for the entire simulation with the

implementation of capillary hysteresis in the matrix (Fig. **5-36**), which shows us that water propagates more in the fracture during the injection period and is imbibed slowly by matrix blocks compared to the base case with no capillary hysteresis effect. This observation also serves us as a validation of the experimental results (Karpyn *et al.*, 2008).

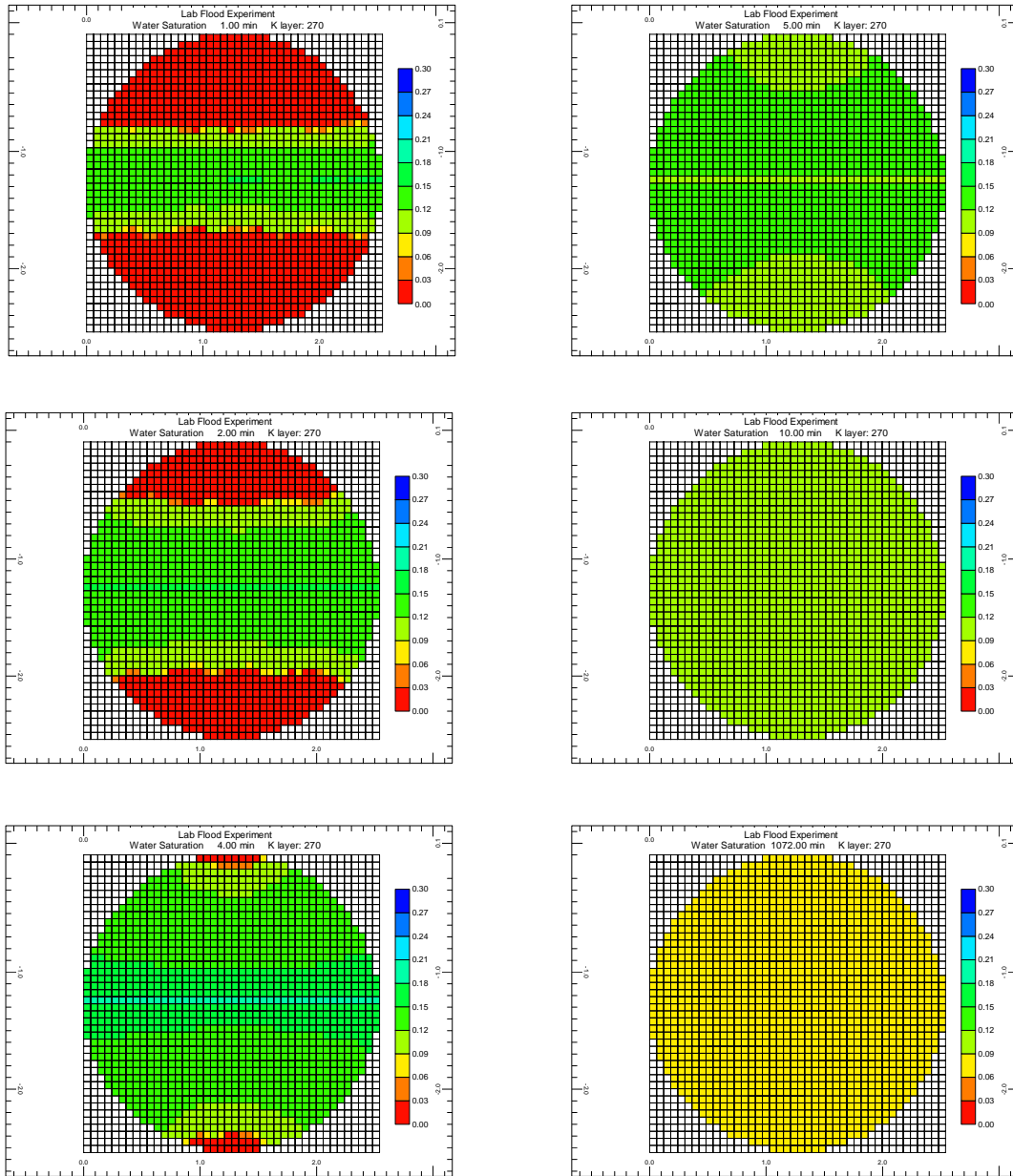


Figure 5-34: Cross-sectional (xy) water saturation distribution of the slice 3 mm above the bottom of the core model with capillary hysteresis effect in the matrix

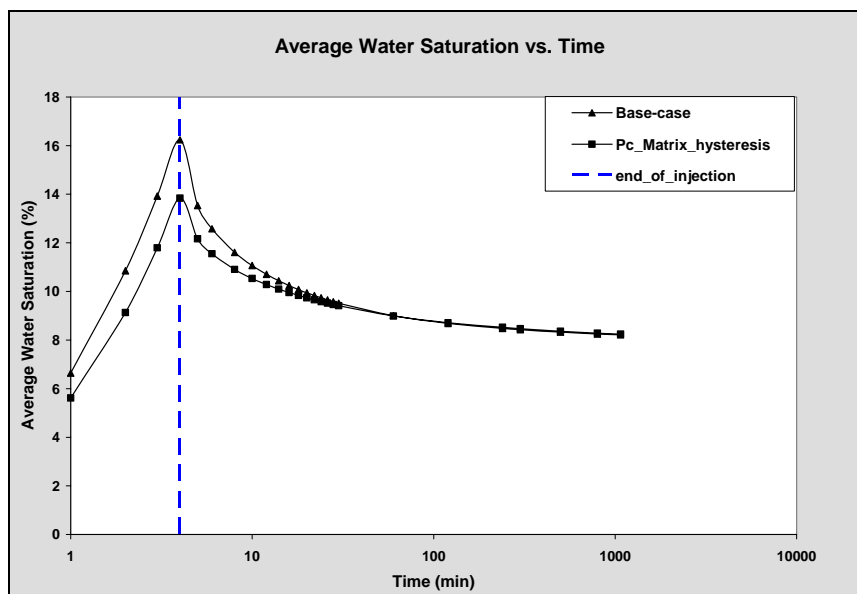


Figure 5-35: Average water saturation in the slice 3 mm above the bottom of the model as a function of time

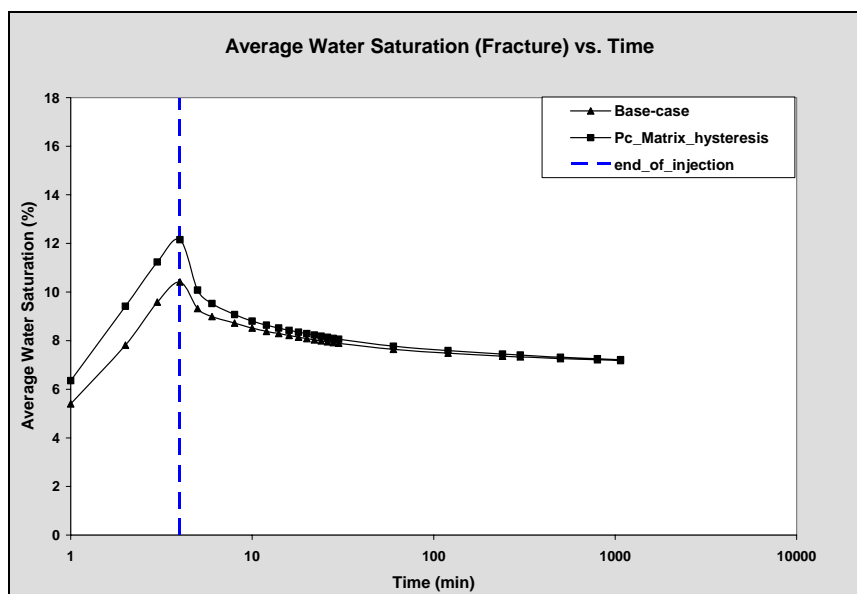


Figure 5-36: Average water saturation in the fracture as a function of time

Chapter 6

Conclusions

Prediction of fluid migration and the characterization of fundamental transport properties in highly heterogeneous systems is a complex problem of great importance in underground flow processes. The efficiency of fluid displacement, hydrocarbon recovery and modeling of spontaneous capillary imbibition processes in naturally fractured rocks requires a complete understanding of flow mechanisms as well as transport properties in porous media. This study provides a mechanistic explanation for spontaneous capillary imbibition in fractured media through experimental and numerical analysis. In addition, the present research allows us to improve ability to predict fluid migration in fractured geologic formations. The automated history matching approach proposed in this study with a powerful optimization protocol also provides a successful implementation and validation tool to construct the relative permeability and capillary pressure curves for matrix and fracture. Using the experimental results obtained from CT scan data and simulation results described in the present work, the following conclusions are made.

- The developed automated history matching protocol can handle the optimization of multiple parameters simultaneously which indicates its power and flexibility. Results of automated history matching confirm the inefficiency of the power-law parameterization in constructing the relative permeability curves with a satisfied monotonicity.

- B-spline parameterizations with a transformation of variables are better representations of relative permeability curves since they ensure monotonicity for relative permeability curves. B-splines with a uniformly distributed control points are also preferable, providing efficient computational algorithm for the construction of relative permeability curve.
- The capillary pressure and gravity forces are the most dominant driving mechanisms affecting the propagation of wetting phase with the displacement of non-wetting-phase in naturally fractured reservoirs. The capillary pressure contrast between the matrix and the fracture controls the fluid distribution in the regions adjoining to fracture plane as well as moving away from the fracture horizontally. On the other hand, gravity forces as a result of saturation gradients determine the cross-flow between layers in the matrix and the fracture.
- Accounting for capillary forces in the fracture is crucial for successful modeling of matrix-fracture flow. The wetting fluid is able to propagate in the fracture under capillary action and then is driven into the rock matrix due to the capillary pressure contrast between the matrix and the fracture. Otherwise, the non-wetting phase could not be effectively displaced by the wetting phase for the purpose of hydrocarbon recovery in naturally fractured reservoirs.
- Three distinctive flow intervals such as early, intermediate and late time identified in the modeling of spontaneous capillary imbibition demonstrate the complexity of flow mechanisms occurring during the displacement of non-wetting phase with the wetting phase in highly heterogeneous porous media. Therefore, the coexistence of co-current and counter-current flow mechanisms during capillary

imbibition in a fractured rock at different time periods requires a proper description of transport properties such as capillary pressure, relative permeability and fracture permeability for modeling purposes.

- Sensitivity analyses indicate that there is a strong correspondence between fluid distribution and fracture structure. The continuity of the fracture has a significant impact on the encroachment of the wetting phase throughout the entire core. The continuous fracture structure enables to fill-up the fracture plane effectively while the propagation of the non-wetting phase is diminished by the existence of disconnection of the fracture blocks using the discontinuous fracture structure.
- The hysteresis effect should be accounted for the construction of capillary pressure and relative permeability curves in order to mimic the capillary imbibition experiments successfully. The complexity of flow mechanisms and the saturation alterations between the wetting and non-wetting phase observed in the experiments can only be captured by the proper implementation of capillary pressure and relative permeability curves with hysteretic components.

References

- Akin, S.: "Estimation of Fracture Relative Permeabilities from Unsteady State Corefloods," *J. Pet. Science. Eng.* (2001) **30**, 1.
- Akin, S., and Demiral, M.R.B.: "Effect of Flow Rate on Imbibition Three-Phase Relative Permeabilities and Capillary Pressures," *Proc.*, SPE Annual Technical Conference and Exhibition, San Antonio, TX (1997) 5-8 October.
- Akin, S., and Kovscek, A.R.: "Imbibition Studies of Low Permeability Porous Media," *Proc.*, SPE Western Regional Meeting, Anchorage, Alaska (1999) 26-27 May.
- Alajmi A.F: "The Influence of a Fracture Tip on Two-Phase Flow Displacement Processes," Ph.D. Dissertation, The Pennsylvania State University, University Park, 2003.
- Al-Lawati, S., and Saleh, S.: "Oil Recovery in Fracture Oil Reservoirs by Low IFT Imbibition Process," paper SPE 36688 presented at the 1996 Annual Technical Conference and Exhibition, Denver, Colorado.
- Al-Wadahi, M., Grader, A.S., and Ertekin, T.: "An Investigation of Three-Phase Countercurrent Flow using X-Ray Computerized Tomography and Neuro-simulation Modeling," *Proc.*, SPE Annual Technical Conference and Exhibition, Dallas, TX (2000) 1-4 October.
- Archer, J.S., and Wong, S.W.: "Use of a Reservoir Simulator to Interpret Laboratory Waterflood Data," *SPEJ* (1973) 343.

- Ayala, H.F.L.: “Compositional Modeling of Naturally-Fractured Gas-Condensate Reservoirs in Multi-Mechanistic Flow Domains,” Ph.D. Dissertation, The Pennsylvania State University, University Park, 2004.
- Baldwin, B.A., and Spinler, E.A: “In-Situ Saturation Development During Spontaneous Imbibition,” *Proceedings*, SCA International Symposium, Golden, CO (1999) Sec. SCA 9922.
- Barenblatt, G.I., Zheltov, I.P., and Kochina, I.N.: “Basic Concepts in the Theory of Seepage of Homogeneous liquids in Fissured Rocks, PMM,” *Sov. Appl. Math. Mech.* (1960) **24**, No.5, 852.
- Behbahani, S.H., Donato, D.G., and Blunt, J.M.: “Simulation of Counter-Current Imbibition in Water-Wet Fractured Reservoirs,” *J. Pet. Science. Eng.* (2006) **50**, 21.
- Bertels, S.P., DiCarlo, D.A., and Blunt, M.J.: “Measurement of Aperture Distribution, Capillary Pressure, Relative Permeability, and in situ Saturation in a Rock Fracture using Computed Tomography Scanning,” *Water Resour. Res.* (2001) **37**, 649.
- Bossie-Codreanu, D., Bia, P. R., and Sabathier, J.: “The Checker Model, an Improvement in Modeling Naturally Fractured Reservoirs with a Tridimensional, Triphasic, Black-Oil Numerical Model,” *SPEJ* (1985) 743.
- Bourblaux, J.B., and Kalaydjian, J.F.: “Experimental Study of Co-current and Countercurrent Flows in Natural Porous Media,” *SPEJ* (1990) 361.
- Brooks, R.H. and Corey, A.T. 1964. Hydraulic Properties of Porous Media. *Hydrology Papers* **3**.

- Chavent, G., Cohen, G., and Espy, M.: "Determination of Relative Permeability and Capillary Pressure by Automatic Adjustment Method," *Proc.*, SPE Annual Technical Conference and Exhibition, Dallas (1980) 21-24 September.
- Chen, Z.-X.: "Some Invariant Solutions of Two-Phase Fluid Displacement Problems Including Capillary Effect," *SPE* (May 1988) 691.
- Chen, Z.-X., Bodvarsson, G.S., and Whitherspoon, P.A.: "An Integral Equation Formulation for Two-Phase Flow and Other Nonlinear Flow Problems through Porous Media," paper 20517 presented at the 1990 SPE Annual Technical Conference and Exhibition, New Orleans, 23-26 September.
- Chen, S., Li, G., Peres, A., and Reynolds, A.C.: "A Well Test for In-situ Determination of Relative Permeability Curves," paper SPE 96414 presented at the 2005 SPE Annual Technical Conference and Exhibition, Dallas, TX, 9-12 October.
- Cil, M., Reis, C.J., Miller, A.M., and Misra, D.: "An Examination of Countercurrent Capillary Imbibition Recovery from Single Matrix Blocks and Recovery Predictions by Analytical Matrix/Fracture Transfer Functions," paper SPE 49005 presented at the 1998 SPE Annual Technical Conference and Exhibition, New Orleans, Louisiana, 27-30 September.
- Clark, S.P., Jr.: "Handbook of Physical Constants," The Geological Society of America, Yale University, New Haven, Conn. (1966).
- Cui, H., and Kelkar, M.: "Automatic History Matching of Naturally Fractured Reservoirs and a Case Study," paper SPE 94037 presented at the 2005 SPE Western Regional Meeting, Irvine, CA, 30 March-1 April.

- Cuiec, L., Bourbiaux, B.J., and Kalaydjian, F.J.: "Oil Recovery by Imbibition in Low-Permeability Chalk," *SPE Form. Eval.* (1994) **9**, 200.
- De la Porte, J.J., Kossack, C.A., and Zimmerman, R.W.: "The effect of Fracture Relative Permeabilities and Capillary Pressures on the Numerical Simulation of Naturally Fractured Reservoirs," paper SPE 95241 presented at the 2005 SPE Annual Technical Conference and Exhibition, Dallas, TX, 9-12 October.
- Du Prey, E.L.: "Gravity and Capillary Effects on Imbibition in Porous Media," *SPEJ* (June 1978) 195.
- Firoozabadi, A., and Hauge, J.: "Capillary Pressure in Fractured Porous Media," *J. Pet. Tech.* (June 1990) 784.
- Firoozabadi, A., and Markeset, T.: "An Experimental Study of Capillary and Gravity Cross-flow in Fractured Porous Media," paper SPE 24918 presented at the 1992 SPE Annual Technical Conference and Exhibition, Washington DC, 4-7 October.
- Firoozabadi, A., and Thomas, L.K.: "Sixth SPE Comparative Solution Project: Dual Porosity Simulators," *J. Pet. Tech.* (1990) 710.
- Fischer, H., Wo, S., and Morrow, R.N.: "Modeling the Effect of Viscosity Ratio on Spontaneous Imbibition," *SPE Res. Eval & Eng.* (June 2008) 577.
- Fung, C.: "Evaluation of the Improved Dual-Porosity Model for the Simulation of Gravity Effects in Naturally Fractured Reservoirs," paper CIM 88-39-05 presented at the 1988 39th Annual Technical Meeting of Petroleum Society of Canadian Institute of Mining, Calgary.

- Gang, W., and Kelkar, M.: "Efficient History Matching in Naturally Fractured Reservoirs," paper SPE 99578 presented at the 2006 SPE/DOE Symposium on Improved Oil Recovery, Tulsa, Oklahoma, 22-26 April.
- Gilman, J.R., and Kazemi, H.: "Improved Calculations for Viscous and Gravity Displacement in Matrix Blocks in Dual-Porosity Simulators," *J. Pet. Tech.* (January 1988) **60**.
- Hamon, G., and Vidal, J.: "Scaling-up the Capillary Imbibition Process from Laboratory Experiments on Homogeneous and Heterogeneous Samples," paper SPE 15852 presented at the 1986 European Petroleum Conference, London, UK.
- Hatiboglu, C.U., and Babadagli, T.: "Experimental Analysis of Primary and Secondary Oil Recovery from Matrix by Counter-Current Diffusion and Spontaneous Imbibition," paper SPE 90312 presented at the 2004 SPE Annual Technical Conference and Exhibition, Houston, Texas, 26-29 September.
- Hill, A.C., and Thomas, G. W.: "A New Approach for Simulating Complex Reservoirs," paper SPE 13537 presented at the 1985 SPE Reservoir Simulation Symposium, Dallas, TX, 10-13 February.
- Hognesen, J.E., Standnes, C.D., and Austad, T.: "Experimental and Numerical Investigation of High Temperature Imbibition into Preferential Oil-Wet chalk," *J. Pet. Sci. Eng.* (2006) **53**, 100.
- Iffly, R., Rousselet, D.C., and Vermeulen, J.L.: "Fundamental Study of Imbibition in Fissured Oil Fields," paper SPE 4102 presented at the 1972 Annual Technical Conference, Dallas, TX.

IMEX, Three-Phase Black Oil Simulator, 2005.13 User's Guide, Computer Modeling Group (CMG), Calgary, 2005.

Kang, Z., Wu, Y.S., Li, J., Wu, Y., Zhang, J., and Wang, G.: "Modeling Multiphase Flow in Naturally Fractured Vuggy Petroleum Reservoirs," paper SPE 102356 presented at the 2006 SPE Annual Technical Conference and Exhibition, San Antonio, TX, 24-27 September.

Karpyn, T. Z., Halleck, M.P., and Grader, S.A.: "A Study of Spontaneous Imbibition in Fractured Sandstone with Contrasting Sedimentary Layers," *J. Pet. Sci. and Eng.* (2008) in press.

Kazemi, H.: "Pressure Transient Analysis of Naturally Fractured Reservoirs with Uniform Fracture Distribution," *SPEJ* (1969) 451, *Trans. AIME* **246**.

Kazemi, H., and Gilman, J.R.: "Multiphase Flow in Fractured Petroleum Reservoirs," *Flow and Contaminant Transport in Fractured Rock*, Bear, J., Tsang, C., and Marsily, G. (ed.), Academic Press Inc., (1993).

Kazemi, H., Merrill, L., Porterfield, K., and Zeman, P.: "Numerical Simulation of Water-Oil Flow in Naturally Fractured Reservoirs," *SPEJ* (December 1976) 317.

Kazemi, H., Merrill, L.S.: "Numerical Simulation of Water Imbibition in Fractured Cores," *SPEJ* (1979) 323.

Kerig, P.D., and Watson, A.T.: "A New Algorithm for Estimating Relative Permeabilities from the Displacement Experiments," *SPERE* (1987), 103.

Kleppe, J., and Morse, R.A.: "Oil Production from Fractured Reservoirs by Water Displacement," paper SPE 5084 presented at the 1974 SPE Annual Technical Conference and Exhibition, Houston, Texas, 6-9 October.

- Kruger, W.D.: "Determining Areal Permeability Distribution by Calculations," *J. Pet. Tech.* (1961) 691.
- Lee, J., and Kang, J.M.: "Oil Recovery in a Fracture of Variable aperture with Countercurrent Imbibition: Experimental Analysis," paper SPE 56416 presented at the 1999 SPE Annual Technical Conference and Exhibition, Houston, Texas, 3-6 October.
- Li, G.: "History Dependent Modeling of Countercurrent Flow in Porous Media," Ph.D. Dissertation, The Pennsylvania State University, University Park, 2003.
- Li, G., Karpyn, T.Z., Halleck, M.P., and Grader, S.A.: "Numerical Simulation of a CT-Scanned Counter-Current Flow Experiment," *Transport in Porous Media* (2005) **60**, 225.
- Marle, C.M.: *Multiphase Flow in Porous Media*, Gulf Publishing Company, Editions Technip, Paris (1981).
- MATLAB 7.3.0, release 2006b tutorial, The Math Works, Inc., Natick, MA, 2006.
- Mattax, C.C., and Kyte, J.R.: "Imbibition Oil Recovery from Fractured Water Drive Reservoirs," *SPEJ* (June 1962) 177.
- McWhorter, D.B. and Sunada, K.D.: "Exact Integral Solution for Two-Phase Flow," *Water Resour. Res.* (1990) **26**, 339.
- Morrow, R.N., Mason, G.: "Recovery of Oil by Spontaneous Imbibition," *Curr. Opin. Coll. Inter. Sci.* (2001) **6**, No. 3, 321.
- Pankaj, S.G., and Kishore, K.M.: "Matrix-Fracture Transfer through Countercurrent Imbibition in Presence of Fracture Fluid Flow," *Transport in Porous Media* (2004) **55**, 309.

- Parson, R.W., and Chaney, P.R.: "Imbibition Model Studies on Water-Wet Carbonate Rocks," *SPEJ* (March 1966) 26.
- Pieters, D.A., and Graves, R.M.: "Fracture Relative Permeability: Linear or Non-linear Function?," paper SPE 28701 presented at the 1994 International Petroleum Conference and Exhibition of Mexico, Veracruz, Mexico, 10-13 October.
- Pooladi-Darvish, M., and Firoozabadi, A.: "Experiments and Modeling of Water Injection in Water-Wet Fractured Porous Media," *J. Can. Pet. Tech.* (2000) **39**, No.3, 31.
- Pooladi-Darvish, M., and Firoozabadi, A.: "Co-Current and Counter-Current Imbibition in a Water-Wet Matrix Block," *SPEJ* (2000) **5**, No.1, 3.
- Pruess, K., and Narasimhan, T.N.: "A Practical Method for Modeling Fluid and Heat Flow in Fractured Porous Media," *SPEJ* (1985) 25.
- Quandalle, P., and Sabathier, J. C.: "Typical Features of a Multipurpose Reservoir Simulator," *SPE Res. Eng. J.* (November 1989) 475.
- Rangel-German, E., Akin, S., and Castanier, L.M.: "Experimental and Theoretical Investigation of Multiphase Flow in Fractured Media," paper presented at the 1998 Geothermal Resources Council Annual Meeting, San Diego, CA, 20-23 September.
- Rangel-German, E.R., and Kavscek, A.R.: "Matrix-Fracture Shape Factors and Multiphase-Flow Properties of Fractured Porous Media," paper SPE 95105 presented at the 2005 SPE Latin American and Caribbean Petroleum Engineering Conference, Rio de Janeiro, Brazil, 20-23 June.
- Romm, E.S.: "Fluid Flow in Fractured Rocks," Nedra Publisher, Moscow (1966).

- Rossen, W.R., and Kumar, A.T.A.: "Single and Two-Phase Flow in Naturally Fractures," paper SPE 24915 presented at the 1992 SPE Annual Technical Conference and Exhibition, Washington, D.C., 4-7 October.
- Ruth, W.D., Li, Y., Mason, G., and Morrow, R.N.: "An Approximate Analytical Solution for Counter-Current Spontaneous Imbibition," (2007) **66**, 373.
- Salomon, D.: "Computer Graphics and Geometric Modeling," Springer, Verlag, New York, Inc., New York (1999).
- Schechter, D.S., Zhou, D., and Orr Jr., F.M.: "Low IFT Drainage and Imbibition," *J. Pet. Sci. Eng.* (1994) **11**, 283.
- Standness, C.D.: "Spontaneous Imbibition of Water into Cylindrical Cores with High Aspect Ratio: Numerical and Experimental Results," *J. Pet. Sci. Eng.* (2006) **50**, 151.
- Tavassoli, Z., Zimmerman, R.W., and Blunt, M.J.: "Analysis Counter-Current Imbibition with Gravity in Weakly Water-Wet Systems," *J. Pet. Science. Eng.* (2005) **48**, No.1-2, 94.
- Tavassoli, Z., Zimmerman, R.W., and Blunt, M.J.: "Analytic Analysis for Oil Recovery During Counter-Current Imbibition in Strongly Water-Wet Systems," *Transport in Porous Media* (2005) **58**, 173.
- Thomas, L., Pierson, R., and Dixon, T.: "Fractured Reservoir Simulation," *SPEJ* (February 1983) 42.
- Timur, A.: "An Investigation of Permeability, Porosity, and Residual Water Saturation Relationship for Sandstone Reservoirs," *The Log Analyst* (1968) **9**, No. 4, 8.

Warren, J.E., and Root, P.J.: "The Behavior of Naturally Fractured Reservoirs," *SPEJ* (September 1963) 245, *Trans. AIME* **228**.

Zhang, X., Morrow, N.R., and Ma, S.: "Experimental Verification of a Modified Scaling Group for Spontaneous Imbibition," *SPE Res. Eng. J.* (1996) **11**, 280.

Zhou, D. and Stenby, E.H.: "Immiscible Displacement in a Porous Medium Simulated by a Statistical Model," *North Sea Oil and Gas Reservoirs-II*, Buller et al. (ed.), Graham and Tortman, London, UK, (1989) 271-280.

Appendix A

Representation of Relative Permeability to Oil

A.1 Quadratic B-Spline Representation

- **1th interval:** $0 \leq S_w \leq 0.1$

$$S_{wt}(t) = \frac{1}{2}(t^2 - 2t + 1)CS_{w-1} + \frac{1}{2}(-2t^2 + 2t + 1)CS_{w0} + \frac{1}{2}(t^2)CS_{w0}$$

$$kr_i(t) = \frac{1}{2}(t^2 - 2t + 1)Ckr_{o-1} + \frac{1}{2}(-2t^2 + 2t + 1)Ckr_{o0} + \frac{1}{2}(t^2)Ckr_{o0}$$

- **2nd interval:** $0.1 < S_w \leq 0.5$

$$S_{wt}(t) = \frac{1}{2}(t^2 - 2t + 1)CS_{w0} + \frac{1}{2}(-2t^2 + 2t + 1)CS_{w1} + \frac{1}{2}(t^2)CS_{w2}$$

$$kr_i(t) = \frac{1}{2}(t^2 - 2t + 1)Ckr_{o0} + \frac{1}{2}(-2t^2 + 2t + 1)Ckr_{o1} + \frac{1}{2}(t^2)Ckr_{o2}$$

- **3rd interval:** $0.5 < S_w \leq 0.8$

$$S_{wt}(t) = \frac{1}{2}(t^2 - 2t + 1)CS_{w1} + \frac{1}{2}(-2t^2 + 2t + 1)CS_{w2} + \frac{1}{2}(t^2)CS_{w3}$$

$$kr_i(t) = \frac{1}{2}(t^2 - 2t + 1)Ckr_{o1} + \frac{1}{2}(-2t^2 + 2t + 1)Ckr_{o2} + \frac{1}{2}(t^2)Ckr_{o3}$$

- **4th interval:** $0.8 < S_w \leq 1.0$

$$S_{wt}(t) = \frac{1}{2}(t^2 - 2t + 1)CS_{w2} + \frac{1}{2}(-2t^2 + 2t + 1)CS_{w3} + \frac{1}{2}(t^2)CS_{w4}$$

$$kr_i(t) = \frac{1}{2}(t^2 - 2t + 1)Ckr_{o2} + \frac{1}{2}(-2t^2 + 2t + 1)Ckr_{o3} + \frac{1}{2}(t^2)Ckr_{o4}$$

A.2 Cubic B-Spline Representation

- **1th interval:** $0 \leq S_w \leq 0.25$

$$S_{wi}(t) = \frac{1}{6}(-t^3 + 3t^2 - 3t + 1)CS_{w-1} + \frac{1}{6}(3t^3 - 6t^2 + 4)CS_{w0} +$$

$$\frac{1}{6}(-3t^3 + 3t^2 + 3t + 1)CS_{w1} + \frac{1}{6}(t^3)CS_{w2}$$

$$kr_i(t) = \frac{1}{6}(-t^3 + 3t^2 - 3t + 1)Ckr_{o-1} + \frac{1}{6}(3t^3 - 6t^2 + 4)Ckr_{o0} +$$

$$\frac{1}{6}(-3t^3 + 3t^2 + 3t + 1)Ckr_{o1} + \frac{1}{6}(t^3)Ckr_{o2}$$

- **2nd interval:** $0.25 < S_w \leq 0.5$

$$S_{wi}(t) = \frac{1}{6}(-t^3 + 3t^2 - 3t + 1)CS_{w0} + \frac{1}{6}(3t^3 - 6t^2 + 4)CS_{w1} +$$

$$\frac{1}{6}(-3t^3 + 3t^2 + 3t + 1)CS_{w2} + \frac{1}{6}(t^3)CS_{w3}$$

$$kr_i(t) = \frac{1}{6}(-t^3 + 3t^2 - 3t + 1)Ckr_{o0} + \frac{1}{6}(3t^3 - 6t^2 + 4)Ckr_{o1} +$$

$$\frac{1}{6}(-3t^3 + 3t^2 + 3t + 1)Ckr_{o2} + \frac{1}{6}(t^3)Ckr_{o3}$$

- **3rd interval:** $0.5 < S_w \leq 0.75$

$$S_{wi}(t) = \frac{1}{6}(-t^3 + 3t^2 - 3t + 1)CS_{w1} + \frac{1}{6}(3t^3 - 6t^2 + 4)CS_{w2} +$$

$$\frac{1}{6}(-3t^3 + 3t^2 + 3t + 1)CS_{w3} + \frac{1}{6}(t^3)CS_{w4}$$

$$kr_i(t) = \frac{1}{6}(-t^3 + 3t^2 - 3t + 1)Ckr_{o1} + \frac{1}{6}(3t^3 - 6t^2 + 4)Ckr_{o2} +$$

$$\frac{1}{6}(-3t^3 + 3t^2 + 3t + 1)Ckr_{o3} + \frac{1}{6}(t^3)Ckr_{o4}$$

- **4th interval:** $0.75 < S_w \leq 1.0$

$$S_{wi}(t) = \frac{1}{6}(-t^3 + 3t^2 - 3t + 1)CS_{w2} + \frac{1}{6}(3t^3 - 6t^2 + 4)CS_{w3} +$$

$$\frac{1}{6}(-3t^3 + 3t^2 + 3t + 1)CS_{w4} + \frac{1}{6}(t^3)CS_{w5}$$

$$kr_i(t) = \frac{1}{6}(-t^3 + 3t^2 - 3t + 1)Ckr_{o2} + \frac{1}{6}(3t^3 - 6t^2 + 4)Ckr_{o3} +$$

$$\frac{1}{6}(-3t^3 + 3t^2 + 3t + 1)Ckr_{o4} + \frac{1}{6}(t^3)Ckr_{o5}$$

Appendix B

Sample Matlab and C++ Source Codes for Preparation of the Simulation Model

B.1 Subtraction of Dry and Oil-Wet CT Scan Data

```
clear all
clc

%===== UPLOADING DRY AND OIL-WET CT SCAN DATA =====

for ifile=1:29;

    cd CT_dry\w_50_slices;

    sprintf('Slice Number: %d',ifile);

    t=num2str(ifile);

    if (ifile<10)

        Datafile_dry=strcat('basar_data_00',t);

    elseif (ifile<100)

        Datafile_dry=strcat('basar_data_0',t);

    else

        Datafile_dry=strcat('basar_data_',t);

    end

    A_dry=dlmread(Datafile_dry);

    [a,b] = size(A_dry); % a and b are the sizes of the matrix

    cd ../
    cd ../
    cd CT_oil
```



```

if (ifile<10)

    Datafile_oil=strcat('basar_oil_00',t);

elseif (ifile<100)

    Datafile_oil=strcat('basar_oil_0',t);

else

    Datafile_oil=strcat('basar_oil_',t);

end

A_oil=dlmread(Datafile_oil);

if (ifile==29);
    slice = 41;
else
    slice = 50;
end

%===== ARRANGING RAW DATA FROM (23X9+4) TO BE 211 ROWS =====

lcount = 1;
brow = 1;
xdim = 211;
ydim = 211;

for row = 1 : a

    for col = 1 : b

        if (lcount == 24)&(col==4)

            Amap_dry( brow, (lcount - 1)*9 + col ) = A_dry( row, col );
            Amap_oil( brow, (lcount - 1)*9 + col ) = A_oil( row, col );
            lcount=0;
            brow=brow+1;
            break

        else

            Amap_dry( brow, (lcount - 1)*9 + col ) = A_dry( row, col );
            Amap_oil( brow, (lcount - 1)*9 + col ) = A_oil( row, col );

        end

    end

    lcount=lcount+1;
end

```

```
%==REARRANGING THE MATRIX TO BE 3-D AND IDENTIFICATION OF FRACTURE ==
```

```

jk=0;
for k = 1 : slice;

    for i = 1 : xdim;

        for j = 1 : ydim;

            B_dry(j,i,k)=Amap_dry(j+(jk*ydim),i);
            B_oil(j,i,k)=Amap_oil(j+(jk*ydim),i);

            if (B_dry(j,i,k)==0);
                B_dry(j,i,k)=10;
            end
            if ((j>86)&&(j<113));
                if (B_dry(j,i,k)<=2800); %CT THRESHOLD
                    B_dry(j,i,k)=10;
                end
            end
            if (B_dry(j,i,k)==10);
                B_oil(j,i,k)=0;
            end
        end
    end
    jk=jk+1;
end

sum_dry = 0;
sum_oil = 0;
count_dry = 0;
count_oil = 0;

%===== AVERAGING DRY AND OIL-WET CT SCAN DATA =====

for k = 1 : slice;

    for i = 1 : xdim;

        for j = 1 : ydim;

            if (B_dry(j,i,k)~=10);
                sum_dry = sum_dry + B_dry(j,i,k);
                count_dry = count_dry + 1;
            end
            if (B_oil(j,i,k)~=0);
                sum_oil = sum_oil + B_oil(j,i,k);
                count_oil = count_oil + 1;
            end
        end
    end
end
end

```

```

ave_dry = sum_dry/count_dry;
ave_oil = sum_oil/count_oil;
delta_ave_CT = ave_oil - ave_dry;
diff=B_oil-B_dry;

cd ../;

%===== WRITING THE SUBTRACTED MATRIX INTO A FILE =====

t=num2str(ifile);
if (ifile<10);
filename = ['subtracted_00' t '.mat'];
elseif (ifile<100);
filename = ['subtracted_0' t '.mat'];
else
filename = ['subtracted_' t '.mat'];
end

save (filename);

clear all
end

```

B.2 Up-Scaling the Subtracted Data

```

clear all
clc

%==== UPLOADING THE SUBTRACTED DATA AND DEFINING UP-SCALING SCHEME ====

for ifile=1:29;

    zeros=0;
    x_upsfactor=5;
    y_upsfactor=5;
    z_upsfactor=5;
    nrpixels=0;
    scnrpixels=0;

    sprintf('Slice Number: %d',ifile);

    t=num2str(ifile);

    if (ifile<10)

        Datafile=strcat('subtracted_00',t, '.mat');

    elseif (ifile<100)

        Datafile=strcat('subtracted_0',t, '.mat');

    else

        Datafile=strcat('subtracted_',t, '.mat');

    end

    load(Datafile);

    if (ifile~=29);

        for k = 1 : slice;

            for i = 1 : xdim-1;

                for j = 1 : ydim-1;

                    diff_up(j,i,k)=diff(j+1,i+1,k);

                end

            end

        end
    end
end

```

```

end

%===== CALCULATING THE NUMBER OF ROCK PIXELS =====

for k = 1 : slice;

    for i = 1 : xdim-1;

        for j = 1 : ydim-1;

            if ((diff_up(j,i,k)<0)&&(diff_up(j,i,k)~=-10));
                diff_up(j,i,k)=0;
            end
            if (diff_up(j,i,k)~=-10);
                nrpixels = nrpixels + 1;
            end
        end
    end
end

%===== MASS BALANCE CHECK AND UP-SCALING =====

i5=0;
j5=0;
k5=0;
sum=0;
icount=0;

fid= fopen('mass_check.txt','w');
for k = 1 : (slice/z_upsfactor);

    k1=k5+1;
    k2=k1+1;
    k3=k2+1;
    k4=k3+1;
    k5=k4+1;
    for i = 1 : (xdim-1)/x_upsfactor;

        i1=i5+1;
        i2=i1+1;
        i3=i2+1;
        i4=i3+1;
        i5=i4+1;

        for j = 1: (ydim-1)/y_upsfactor;

            j1=j5+1;
            j2=j1+1;
            j3=j2+1;
            j4=j3+1;

```

```

        j5=j4+1;

    for kk=k1:k5;
        for ii=i1:i5;
            for jj=j1:j5;

                if (diff_up(jj,ii,kk)==-10);
                    zeros=zeros+1;
                else
                    sum = sum + diff_up(jj,ii,kk);
                    icount=icount+1;
                end

            end

        end
    end

%===== CALCULATING THE NUMBER OF UP-SCALED ROCK PIXELS =====

    if (zeros <= (x_upsfactor*y_upsfactor*z_upsfactor*0.4));
        UB{ifile}(j,i,k)=sum /icount;
        scnrpixels=scnrpixels+1;
    elseif (zeros >= (x_upsfactor*y_upsfactor*z_upsfactor*0.6));
        UB{ifile}(j,i,k)=0;
    else
        UB{ifile}(j,i,k)=-1;
        ave=sum/icount;
        fprintf(fid,'%d %d %d %d %f\n', j, i, k, zeros, ave);
    end
    zeros=0;
    sum=0;
    icount=0;

end
j5=0;
end
i5=0;
end

else

    for k = 1 : slice-1;

        for i = 1 : xdim-1;

            for j = 1 : ydim-1;

                diff_up(j,i,k)=diff(j+1,i+1,k);

            end

        end

    end

```

```

                                end
end

for k = 1 : slice-1;

    for i = 1 : xdim-1;

        for j = 1 : ydim-1;

            if ((diff_up(j,i,k)<0)&&(diff_up(j,i,k)~-10));
                diff_up(j,i,k)=0;
            end
            if (diff_up(j,i,k)~-10);
                nrpixels = nrpixels + 1;
            end
        end
    end
end

i5=0;
j5=0;
k5=0;
sum=0;
icount=0;

fid= fopen('mass_check.txt','w');
for k = 1 : ((slice-1)/z_upsfactor);

    k1=k5+1;
    k2=k1+1;
    k3=k2+1;
    k4=k3+1;
    k5=k4+1;
for i = 1 : (xdim-1)/x_upsfactor;

    i1=i5+1;
    i2=i1+1;
    i3=i2+1;
    i4=i3+1;
    i5=i4+1;

    for j = 1: (ydim-1)/y_upsfactor;

        j1=j5+1;
        j2=j1+1;
        j3=j2+1;
        j4=j3+1;
        j5=j4+1;

        for kk=k1:k5;
            for ii=i1:i5;

```

```

        for jj=j1:j5;

            if (diff_up(jj,ii,kk)==-10);
                zeros=zeros+1;
            else
                sum = sum + diff_up(jj,ii,kk);
                icount=icount+1;
            end

        end

    end
end
if (zeros <= (x_upsfactor*y_upsfactor*z_upsfactor*0.4));
    UB{ifile}(j,i,k)=sum /icount;
    scnrpixels=scnrpixels+1;
elseif (zeros >= (x_upsfactor*y_upsfactor*z_upsfactor*0.6));
    UB{ifile}(j,i,k)=0;
else
    UB{ifile}(j,i,k)=-1;
    ave=sum/icount;
    fprintf(fid,'%d %d %d %d %f\n', j, i, k, zeros, ave);
end
zeros=0;
sum=0;
icount=0;
end
j5=0;
end
i5=0;
end

end

%===== UPDATING THE UPSCALED DATA ACCORDING TO MASS BALANCE CHECK =====

S=dlmread('mass_check.txt');
Ssort=sortrows(S,4);
[a,b] = size(Ssort);
npoints=((nrpixels/(x_upsfactor*y_upsfactor*z_upsfactor))-scnrpixels);
rnpoints=round(npoints);
for j=1:rnpoints;
    UB{ifile}(Ssort(j,1),Ssort(j,2),Ssort(j,3))=Ssort(j,5);
end
for j=rnpoints+1:a;
    UB{ifile}(Ssort(j,1),Ssort(j,2),Ssort(j,3))=0;
end

status=fclose(fid);
ave_CT{ifile}=delta_ave_CT;
save upscaled.mat UB ave_CT;
end

```


B.3 Construction of Petro-Physical Data (Porosity and Permeability)

```

clear all
clc

%UPLOADING THE UP-SCALED DATA AND DEFINING THE CONSTANTS AND INITIAL
CONDITIONS

load upscaled.mat;

est_ave_poro = 0.18;
poro_cut_off = 0.31;
swir = 20;
xdim_up=42;
ydim_up=42;
sum_poro = 0;
icount_poro = 0;
sum_perm = 0;
icount_perm = 0;
ave_perm = 0;

%==== CONSTRUCTION OF POROSITY DISTRIBUTION ====

for ifile=1:29;
poro{ifile} = (UB{ifile}/ave_CT{ifile}) * est_ave_poro;

    if (ifile)~=29;
        slice = 10;
    else
        slice = 8;
    end

    for k = 1 : slice;

        for i = 1 : xdim_up;

            for j = 1 : ydim_up;

                if (poro{ifile}(j,i,k)>poro_cut_off);
                    poro{ifile}(j,i,k)=poro_cut_off;
                end

                if (poro{ifile}(j,i,k)~=0);
                    sum_poro = sum_poro + poro{ifile}(j,i,k);
                    icount_poro = icount_poro + 1;
                end

                if ((j>18)&&(j<23)&&(poro{ifile}(j,i,k)==0));
                    poro{ifile}(j,i,k)=-1;
                end
            end
        end
    end
end

```

```

end
end
end

end

%==== CONSTRUCTION OF PERMEABILITY DISTRIBUTION ====

for k = 1 : slice;

    for i = 1 : xdim_up;

        for j = 1 : ydim_up;

            if (poro{ifile}(j,i,k)~= -1);
                perm{ifile}(j,i,k) = (0.136 *
((poro{ifile}(j,i,k)*100)^4.4))/(swir^2);
            else
                perm{ifile}(j,i,k)=-1;
            end

            if
((perm{ifile}(j,i,k)~=0)&&(perm{ifile}(j,i,k)~= -1));
                sum_perm = sum_perm + perm{ifile}(j,i,k);
                icount_perm = icount_perm + 1;
            end
        end
    end
end

end

ave_perm = sum_perm / icount_perm;
ave_poro = sum_poro / icount_poro;

save petrophysics.mat perm poro;

```

B.4 Extraction of Water-Wet CT Data for Calculating Experimental Saturation

```

clear all
clc

%===== UPLOADING WATER-WET CT SCAN DATA =====

for ifile=1:29;

    sprintf('Slice Number: %d',ifile);

    t=num2str(ifile);

    cd CT_water

    if (ifile<10)

        Datafile_water_end=strcat('basar_endimb_00',t);

    elseif (ifile<100)

        Datafile_water_end=strcat('basar_endimb_0',t);

    else

        Datafile_water_end=strcat('basar_endimb_',t);

    end

    A_water_end=dlmread(Datafile_water_end);
    [a,b] = size(A_water_end);

    if (ifile==29);
        slice = 41;
    else
        slice = 50;
    end
    lcount = 1;
    brow = 1;
    xdim = 211;
    ydim = 211;

%=====ARRANGING RAW DATA FROM (23X9+4) TO BE 211 ROWS =====

for row = 1 : a

```

```

for col = 1 : b

    if (lcount == 24)&&(col==4)

        Amap_water_end( brow, (lcount - 1)*9 + col ) = A_water_end(
row, col );
        lcount=0;
        brow=brow+1;
        break

    else

        Amap_water_end( brow, (lcount - 1)*9 + col ) = A_water_end(
row, col );

    end

end

lcount=lcount+1;

end

jk=0;
for k = 1 : slice;

    for i = 1 : xdim;

        for j = 1 : ydim;

            B_water_end(j,i,k)=Amap_water_end(j+(jk*ydim),i);

        end

        jk=jk+1;

    end

end

cd ..;

%== UPLOADING THE SUBTRACTED DATA FOR THE IMPLEMENTATION OF PREVIOUSLY
IDENTIFIED FRACTURE =====

if (ifile<10)

```

```

        Datafile=strcat('subtracted_00',t, '.mat');

elseif (ifile<100)

        Datafile=strcat('subtracted_0',t, '.mat');

else

        Datafile=strcat('subtracted_',t, '.mat');

end

load(Datafile);

for k = 1 : slice;

        for i = 1 : xdim;

                for j = 1 : ydim;

                        if ((j>86)&&(j<113));
                                if (diff(j,i,k)==-10);

                                        B_water_end(j,i,k)=-1728;

                                end
                        end
                end
        end
end

t=num2str(ifile);
if (ifile<10);
filename = ['water_end_00' t '.mat'];
elseif (ifile<100);
filename = ['water_end_0' t '.mat'];
else
filename = ['water_end_' t '.mat'];
end

save (filename);

end

```

B.5 Up-Scaling of the Extracted Data and Saturation Calculation

```

clear all
clc

%==== UPLOADING THE EXTRACTED DATA AND DEFINING UP-SCALING SCHEME ====

for ifile=1:29;

    zeros=0;
    x_upsfactor=5;
    y_upsfactor=5;
    z_upsfactor=5;
    nrpixels=0;
    scnrpixels=0;

    sprintf('Slice Number: %d',ifile);

    t=num2str(ifile);

    if (ifile<10)

        Datafile=strcat('water_end_00',t, '.mat');

    elseif (ifile<100)

        Datafile=strcat('water_end_0',t, '.mat');

    else

        Datafile=strcat('water_end_',t, '.mat');

    end

    load(Datafile);

    if (ifile~=29);

        for k = 1 : slice;

            for i = 1 : xdim-1;

                for j = 1 : ydim-1;

                    B_water_end_up(j,i,k)=B_water_end(j+1,i+1,k);

```

```

                                end
                        end
                end

%===== CALCULATING THE NUMBER OF ROCK PIXELS =====

        for k = 1 : slice;

                for i = 1 : xdim-1;

                        for j = 1 : ydim-1;

                                if
((B_water_end_up(j,i,k)<0)&&(B_water_end_up(j,i,k)~-1728));
                                B_water_end_up(j,i,k)=0;
                                end
                                if (B_water_end_up(j,i,k)~-1728);
                                nrpixels = nrpixels + 1;
                                end
                        end
                end
        end

%===== MASS BALANCE CHECK AND UP-SCALING =====

        i5=0;
        j5=0;
        k5=0;
        sum=0;
        icount=0;

        fid= fopen('mass_check.txt','w');
        for k = 1 : (slice/z_upsfactor);

                k1=k5+1;
                k2=k1+1;
                k3=k2+1;
                k4=k3+1;
                k5=k4+1;
        for i = 1 : (xdim-1)/x_upsfactor;

                i1=i5+1;
                i2=i1+1;
                i3=i2+1;
                i4=i3+1;
                i5=i4+1;

                for j = 1: (ydim-1)/y_upsfactor;

                        j1=j5+1;
                        j2=j1+1;
                        j3=j2+1;

```

```

j4=j3+1;
j5=j4+1;

for kk=k1:k5;
    for ii=i1:i5;
        for jj=j1:j5;

            if (B_water_end_up(jj,ii,kk)==-1728);
                zeros=zeros+1;
            else
                sum = sum + B_water_end_up(jj,ii,kk);
                icount=icount+1;
            end

        end

    end

end

%===== CALCULATING THE NUMBER OF UP-SCALED ROCK PIXELS =====

    if (zeros <= (x_upsfactor*y_upsfactor*z_upsfactor*0.4));
        UB{ifile}(j,i,k)=sum /icount;
        scnrpixels=scnrpixels+1;
    elseif (zeros >= (x_upsfactor*y_upsfactor*z_upsfactor*0.6));
        UB{ifile}(j,i,k)=0;
    else
        UB{ifile}(j,i,k)=-1;
        ave=sum/icount;
        fprintf(fid,'%d %d %d %d %f\n', j, i, k, zeros, ave);
    end
    zeros=0;
    sum=0;
    icount=0;

end
j5=0;
end
i5=0;
end

else

    for k = 1 : slice-1;

        for i = 1 : xdim-1;

            for j = 1 : ydim-1;

                B_water_end_up(j,i,k)=B_water_end(j+1,i+1,k);

```



```

                                end
                            end
                        end

                    for k = 1 : slice-1;

                        for i = 1 : xdim-1;

                            for j = 1 : ydim-1;

                                if
((B_water_end_up(j,i,k)<0)&&(B_water_end_up(j,i,k)~-1728));
                                    B_water_end_up(j,i,k)=0;
                                end
                                if (B_water_end_up(j,i,k)~-1728);
                                    nrpixels = nrpixels + 1;
                                end
                            end
                        end
                    end

                end

            i5=0;
            j5=0;
            k5=0;
            sum=0;
            icount=0;

            fid= fopen('mass_check.txt','w');
            for k = 1 : ((slice-1)/z_upsfactor);

                k1=k5+1;
                k2=k1+1;
                k3=k2+1;
                k4=k3+1;
                k5=k4+1;
            for i = 1 : (xdim-1)/x_upsfactor;

                i1=i5+1;
                i2=i1+1;
                i3=i2+1;
                i4=i3+1;
                i5=i4+1;

                for j = 1: (ydim-1)/y_upsfactor;

                    j1=j5+1;
                    j2=j1+1;
                    j3=j2+1;
                    j4=j3+1;

```

```

        j5=j4+1;

    for kk=k1:k5;
        for ii=i1:i5;
            for jj=j1:j5;

                if (B_water_end_up(jj,ii,kk)==-1728);
                    zeros=zeros+1;
                else
                    sum = sum + B_water_end_up(jj,ii,kk);
                    icount=icount+1;
                end

            end

        end
    end
    if (zeros <= (x_upsfactor*y_upsfactor*z_upsfactor*0.4));
        UB{ifile}(j,i,k)=sum /icount;
        scnrpixels=scnrpixels+1;
    elseif (zeros >= (x_upsfactor*y_upsfactor*z_upsfactor*0.6));
        UB{ifile}(j,i,k)=0;
    else
        UB{ifile}(j,i,k)=-1;
        ave=sum/icount;
        fprintf(fid,'%d %d %d %d %f\n', j, i, k, zeros, ave);
    end
    zeros=0;
    sum=0;
    icount=0;
end
j5=0;
end
i5=0;
end

end

%===== UPDATING THE UPSCALED DATA ACCORDING TO MASS BALANCE CHECK =====

S=dlmread('mass_check.txt');
Ssort=sortrows(S,4);
[a,b] = size(Ssort);
npoints=((nrpixels/(x_upsfactor*y_upsfactor*z_upsfactor))-scnrpixels);
rnpoints=round(npoints);
for j=1:rnpoints;
    UB{ifile}(Ssort(j,1),Ssort(j,2),Ssort(j,3))=Ssort(j,5);
end
for j=rnpoints+1:a;
    UB{ifile}(Ssort(j,1),Ssort(j,2),Ssort(j,3))=0;
end
status=fclose(fid);
save sat_upscaled.mat UB;

end

```

```
load sat_upscaled.mat;

Swav=0.056; %===== Average Water Saturation =====

Ctav=32; %===== Average CT Number =====

slope=(Swav/Ctav);

for ifile=1:29;
Swat{ifile} = (slope*UB{ifile});

end

save saturation.mat Swat;
```

B.6 Optimization

```

clear all
clc
x0 = [-1 -1 -1 -1 -1 -1 -1 -1 -1]; %==== Initial Values for control
Parameters Defining Relative Permeability and Capillary Pressure ====

options = optimset;
options = optimset(options, 'Display', 'iter');
options = optimset(options, 'TolFun', 0.000001); %Tolerance Function
Stopping Criteria
options = optimset(options, 'TolX', 0.0000001 ); %Tolerance Variable
Stopping Criteria
options = optimset(options, 'TolCon', 0);
options = optimset(options, 'FunValCheck', 'on');
options = optimset(options, 'PlotFcns', { @optimplotx
@optimplotfunccount @optimplotfval @optimplotresnorm @optimplotstepsize
@optimplotfirstorderopt });
options = optimset(options, 'Diagnostics', 'on');
options = optimset(options, 'DiffMaxChange', 0.1); %Maximum Perturbation
options = optimset(options, 'DiffMinChange', 0.001 ); %Minimum
Perturbation
options = optimset(options, 'LargeScale', 'on'); %Large-Scale
Optimization Algorithm
options = optimset(options, 'LevenbergMarquardt', 'off');
[x,resnorm,residual,exitflag,output,lambda,jacobian] = ...
lsqnonlin(@obj_calc,x0,[-3],[0],options);

```

B.7 C++ Source Code for Extraction of Required Properties from Simulation Output

```
// read_matrix.cpp : Defines the entry point for the console application.

//

#include <iostream>

#include <fstream>

using namespace std;

int main()
{
    ifstream in1("SW.inc", ios::in);

    ofstream out1("results/output.out", ios::out);

    ofstream out2("results/time.out", ios::out);

    int ttt,iii,jjj,j,k;

    double *time;

    int index_i = 42;

    int index_j = 42;

    int index_k = 288;

    int index_t = 26;

    //double sat[5][42][42][40];

    double ****sat;

    sat= (double ****) malloc (sizeof(double****) * index_t);

    for(ttt=0; ttt<index_t; ttt++)
```

```

*(sat+ttt) = (double ***) malloc (sizeof(double**) * index_i);

for(ttt=0; ttt<index_t; ttt++)

    for( iii=0; iii<index_i; iii++)

        (*(sat+ttt) + iii) = (double**) malloc (sizeof(double*) * index_j);

for(ttt=0; ttt<index_t; ttt++)

    for( iii=0; iii<index_i; iii++)

        for(jjj=0; jjj<index_j; jjj++)

            *( *( *(sat+ttt) + iii) + jjj) = (double*) malloc

(sizeof(double) * index_k);

```

```

time= (double *) malloc (sizeof(double) * index_t);

char dum[100];

```

```

time[0]=0;

for (int ii=0; ii<index_i; ii++){

    for (int jj=0; jj<index_j; jj++){

        for (int kk=0; kk<index_k; kk++){

            sat[0][ii][jj][kk]=0;

        }

    }

}

```

```

for (ii=1; ii<= 6; ii++)

```

```

        in1.getline(dum,100);
    for (int tt=1; tt<index_t; tt++){
        in1.getline(dum,100);
        for (ii=1; ii<=7; ii++)
            in1 >> dum[ii];
        in1 >> time[tt];
        in1.getline(dum,100);
        for (ii=1; ii<= 4; ii++)
            in1.getline(dum,100);
        for (int jj=0; jj<index_j*index_k; jj++){
            for (ii=1; ii<=4; ii++)
                in1 >> dum[ii];
            in1 >> k;
            for (ii=1; ii<=3; ii++)
                in1 >> dum[ii];
            in1 >> j;
            for (ii=0; ii<index_i; ii++)
                in1 >> sat[tt][ii][j-1][k-1];
        }
    }

    for (tt=0; tt<index_t; tt++){
        out2.width(15);
        out2 << time[tt] << endl;
    }

```

```

        for (int kk=0; kk<index_k; kk++){
            for (int jj=0; jj<index_j; jj++){
                for (ii=0; ii<index_i-1; ii++){
                    out1.width(15);
                    out1 << sat[tt][ii][jj][kk];
                }
                out1.width(15);
                out1 << sat[tt][41][jj][kk] << endl;
            }
        }
    }
    return 0;

    for(ttt=0; ttt<index_t; ttt++)
        free(*(sat+ttt));

    for(ttt=0; ttt<index_t; ttt++)
        for( iii=0; iii<index_i; iii++)
            free(*( *(sat+ttt) + iii));

    for(ttt=0; ttt<index_t; ttt++)
        for( iii=0; iii<index_i; iii++)
            for(jjj=0; jjj<index_j; jjj++)
                free(*( *( *(sat+ttt) + iii) + jjj));

    free (sat);
}

```


VITA

BASAR BASBUG

Basar Basbug was born in Ankara, Turkey on December 25, 1979. He graduated from Ayranci Super High School in 1997. He received a B.Sc. degree in Petroleum and Natural Gas Engineering from Middle East Technical University, Ankara, Turkey in 2002. He pursued his graduate study in the same university and earned a M.Sc. degree in Petroleum and Natural Gas Engineering in 2005. During this period, he was appointed as a teaching and a research assistant. His research interest focused on reservoir simulation, fluid flow through porous media and CO₂ sequestration. After graduation, he came to the United States to pursue doctoral studies and joined Penn State in August, 2005. Since then, he has been a Ph.D. candidate in the Petroleum and Natural Gas Engineering Program. During his doctoral study, he was awarded with graduate research assistantship and received “Anne C. Wilson Graduate Student Research Award” by the College of Earth and Mineral Sciences in 2005. He specialized in modeling of spontaneous imbibition and developing history matching approach in naturally fractured reservoirs. His research works have been published in technical journals, and in the conference proceedings. He is a member of Society of Petroleum Engineers.